Development of synaptic light-emitting transistors : towards multifunctional organic electronic devices

Yusheng Chen

UNIVERSITÉ DE STRASBOURG

ÉCOLE DOCTORALE des Sciences Chimiques

[UMR 7006]

THÈSE

présentée par :

[Yusheng CHEN]

soutenue le : **23 Juin 2023**

pour obtenir le grade de : **Docteur de l'université de Strasbourg**

Discipline/ Spécialité : Chimie

Développement de transistors électroluminescents synaptiques : vers des dispositifs électroniques organiques multifonctionnels

THÈSE dirigée par :

M. SAMORI Paolo — Professeur, Institut de Science et d'Ingénierie Supramoléculaires, Université de Strasbourg & CNRS, Strasbourg, France

RAPPORTEURS :

Mme. INAL Sahika — Professeur, Biological and Environmental Science and Engineering, King Abdullah University of Science and Technology (KAUST), Thuwal, Saudi Arabia

M. FABIANO Simone — Professeur, Department of Science and Technology, Linköping University, Norrköping, Sweden

AUTRES MEMBRES DU JURY :

M. HEISER Thomas — Professeur, ICube, Université de Strasbourg & CNRS, Strasbourg, France

Résumé

Les technologies de l'information émergentes, notamment l'intelligence artificielle, les mégadonnées et l'Internet des objets, entraînent un changement de paradigme dans notre société, améliorant profondément la qualité de vie sur notre planète. Ces technologies reposent sur des dispositifs électroniques multifonctionnels capables de collecter, traiter, stocker et échanger des données. Par rapport aux matériaux électroniques traditionnels à base de silicium, les molécules organiques offrent de nombreux avantages, tels que des propriétés physiques et chimiques ajustables, un poids ultraléger, une flexibilité mécanique, une facilité de traitement avec des méthodes évolutives et une rentabilité.[1, 2] À l'avenir, les dispositifs électroniques à base de molécules organiques conviendront particulièrement aux applications en tant que systèmes de surveillance humaine, y compris la détection chimique et physique, le stockage de données et les dispositifs émettant de la lumière.[3–5]

Une stratégie bien établie pour améliorer les performances des dispositifs électroniques et réduire la consommation d'énergie repose sur la réduction de la taille des composants électroniques, c'est-à-dire des transistors dans les microprocesseurs. Cependant, les effets quantiques et les phénomènes d'effet tunnel d'électrons entrent en jeu, empêchant la miniaturisation des composants du dispositif en dessous de 5 nm. Une autre façon de stimuler la fonctionnalité des dispositifs électroniques, comme stratégie alternative à la miniaturisation, repose sur la diversification fonctionnelle à travers le développement de dispositifs capables d'effectuer des tâches multiples. La multifonctionnalité dans les matériaux et les dispositifs optoélectroniques peut être obtenue en exploitant des films multicomposants qui peuvent être développés par mélange ou par dépôt couche par couche, comme réalisé par des protocoles d'évaporation thermique et d'enduction en solution, chaque couche conférant une fonction donnée au dispositif.[6]

Alors que le développement de dispositifs multifonctionnels fait l'objet d'une

grande attention depuis plus d'une décennie, l'incorporation simultanée du stockage de données et de la fonction d'émission de lumière est sous-explorée. Ici, l'objectif de cette thèse est d'intégrer la fonction de mémoire et la fonction d'émission de lumière dans un dispositif donné. En particulier, le courant post-synaptique est exploité pour alimenter des matériaux émettant de la lumière, produisant une émission de lumière post-synaptique.

Cette thèse est subdivisée en 8 chapitres. Le chapitre 1 présente le but et la structure de la thèse. Les chapitres 2 et 3 offrent une introduction aux mémoires et aux dispositifs émettant de la lumière, respectivement.

Les molécules à longue rémanence ont suscité beaucoup d'intérêt en raison de leur application potentielle dans le stockage optique de données, les capteurs, l'imagerie in vivo et la lutte contre la contrefaçon. En effet, la luminescence de longue durée dans les dispositifs optoélectroniques est très recherchée dans les technologies de stockage optique de données et d'affichage. Le chapitre 4 présente la fabrication de transistors électroluminescents organiques à longue rémanence (LAOLET), dont le fonctionnement repose sur une nouvelle stratégie basée sur un effet synaptique photo-induit dans une couche de canal semi-conductrice inorganique, pour alimenter l'électroluminescence lorsqu'elle est interfacée avec un matériau organique émettant de la lumière, comme en Figure I. Des films minces semi-conducteurs amorphes d'oxyde de zinc-gallium-indium (IGZO) ont été utilisés non seulement comme couche de canal de type N, mais également comme couche de fonction mémoire en raison de leur grande mobilité et de leur caractéristique de photoconductivité persistante. En raison de la cinétique lente de recombinaison des électrons photogénérés avec les lacunes d'oxygène dans la couche de canal, le matériau organique peut être alimenté par un courant post-synaptique et présenter une émission de lumière de longue durée (des centaines de secondes) après l'arrêt de l'irradiation UV. En faisant varier la polarisation de la grille, nos LAOLET présentent une émission de lumière persistante avec une durée de vie variable après exposition à un stimulus UV. En l'absence de

tension de grille appliquée, une telle émission de lumière d'après-glow facilitée par la plasticité synaptique de 11 cd m^{-2} présente une durée de vie supérieure à 270 s, après 50 s d'irradiation UV. Au lieu de cela, lorsqu'une tension de grille de −30 V est appliquée, une luminosité plus faible de 4 cd m^{-2} et une durée de vie plus courte de 159 s ont été observées après une irradiation UV de 50 s.

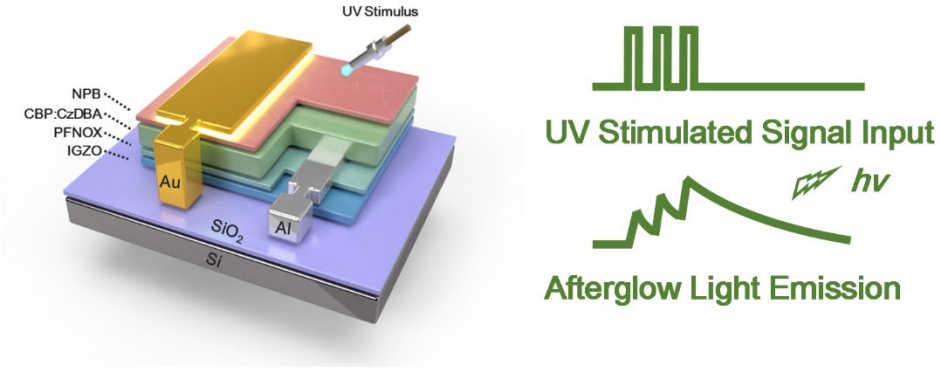

Figure I. Image schématique illustrant la structure du dispositif et le mécanisme de fonctionnement des LAOLET à impulsion UV. La couche de transport d'électrons est constituée de poly[9,9-bis(60-(N,N-diéthylamino) hexyl)-fluorène-alt-9,9-bis(3-éthyl(oxétane-3-éthoxy)-hexyl)-fluorène] (PFNOX), tandis que la couche de transport de trous est composée de N,N′-Di(1-naphtyl)-N,N′-diphényl-(1,1′-biphényl)-4,4′-diamine (NPB). La couche d'émission de lumière comprend du 9,10-bis(4-(9H-carbazol-9-yl)-2,6-diméthylphényle)-9,10-diboraanthracène (CzDBA) en tant que matériau émetteur de lumière verte hébergé dans une matrice de 4,4-bis(N-carbazolyl)-1,1-biphényle (CBP).

L’utilisation du courant post-synaptique pour générer une luminescence de longue durée présente un potentiel de rupture pour l’exploitation de la prochaine génération d’écrans intelligents. Pour obtenir une longue émission de rémanence multisensible, des LAOLET à impulsion électrique peuvent être conçus pour des signaux d’entrée présynaptiques distinctes. Le chapitre 5 présente des LAOLET à impulsion électrique, dont le fonctionnement repose sur une architecture à grille flottante nanométrique,

comme le montre la Figure II. Une couche de nanoparticules Au (NPs Au) d'une taille de 5 nm a été déposée entre la couche diélectrique (SiO_2) et la couche tunnel (Al_2O_3) pour le stockage de charge, fournissant un comportement de mémoire des dispositifs. Des affichages reconfigurables peuvent être réalisés en sélectionnant la polarité de la tension de grille. Une longue émission de rémanence avec une luminosité et un temps de rétention reconfigurables est observée lors de l'application d'une impulsion de tension de grille positive spécifique. Une fois qu'une pointe de tension de grille positive de stimulus de 100 V est terminée, le courant post-synaptique et la luminosité ont augmenté à 0.12 mA et 81 cd m^{-2}. Après avoir répété huit fois des pointes positives, le courant post-synaptique et la luminosité ont augmenté pour atteindre 0.24 mA et 142 cd m^{-2}. Inversement, lorsqu'un stimulus de tension de grille négative est appliqué, ces LAOLET fonctionnent comme un affichage cliquable. Un courant à l'état passant stable d'environ 1 mA accompagné d'une luminosité stable d'environ 300 cd m^{-2} est observé sous une tension de grille négative.

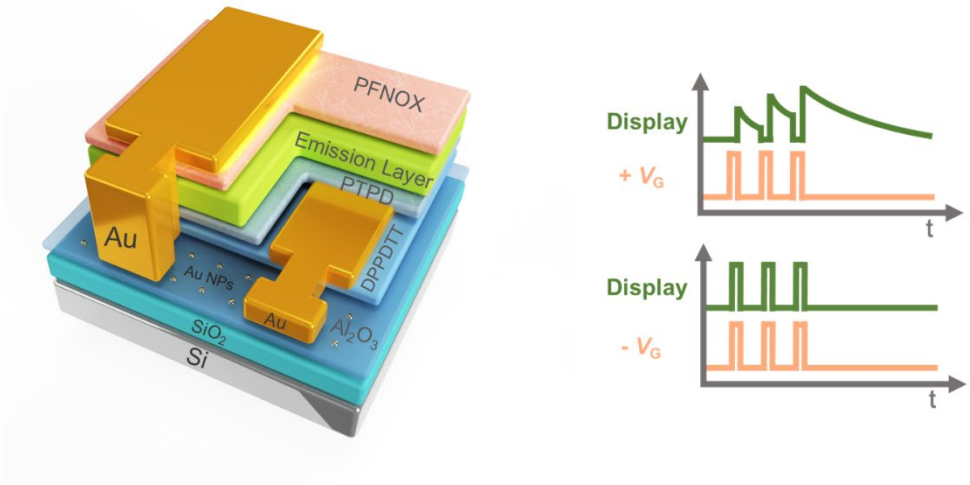

Figure II. Image schématique illustrant la structure du dispositif et le mécanisme de fonctionnement des LAOLET à impulsion électrique. Le poly((2,3,5,6-tétrahydro-2,5-bis(2-octyldodécyl)-3,6-dioxopyrrolo(3,4-c)pyrrole-1,4-diyl)-2,5-thiophènediylthiéno(3,2-b)thiophène-2,5-diyl-2,5 thiophènediyl) (DPPDTT) a été utilisé comme couche de canal. Le poly(4-butylphényl-diphényl-amine) (PTPD) et le

PFNOX ont été incorporés en tant que couche de transport d'électrons et de trous, respectivement. Divers matériaux d'émission de lumière ont été utilisés pour des LAOLETs en couleur complète.

Les dispositifs organiques émettant de la lumière sont des composants clés pour les applications optoélectroniques émergentes, notamment les écrans intelligents et la surveillance de la santé. Malgré les grandes avancées réalisées grâce à l'intégration de la fonction de mémoire dans les dispositifs OLETs, les LAOLETs fabriqués sur une tranche de silicium avec SiO_2 comme couche diélectrique à faible constante diélectrique (k_{SiO_2} = 3.9) nécessitent une tension de travail élevée, c'est-à-dire d'environ 100 V, ce qui devrait être réduit à un niveau de consommation d'énergie faible et même à un niveau de sécurité lorsqu'ils sont en contact avec les tissus humains. Dans le chapitre 6, des matériaux à constante diélectrique élevée (k), de l'oxyde de lanthane-aluminium ($LaAlO_x$, k_{LaAlO_x} = 13), ont servi de couche diélectrique dans les LAOLET (Figure III). Utilisant des matériaux à haute mobilité comme couche de canal, les LAOLET basse tension de type P et de type N sont fabriqués avec succès sur le substrat de verre grâce à toutes les technologies de traitement de solution, permettant ainsi une diminution significative de la tension de fonctionnement à 12 V. De plus, dans les LAOLETs à faible tension de type N, le courant post-synaptique et la luminosité facilités par la tension d'amplification reposaient sur la couche électrolytique d'AlO_x, qui est déposée entre la couche $LaAlO_x$ et la couche de canal. À l'inverse, une émission de longue durée après stimulation de la tension de déplétion s'est produite dans les LAOLETs à faible tension de type P, ce qui peut être attribué à la grille flottante de nanoparticules d'or incorporée dans la couche $LaAlO_x$. Des études approfondies sur les affichages à longue durée d'afterglow, qui imitent un comportement synaptique distinct, ont été menées pour prouver la polyvalence des LAOLETs à faible tension.

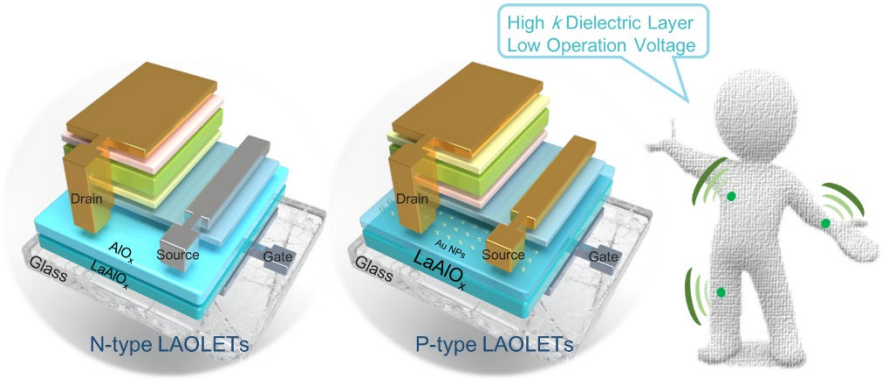

Figure III. Image schématique illustrant la structure du dispositif des LAOLET à basse tension, qui présentent un potentiel d'application dans le domaine de la surveillance de la santé. La couche de canal, la couche d'émission de lumière et la couche de transport de charge ont ensuite été déposées sur le dessus des matériaux à haute *k*.

Le chapitre 7 présente l'application de OLET à longue rémanence. Comme preuve de concept, des réseaux de LAOLET à stimulus UV ont été utilisés en tant que capteurs UV visuels qui émettent une lumière verte de longue durée dans les régions irradiées. De manière significative, en conférant aux LAOLET à impulsion électrique des capacités de détection de force, ils peuvent fonctionner comme des capteurs de pression à longue rémanence qui émettent une lumière verte de longue durée à la suite d'une action d'extrusion contrôlée.

Le chapitre 8 résume le travail de thèse et fournit des lignes directrices pour l'intégration réussie de multifonctionnalité dans un seul dispositif. L'émission de lumière dans les OLET peut être alimentée par un courant post-synaptique, produisant une émission de lumière post-synaptique avec deux propriétés synaptiques spéciales,[7] la plasticité à impulsion dépendante du temps et la transmission de la mémoire à court terme à la mémoire à long terme. Les connaissances développées dans le cadre de cette thèse ont un potentiel pour de futurs travaux de recherche et de développement révolutionnaires. À court terme, des avancées importantes peuvent être prévues en

améliorant les performances des LAOLET grâce à la conception optimale des matériaux émettant de la lumière afin de garantir un rendement quantique élevé ou en intégrant la couche d'injection/de blocage d'électrons/de trous dans l'architecture du dispositif.[8] Dans le contexte de l'incorporation de capteurs chimiques et physiques sur des substrats extensibles, les dispositifs LAOLET peuvent être utilisés à intégrer dans des humains ou des robots.[9] À long terme, la vision de la fabrication d'un cerveau artificiel a poussé les chercheurs à imiter la fonction du réseau neuronal naturel du cerveau par un réseau tridimensionnel de mémoires à l'état solide.[10] À l'avenir, des mémoires optiques comprenant des LAOLET et des dispositifs optiques commutables peuvent être envisagés pour faire le lien entre les fonctions intrinsèques des mémoires instantanées et permanentes, reproduisant ainsi la relation entre les synapses et les protéines/tissus dans le cerveau humain.

Références :

1. Hu, P.; He, X.; Jiang, H. Greater than 10 $cm^2 V^{-1} s^{-1}$: A Breakthrough of Organic Semiconductors for Field-effect Transistors. InfoMat 2021, 3, 613–630.

2. Lee, Y.; Park, J.; Choe, A.; Cho, S.; Kim, J.; Ko, H. Mimicking Human and Biological Skins for Multifunctional Skin Electronics. Adv. Funct. Mater. 2019, 30, 1904523.

3. Borges-González, J.; Kousseff, C. J.; Nielsen, C. B. Organic Semiconductors for Biological Sensing. J. Mater. Chem. C 2019, 7, 1111–1130.

4. Zhu, Z.; Guo, Y.; Liu, Y. Application of Organic Field-effect Transistors in Memory. Mater. Chem. Front. 2020, 4, 2845–2862.

5. Ganesan, P.; Tsao, H. N.; Gao, P. En Route to Wide Area Emitting Organic Light-Emitting Transistors for Intrinsic Drive-Integrated Display Applications: A Comprehensive Review. Adv. Funct. Mater. 2021, 31, 2105506.

6. Lee, G. H.; Moon, H.; Kim, H.; Lee, G. H.; Kwon, W.; Yoo, S.; Myung, D.; Yun, S. H.; Bao, Z.; Hahn, S. K. Multifunctional Materials for Implantable and Wearable Photonic Healthcare Devices. Nat. Rev. Mater. 2020, 5, 149–165.

7. van de Burgt, Y.; Melianas, A.; Keene, S. T.; Malliaras, G.; Salleo, A. Organic Electronics for Neuromorphic Computing. Nat. Electron. 2018, 1, 386–397.

8. Byeon, S.; Lee, D.; Yook, K.; Lee, J. Recent Progress of Singlet-Exciton-Harvesting Fluorescent Organic Light-Emitting Diodes by Energy Transfer Processes. Adv.Mater. 2019, 31, 1803714.

9. Lee, Y.; Park, J.; Choe, A.; Cho, S.; Kim, J.; Ko, H. Mimicking Human and Biological Skins for Multifunctional Skin Electronics. Adv. Funct. Mater. 2020, 30, 1904523.

10. Ham, D.; Park, H.; Hwang, S.; Kim, K. Neuromorphic Electronics based on Copying and Pasting the Brain. Nat. Electron. 2021, 4, 635–644.

Abstract

Emerging information technologies including artificial intelligence, big data, and Internet of Things are imposing a paradigm shift in our society, profoundly improving the quality of life on our planet. These technologies rely on multifunctional electronic devices which are able to collect, process, store and exchange data. Compared with traditional silicon-based electronic materials, organic molecules offer numerous advantages, such as tunable physical and chemical properties, ultralight weight, mechanical flexibility, easy processability with scalable methods and cost-efficiency.[1, 2] In the future, electronic devices based on organic molecules are particularly well-suited for applications as human monitoring systems including chemical and physical sensing, data storage and light-emitting devices.[3-5]

One well-established strategy to improve performance of electronic devices and reduce the power consumption relies on shrinking the size of electronic components, *i.e.* transistors in microprocessors. However, quantum effects and electron tunneling phenomena come into play preventing a miniaturization of device components below 5 nm. Another way to boost the functionality of electronic devices, as alternative strategy to miniaturization, relies on the functional diversification through the development of devices capable to perform multiple tasks. Multifunctionality in materials and opto-electronic devices can be achieved by exploiting multicomponent films that can be developed by blending or by controlled layer-by-layer deposition, as realized by thermal evaporation and solution-coating protocols, with each layer imparting a give function to the device.[6]

While the development of multifunctional devices has been under the spotlight for over a decade, the simultaneous incorporation of data storage and light-emitting function is underexplored. Herein, the goal of this thesis is to integrate memory function and light emission function into a given devices. In particular, post-synaptic current is exploited to drive light emission materials, yielding a post-synaptic light emission.

This thesis is subdivided into 8 chapters. In chapter 1, the purpose and the structure of this thesis are presented. Chapter 2 and 3 offer an introduction to memories and light-emitting devices, respectively.

Long afterglow molecules have raised quite some interests in view of their potential application in optical data storage, sensors, in-vivo imaging and anti-counterfeiting. In fact, long-lasting luminescence in opto-electronic devices is highly sought after in optical data storage and display technology. In chapter 4, the fabrication of long afterglow organic light-emitting transistors (LAOLETs) is presented, whose operation relies on a novel strategy based on a photo-induced synaptic effect in an inorganic semiconductor channel layer, to power electroluminescence when interfaced with an organic light-emitting material, as presented in Figure I. Amorphous semiconducting Indium gallium zinc oxide (IGZO) based thin films have been employed not only as N-type channel layer but also memory function layer due to their high mobility and persistent photoconductivity characteristic. Due to the slow recombination kinetics of photo-generated electrons to oxygen vacancies in the channel layer, the organic material can be fueled by post-synaptic current and displayed a long-lived light-emission (hundreds of seconds) after ceasing UV irradiation. By varying the gate bias, our LAOLETs exhibit persistent light-emission featuring variable lifetime after exposure to UV stimulus. In absence of an applied gate voltage, such a synaptic-plasticity facilitated afterglow emission of 11 cd m^{-2} has a lifetime exceeding 270 s, after 50 s UV irradiation. Instead, when a gate voltage of −30 V applied, weaker brightness of 4 cd m^{-2} and shorter lifetime of 159 s were observed after 50 s UV irradiation.

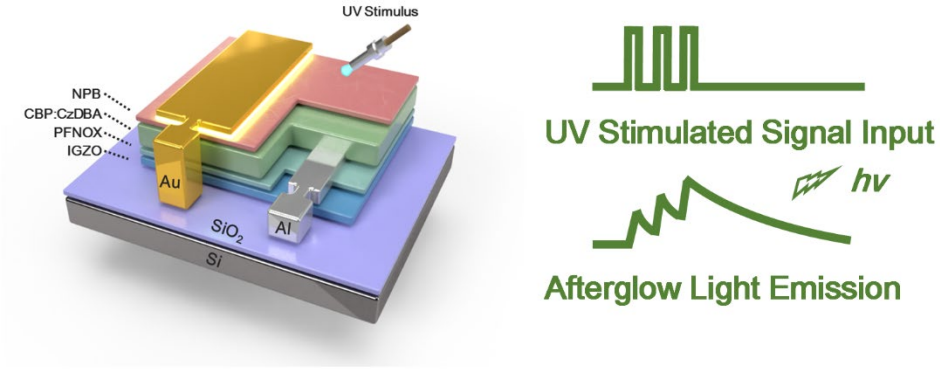

Figure I. Schematic image for illustration the device structure and work mechanism of UV-spike LAOLETs. Poly[9,9-bis(60-(N,N-diethylamino) hexyl)-fluorene-alt-9,9-bis(3-ethyl(oxetane-3-ethyoxy)-hexyl)-fluorene] (PFNOX) and N,N′-Di(1-naphthyl)-N,N′-diphenyl-(1,1′-biphenyl)-4,4′-diamine (NPB) were embedded as electron and hole transport layer, respectively. The light-emission layer comprises 9,10-bis(4-(9H-carbazol-9-yl)-2,6-dimethylphenyl)-9,10-diboraanthracene (CzDBA) as a green light-emitting material hosted in a 4,4-bis(N-carbazolyl)-1,1-biphenyl (CBP) matrix.

The use of postsynaptic current to drive long-lasting luminescence holds a disruptive potential for harnessing the next-generation of smart displays. To achieve multiresponsive long afterglow emission, electrical spiked LAOLETs can be designed for distinct presynaptic signals inputs. In chapter 5, electrical spiked LAOLETs are presented, whose operation relies on a nano-floating gate architecture, as shown in Figure II. A layer of Au nanoparticles (Au NPs) with size of 5 nm was deposited in-between the dielectric layer (SiO_2) and the tunneling layer (Al_2O_3) for charge storage, providing a memory behavior to the devices. Reconfigurable displays can be realized by the selecting polarity of gate voltage. Long afterglow emission is observed upon applying specific positive gate voltage spiked. Once a positive gate voltage spike of 100 V stimulus finished, the post-synaptic current and brightness increased to 0.12 mA and 81 cd m^{-2}. After repeating positive spikes eight times, the post-synaptic current and brightness have grown reaching 0.24 mA and 142 cd m^{-2}. Conversely, when negative

gate voltage stimulus is applied, these LAOLET function as click-on display. A stable on-state current of ~ 1 mA accompanied with stable brightness of ~ 300 cd m^{-2} is observed under every negative gate voltage spike.

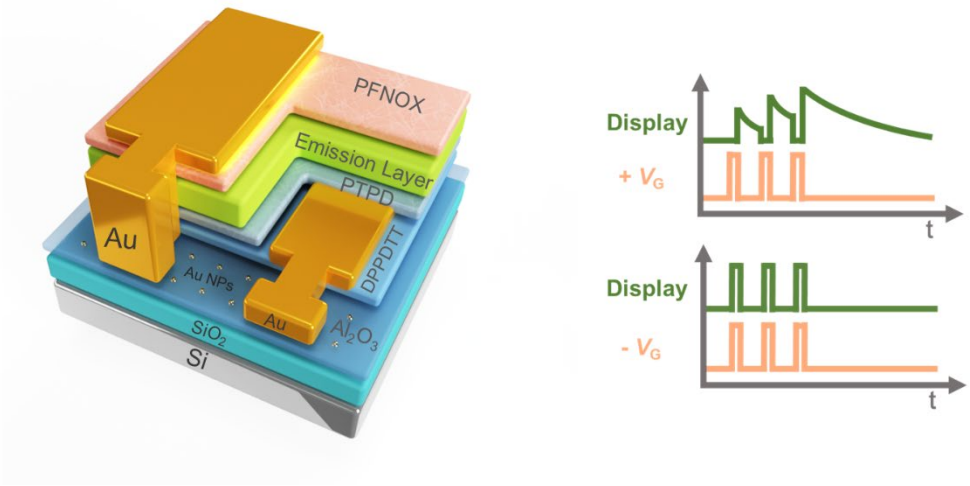

Figure II. Schematic image for illustration the device structure and work mechanism of electrical-spike LAOLETs. Poly((2,3,5,6-tetrahydro-2,5-bis(2-octyldodecyl)-3,6-dioxopyrrolo(3,4-c)pyrrole-1,4-diyl)-2,5-thiophenediylthieno(3,2-b)thiophene-2,5-diyl-2,5 thiophenediyl) (DPPDTT) was utilized as channel layer. Poly(4-butylphenyl-diphenyl-amine) (PTPD) and PFNOX were embedded as electron and hole transport layer, respectively. Various light emission materials were employed for full color LAOLETs.

Organic light-emitting devices are key components for emerging opto-electronics applications including smart displays and health monitoring. Despite the great advancements realized by integration the memory function into OLETs devices, LAOLETs fabricated on silicon wafer with SiO_2 as low dielectric constant (k) dielectric layer (k_{SiO_2} = 3.9) need high operation work voltage, *i.e.* around 100 V, which should be promoted to a low energy consumption level and even a safety level when interfaced with human tissues. In chapter 6, high k materials, lanthanum-aluminum oxide ($LaAlO_x$, k_{LaAlO_x} = 13), served as dielectric layer in LAOLETs (Figure III). Utilizing high mobility

materials as channel layer, both P-type and N-type low voltage LAOLETs are successfully fabricated on the glass substrate through all solution processing technology, respectively, thereby endowing significantly decreasing of the operation voltage to 12 V. Moreover, in N-type low voltage LAOLETs, post-synaptic current and brightness facilitated by amplification voltage relied on the electrolyte layer of AlO_x, which is deposited in-between $LaAlO_x$ layer and channel layer. Conversely, long afterglow emission after depletion voltage stimulus occurred in P-type low voltage LAOLETs, which can be attributed to the floating-gate of Au NPs embedded inside the $LaAlO_x$ layer. In-depth studies on long afterglow displays mimicking distinct synaptic behavior were carried out to prove the versatility of low voltage LAOLETs.

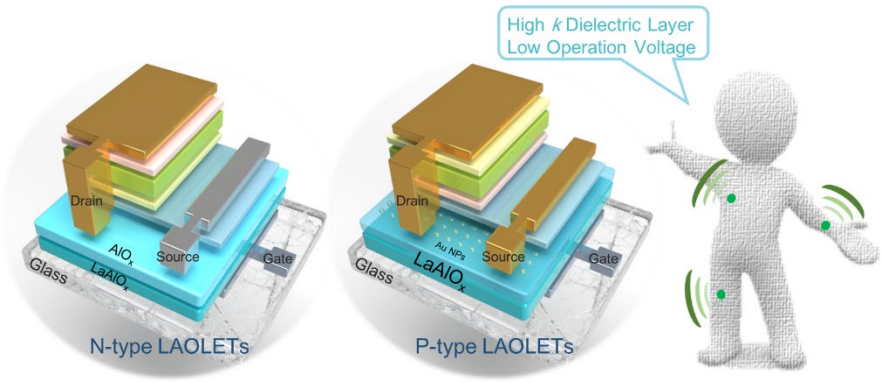

Figure III. Schematic image for illustration the device structure of low voltage LAOLETs, which present potential for the application in health monitoring. Channel layer, light emission layer, charge transport layer and were subsequently deposited on top of the high *k* materials.

In chapter 7, applications of LAOLETs are presented. As a proof-of-concept, UV-spiked LAOLETs arrays were operated as visual UV sensors which emit long-lasting green light in the irradiated regions. Significantly, upon endowing electrical spiked LAOLETs with force sensing capabilities, they can operate as long afterglow pressure sensors which emits long-lasting green light subsequently to a controlled extrusion

action.

Chapter 8 summarizes the thesis work and provides guidelines for the successful integration of multifunctionality into one single devices. Light emission in OLETs can be powered by post-synaptic current, yielding post-synaptic light emission with two special synaptic property,[7] spiked-time-dependent-plasticity and short-term memory to long-term memory transition. The knowledge developed in the framework of this thesis holds potential for future groundbreaking research and development. On the short-term, key steps forward can be foreseen by improving the performance of LAOLETs through the optimal design of the light emissive materials to guarantee high quantum yield or by embedding the electron/hole injection/blocking layer into the device architecture.[8] In the context of incorporating chemical and physical sensors on stretchable substrates, the LAOLET devices can be utilized for the realization of multifunctional e-skin in human or robot.[9] On the long-term, the vision of artificial brain fabrication has inspired researchers to mimic the function of natural brain neuronal network by three-dimensional network of solid-state memories.[10] In the future, optical memories comprising LAOLETs and optical switchable devices can be foreseen to bridge the functions intrinsic to instantaneous and to permanent memories, thereby reproducing the relationship of synapse and protein/tissue in the human brain.

Reference:

1. Hu, P.; He, X.; Jiang, H. Greater than 10 $cm^2 V^{-1} s^{-1}$: A Breakthrough of Organic Semiconductors for Field-effect Transistors. *InfoMat* **2021,** 3, 613−630.

2. Lee, Y.; Park, J.; Choe, A.; Cho, S.; Kim, J.; Ko, H. Mimicking Human and Biological Skins for Multifunctional Skin Electronics. *Adv. Funct. Mater.* **2019,** 30, 1904523.

3. Borges-González, J.; Kousseff, C. J.; Nielsen, C. B. Organic Semiconductors for

Biological Sensing. *J. Mater. Chem. C* **2019,** 7, 1111−1130.

4. Zhu, Z.; Guo, Y.; Liu, Y. Application of Organic Field-effect Transistors in Memory. *Mater. Chem. Front.* **2020,** 4, 2845−2862.

5. Ganesan, P.; Tsao, H. N.; Gao, P. En Route to Wide Area Emitting Organic Light-Emitting Transistors for Intrinsic Drive-Integrated Display Applications: A Comprehensive Review. *Adv. Funct. Mater.* **2021,** 31, 2105506.

6. Lee, G. H.; Moon, H.; Kim, H.; Lee, G. H.; Kwon, W.; Yoo, S.; Myung, D.; Yun, S. H.; Bao, Z.; Hahn, S. K. Multifunctional Materials for Implantable and Wearable Photonic Healthcare Devices. *Nat. Rev. Mater.* **2020,** 5, 149−165.

7. van de Burgt, Y.; Melianas, A.; Keene, S. T.; Malliaras, G.; Salleo, A. Organic Electronics for Neuromorphic Computing. *Nat. Electron.* **2018,** 1, 386−397.

8. Byeon, S.; Lee, D.; Yook, K.; Lee, J. Recent Progress of Singlet-Exciton-Harvesting Fluorescent Organic Light-Emitting Diodes by Energy Transfer Processes. *Adv.Mater.* **2019**, 31, 1803714

9. Lee, Y.; Park, J.; Choe, A.; Cho, S.; Kim, J.; Ko, H. Mimicking Human and Biological Skins for Multifunctional Skin Electronics. *Adv. Funct. Mater.* **2020**, 30, 1904523.

10. Ham, D.; Park, H.; Hwang, S.; Kim, K. Neuromorphic Electronics based on Copying and Pasting the Brain. *Nat. Electron.* **2021**, 4, 635−644.

Symbols and Abbreviations

AFM	Atomic Force Microscopy
Au NPs	Gold Nano-Particles
FET	Field-Effect Transistor
HOMO	Highest Occupied Molecular Orbital
I_{on}/I_{off}	On/Off Current Ratio
$I_{P/E}$	Program/Erase Current Ratio
I_{DS}	Drain-Source Current
I_{GS}	Gate-Source Current
LAOLET	Long Afterglow Organic Light-Emitting Transistor
LTM	Long-Term Memory
LUMO	Lowest Unoccupied Molecular Orbital
OFET	Organic Field-Effect Transistor
OLED	Organic Light-Emitting Diode
OLET	Organic Light-Emitting Transistor
OMT	Organic Memory Transistor
OSC	Organic Semiconductor

OSFET	Optically Switchable Field-Effect Transistor
PPC	Persistent Photoconductivity
PSB	Post-Synaptic Brightness
PSC	Post-Synaptic Current
STDP	Spike-Timing-Dependence-Plasticity
SEM	Scanning Electron Microscopy
STM	Short-Term Memory
TADF	Thermally Activated Delayed Fluorescence
TEM	Transmission Electron Microscope
V_{Th}	Threshold Voltage
ΔV_{Th}	Memory Window, Shifted Threshold Voltage
UV	Ultraviolet Light
V_G	Gate-Source Voltage
V_D	Drain-Source Voltage
Vis	Visible Light
k	Dielectric Constant
μ	Field-Effect Mobility

Table of contents

Chapter 1. Introduction

1.1. Brief Introduction of FETs

Thin-film field-effect transistors (FETs) are the basic element for the development of nowadays electronics and tomorrow's logic circuits. They possess unique functions of signal amplification and controlled switching, which qualifies them as key components in integrated electronic circuitries. Organic semiconductor (OSC) can operate as active materials once incorporated in organic field-effect transistors (OFETs) and because of this reason they have been successfully employed for both fundamental studies and for a variety of technological applications in electronics,[1] and biology,[2] *i.e.* in today's electronic circuitries composing computers and smart phones, in biosensing including Covid-19 detection.[3-4] In contrast to traditional silicon technology which relies on expensive manufacturing processes and on the use of rigid and brittle materials, organic semiconductors are promising candidates for the next-generation of smart, portable and wearable devices. The tremendous work carried out during the last three decades on the development of novel OSC, their controlled processing and device optimization made it possible to increase field-effect mobilities in organic transistors, reaching values up to 20 $cm^2 V^{-1} s^{-1}$.[5-7] Such versatility of OSC materials allowed them to be processed as mechanically flexible, foldable and stretchable films over large areas, and thus be integrated in low-cost and high-performance organic memory transistors (OMTs)[8] and organic light-emitting transistors (OLETs)[9] via printing and other solution-based casting methods.

The structure of OFETs can be classified into four types differing on the distinct order of functionalized layers deposition, *i.e.* geometry, which are presented in Figure 1-1: (a) bottom-gate top-contact, (b) bottom-gate bottom-contact, (c) top-gate bottom-contact, and (d) top-gate top-contact. Silicon wafer with thermally grown oxide layer is commercially available substrate, acting as gate electrode and dielectric layer for fabrication of bottom-gate OFETs. Contact electrode and channel layer based on OSC

can be deposited on the silicon wafer leading a simpler experiment, compared with top-gate devices fabrication requiring further deposition of dielectric layer. However, in bottom-gate architecture, the OSC is exposed to the environment, which can contain oxygen and water, resulting in accelerated degradation and requiring one more encapsulation layer for protection. In contrast, in top-gate architecture, dielectric layer deposited on the top of OSC can isolate the semiconductor from the environment and thus leading the enhancement of device lifetime.

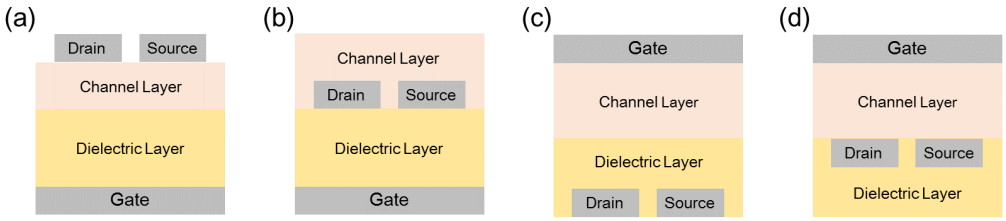

Figure 1-1. Schematic image of four different architecture of OFETs.

The key parameters of OFETs include:

i) Field-effect mobility (μ): The mobility of materials is an important parameter which defines how fast the charge carriers (electrons or holes) move through the OSC layer under an applied electric field. High charge carrier mobility is desirable for achieving high drain-source current, for setting drain-source voltage and gate-source voltage towards this end.

ii) Threshold voltage (V_{Th}): V_{Th} is the minimum voltage required to turn the transistor on. It is influenced by various parameters including the doping level of OSC, contact resistance at the OSC/electrode interface and the thickness of the dielectric layer. The V_{Th} of OFETs can be determined experimentally from the transfer curve by extrapolating the linear region to the V_G axis.

iii) The on/off current ratio (I_{on}/I_{off}): I_{on}/I_{off} is the ratio of on-state current (when gate voltage is applied) and off-state current (in absence of an applied gate voltage) of OFETs. High I_{on}/I_{off} is desirable for achieving low power consumption and high signal-

to-noise ratio.

The last three decades has witnessed an intense research activity on the design and synthesis of OSC consisting of either π-conjugated small molecules or polymers with a specific focus on their charge transport characteristics. The advantages of small molecules relies on their easy purification which is key for forming crystalline films and single crystals. Hitherto, only a limited number of high performance P-type small molecules (*i.e.* pentacence, benzo[b]benzo[4,5]thieno[2,3-d]thiophene (BTBT), 2,6-diphenylanthracene (DPA)) and N-type small molecules (*i.e.* N,N'-dioctyl-3,4,9,10-perylenedicarboximide (PTCDI-C8), 4,8-bis[5-(4-cyano-3-alkylphenyl)-2-thienyl]benzo[1,2-c:4,5-c']bis [1,2,5] thiadiazole (TU-3)) has been designed and synthesized.

Based on alternating donor and acceptor building block, numerous D-A conjugated co-polymers have been designed and displayed exceptional charge transport characteristics. The energy level of their frontier orbitals (*i.e.* (highest occupied molecular orbital (HOMO) and lowest unoccupied molecular orbital (LUMO)) can be tuned by modulating the strength of electron-donating or electron-withdrawing units, enabling to simultaneously improve the efficiencies of charge injection and extraction (hole or electron) into and from the electrode.[10] Li *et al.* developed a very high molecular-weight polymer, poly(diketopyrrolopyrrole-co-dithienylthieno[3,2b]thiophene) (DPP-DTT), which could be solution-processed into an ambient-stable, high-performance OTFT devices with high hole mobility up to 10.5 $cm^2\ V^{-1}\ s^{-1}$ and I_{on}/I_{off} of 10^6.[11] Kim *et al.* introduced an easily synthesized D-A polymer, poly(thienoisoindigo-co-naphthalene) (PTIIG-Np). Thanks to its inherently large planarity and favorable energy levels for hole injection, OFET based on this polymer with an ultrahigh hole mobility of 14.4 $cm^2\ V^{-1}\ s^{-1}$ were demonstrated.[12] Different to semi-crystalline polymer, amorphous polymer, poly(indacenodithiophene-co-benzothiadiazole) (IDT-BT) were shown to display a high hole mobility over 1 $cm^2\ V^{-1}\ s^{-1}$ by Zhang *et al.*, which can be attributed to a greatest extent to an efficient

intramolecular charge transport.[13] Fluorine-(F-) substitution in polymers is a promising strategy to lower the frontier molecular orbital of D-A polymer, promoting electron injection at the electrode-semiconductor interface and leading to high electron mobilities. Yang *et al.* have reported a series of polymers based on the building block of F-substituted isoindigo and F-substituted bithiophene. Among them, poly(2F-substituted-isoindigo-co-2F-substituted-bithiophene) (P2FIID-2FBT) exhibited N-type dominant performance with an electron mobility of 9.70 cm^2 V^{-1} s^{-1}.[14] Via direct arylation polycondensation, Gao *et al.* have synthesized high performance polymer, poly(diketopyrrolopyrrole-co-(E)-1,2-bis(3,4-difluorothien-2-yl)ethene) (PDPP-4FTVT), with electron mobility of 5.86 cm^2 V^{-1} s^{-1}.[15] In 2016, Zheng *et al.* have reported a new building block, F_4BDOPV. Measurements carried out in air environment gave excellent electron mobilities of up to 14.9 cm^2 V^{-1} s^{-1}, as quantified in OFETs devices based on poly(3-((E)-5,7-difluoro-1,6-dimethyl-2-oxoindolin-3-ylidene)-7-((E)-5,7-difluoro-1-methyl-2-oxoindolin-3-ylidene)-3,7-dihydrobenzo[1,2-b:4,5-b']difuran-2,6-dione-co-bithiophene) (F_4BDOPV-2T).[16] In Figure 1-2, the chemical structures of small molecules and polymers displaying high mobility are displayed.

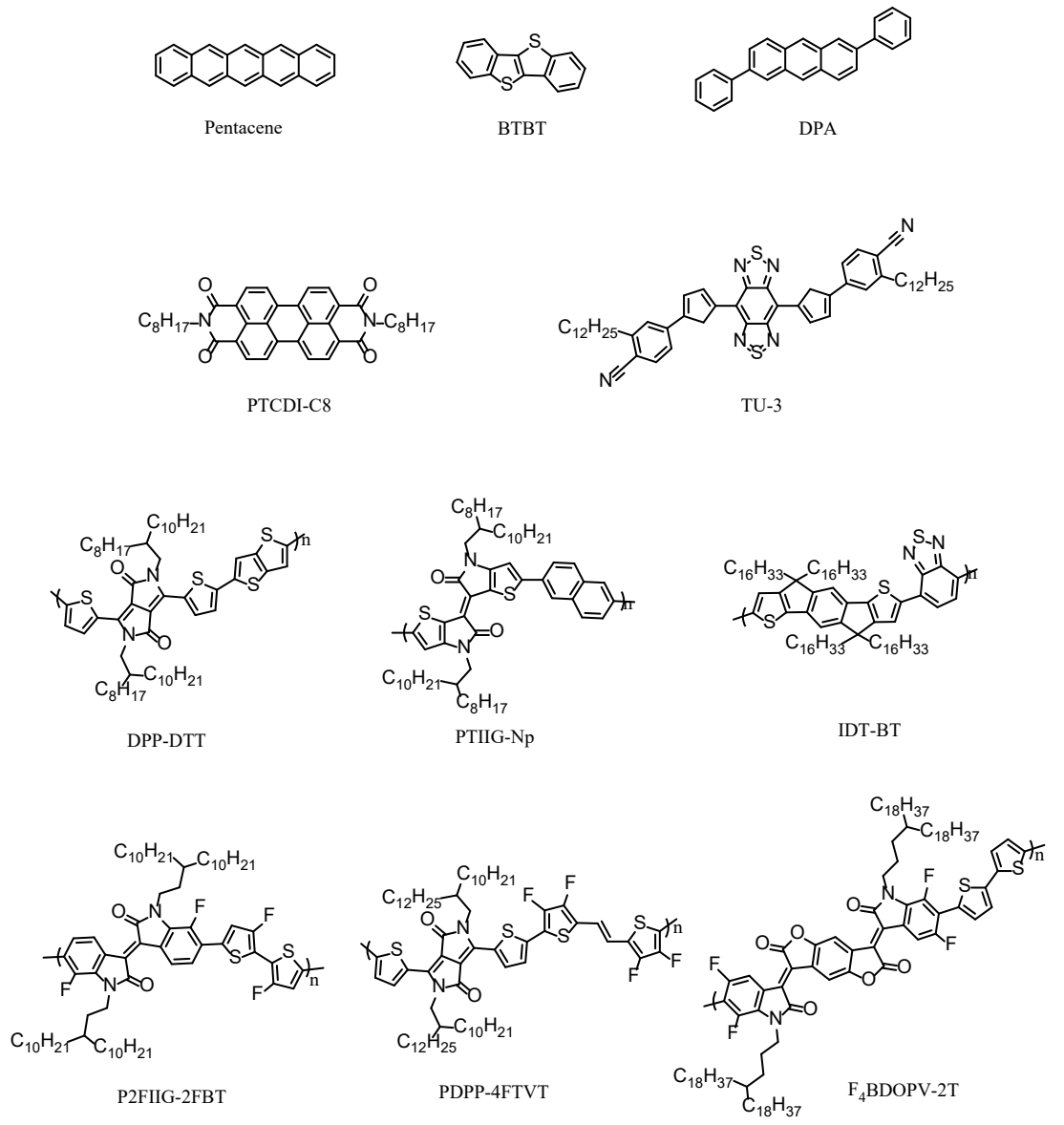

Figure 1-2. Chemical structure of high mobility π- conjugated small molecules and polymers.

Solubility and processability of D-A conjugated polymers depend on their molecular weight, which can be adjusted by tuning the kinetics of polymerization.[17-18] The purification of the D-A conjugated polymers and decrease in the polydispersity of molecular weight, can be achieved typically by the Soxhlet extraction method. For example, Yoon *et al.* separated poly(4-(4,4-bis(2-ethylhexyl)-4H-silolo[3,2-b:4,5-b′]dithiophen-2-yl)-7-(4,4-bis(2-ethylhexyl)-6-(thiophen-2-yl)-4H-silolo[3,2-b:4,5-

b′]dithiophen-2-yl)-5,6-difluorobenzo[c][1,2,5]thiadiazole) into three batches with different molecular weight by using as extraction solvent cyclohexane, dichloromethane, and chloroform, respectively.[19] Zhou *et al.* also purified the poly(dithieno[2,3-d;2′,3′-d']benzo[1,2-b;4,5-b′]dithiophene-co-dithieno[3′,2′:3,4;2″,3″:5,6]benzo[1,2-c][1,2,5]-thiadiazole) according to various polymers' solubility in extraction solvents of chloroform dichloromethane and chlorobenzene, respectively.[20] As a result, conjugated polymers were obtained with low, medium and high molecular weight. Since polymer with high molecular weight can only dissolved in strongly polar solvents, polymers with different molecular weight can be also employed for solution-processed multilayer deposition. In particular, D-A conjugated polymers with low molecular weight can be dissolved in solvent with low polarity and then spin-coated on the top of that with higher molecular weight.

1.2. Aim and Structure of the Thesis

In recent years, the integration of multiple functions into in organic optoelectronics has represented a major step forward towards the implementation of smart devices technologies. Such multifunctional nature can be achieved by increasing the functional complexity in electronic devices and by combining components that are able to impart a distinct function to the ensemble. OFETs represent the ideal platform for studying multifunction integration.[21-23]

The goal of this thesis consists in the integration of switching function, memory function and the light emission function into single devices, which can be applied as long afterglow display, optically switchable display, and some other optical telecommunication. Towards this end, multilayer OFETs perform as an ideal platform for studying memory display, as shown in Figure 1-3. In this kind of structure, gate electrode, dielectric layer, channel layer, interface layer and emission layer should be deposited sequentially. Asymmetric electrode with high work function and low work function should be deposited as drain electrode and source electrode for optimized hole

and electron injection, respectively. The operating mechanism can be summarized as follow: Firstly, the memory function can be introduced into the channel layer or dielectric layer for controlling the drive current, which responds to different inputs, such as light, voltage, pressure, magnetic field, etc. Then, non-volatile or volatile changes of conductivity in the semiconductor characteristics lead to a change in the current powering the light emission layer. Finally, light emission in OLETs exhibits a responsive memory display. It is worth pointing out that the choice of light-emitting materials is not limited to organic molecules. In the future, other types of light-emitting materials, including quantum dots, perovskites and transition metal chalcogenides, can be also employed towards the same goal.

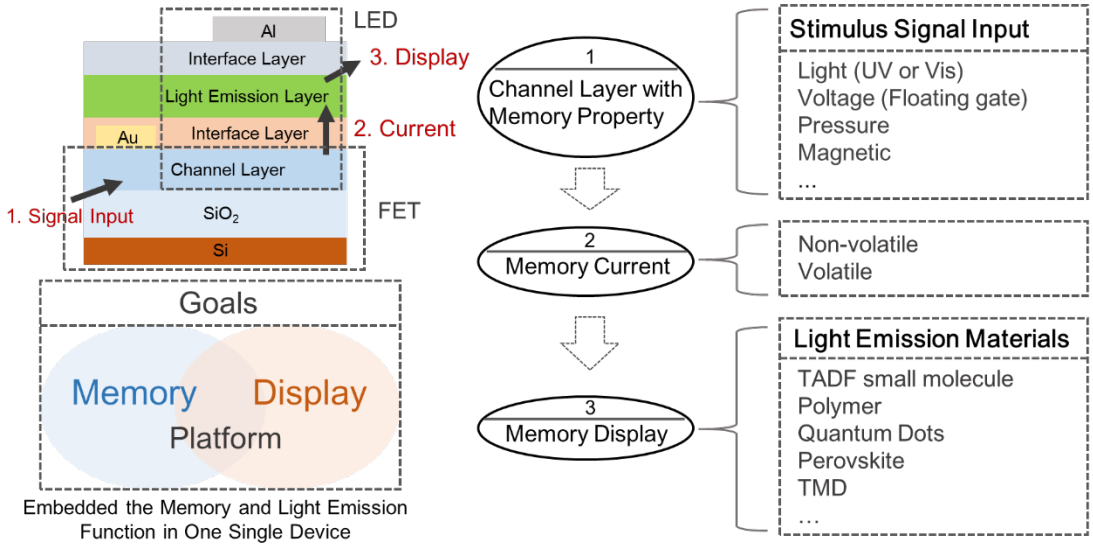

Figure 1-3. Strategy illustration of memory organic light-emitting transistors, achieved in this thesis.

This thesis is given in 8 chapters as follows:

Chapter 1 provides a brief introduction to the OFET and to the design principle of long afterglow OLETs (LAOLETs). It also offers an outline of the thesis work.

Chapter 2 presents a brief theoretical background of the OMTs. OMTs are three-terminal devices whose electrical output can be controlled by applying an electric field

to the active channel via the third electrode, with the current flowing. Depending on different operating mechanism, the architecture of memory transistors are designed as floating gate transistors, ferroelectric transistors, electret gate transistors and optical transistors. In particular, synaptic memory devices been considered as next-generation memory devices, which hold on potential in neuromorphic engineering and artificial intelligence.

Chapter 3 provides a brief theoretical background of the OLETs. To maximize the quantum efficiency in the light-emitting devices, the organic emissive molecules have been designed to utilize more excitons, from fluorescence molecules to phosphorescence molecules and thermally activated delayed fluorescence (TADF) molecules. Concerning the OLETs device architecture, single-layer and multilayer devices display unsatisfactory linear light emission, which limits their performance. Conversely, hybrid structures and vertical structures have been successfully employed to achieve large-area and high light emission characteristics.

Chapter 4 focuses on the fabrication and characterization of synaptic transistors based on inorganic metal oxide of indium-gallium-zinc oxide (IGZO). Powered by post-synaptic current, LAOLETs trigged by UV pulse have been fabricated and characterized subsequently.

Chapter 5 introduces the use of gold nanoparticles as floating gate to realize synaptic OFETs. Electrically trigged LAOLETs were fabricated and displayed two operating modes, being stimulated by positive gate electric spiked and negative electric spiked, respectively.

Chapter 6 introduces the use of high *k* materials, lanthanum-aluminum oxide ($LaAlO_x$), as dielectric layer to achieve low-voltage synaptic transistor. Moreover, low-voltage LAOLETs were also fabricated successfully, which operation voltage is around 12 V.

In Chapter 7, two proof-of-concept practical applications of the LAOLETs

including visual UV sensors array and long afterglow pressure sensor are presented.

Chapter 8 draws the conclusions of this thesis work, discussing the short-term and long-term perspectives of LAOLETs.

1.3. Reference

1. Ren, Y.; Yang, X.; Zhou, L.; Mao, J. Y.; Han, S. T.; Zhou, Y., Recent Advances in Ambipolar Transistors for Functional Applications. *Advanced Functional Materials* **2019,** *29* (40), 1902105.

2. Shi, W.; Guo, Y.; Liu, Y., When Flexible Organic Field-Effect Transistors Meet Biomimetics: A Prospective View of the Internet of Things. *Advanced Materials* **2020,** *32* (15), e1901493.

3. Ditte, K.; Nguyen Le, T. A.; Ditzer, O.; Sandoval Bojorquez, D. I.; Chae, S.; Bachmann, M.; Baraban, L.; Lissel, F., Rapid Detection of SARS-CoV-2 Antigens and Antibodies Using OFET Biosensors Based on a Soft and Stretchable Semiconducting Polymer. *ACS Biomaterials Science & Engineering* **2021**, DOI: 10.1021/acsbiomaterials.1c00727.

4. Liu, H.; Yang, A.; Song, J.; Wang, N.; Lam, P.; Li, Y.; Law, H. K.-w.; Yan, F., Ultrafast, Sensitive, and Portable Detection of COVID-19 IgG Using Flexible Organic Electrochemical Transistors. *Science Advances* **2021,** *7* (7), eabg8387.

5. Zheng, L.; Li, J.; Zhou, K.; Yu, X.; Zhang, X.; Dong, H.; Hu, W., Molecular-Scale Integrated Multi-Functions for Organic Light-Emitting Transistors. *Nano Research* **2020,** *13* (7), 1976-1981.

6. Griggs, S.; Marks, A.; Bristow, H.; McCulloch, I., N-Type Organic Semiconducting Polymers: Stability Limitations, Design Considerations and Applications. *Journal of Materials Chemistry C* **2021,** *9* (26), 8099-8128.

7. Guo, X.; Baumgarten, M.; Müllen, K., Designing π-conjugated Polymers for

Organic Electronics. *Progress in Polymer Science* **2013,** *38* (12), 1832-1908.

8. Yu, Y.; Ma, Q.; Ling, H.; Li, W.; Ju, R.; Bian, L.; Shi, N.; Qian, Y.; Yi, M.; Xie, L.; Huang, W., Small-Molecule-Based Organic Field-Effect Transistor for Nonvolatile Memory and Artificial Synapse. *Advanced Functional Materials* **2019,** *29* (50), 1904602.

9. Liu, C. F.; Liu, X.; Lai, W. Y.; Huang, W., Organic Light-Emitting Field-Effect Transistors: Device Geometries and Fabrication Techniques. *Advanced Materials* **2018,** *30* (52), e1802466.

10. Kim, M.; Ryu, S. U.; Park, S. A.; Choi, K.; Kim, T.; Chung, D.; Park, T., Donor-Acceptor-Conjugated Polymer for High-Performance Organic Field-Effect Transistors: A Progress Report. *Advanced Functional Materials* **2019,** *30* (20), 1904545.

11. Li, J.; Zhao, Y.; Tan, H. S.; Guo, Y.; Di, C. A.; Yu, G.; Liu, Y.; Lin, M.; Lim, S. H.; Zhou, Y.; Su, H.; Ong, B. S., A Stable Solution-Processed Polymer Semiconductor with Record High-Mobility for Printed Transistors. *Scientific Reports* **2012,** *2*, 754.

12. Kim, G.; Kang, S. J.; Dutta, G. K.; Han, Y. K.; Shin, T. J.; Noh, Y. Y.; Yang, C., A Thienoisoindigo-Naphthalene Polymer with Ultrahigh Mobility of 14.4 $cm^2/V{\cdot}s$ that Substantially Exceeds Benchmark Values for Amorphous Silicon Semiconductors. *Journal of the American Chemical Society* **2014,** *136* (26), 9477-9483.

13. Zhang, W.; Smith, J.; Watkins, S. E.; Gysel, R.; McGehee, M.; Salleo, A.; Kirkpatrick, J.; Ashraf, S.; Anthopoulos, T.; Heeney, M.; McCulloch, I., Indacenodithiophene Semiconducting Polymers for High-Performance, Air-Stable Transistors. *Journal of the American Chemical Society* **2010**, *132* (33), 11437–11439.

14. Yang, J.; Zhao, Z.; Geng, H.; Cheng, C.; Chen, J.; Sun, Y.; Shi, L.; Yi, Y.; Shuai, Z.; Guo, Y.; Wang, S.; Liu, Y., Isoindigo-Based Polymers with Small Effective Masses for High-Mobility Ambipolar Field-Effect Transistors. *Advanced Materials* **2017,** *29* (36), 1702115.

15. Gao, Y.; Zhang, X.; Tian, H.; Zhang, J.; Yan, D.; Geng, Y.; Wang, F., High Mobility Ambipolar Diketopyrrolopyrrole-Based Conjugated Polymer Synthesized Via Direct Arylation Polycondensation. *Advanced Materials* **2015,** *27* (42), 6753-6759.

16. Zheng, Y. Q.; Lei, T.; Dou, J. H.; Xia, X.; Wang, J. Y.; Liu, C. J.; Pei, J., Strong Electron-Deficient Polymers Lead to High Electron Mobility in Air and Their Morphology-Dependent Transport Behaviors. *Advanced Materials* **2016,** *28* (33), 7213-7219.

17. Pei, D.; Wang, Z.; Peng, Z.; Zhang, J.; Deng, Y.; Han, Y.; Ye, L.; Geng, Y., Impact of Molecular Weight on the Mechanical and Electrical Properties of a High-Mobility Diketopyrrolopyrrole-Based Conjugated Polymer. *Macromolecules* **2020,** *53* (11), 4490-4500.

18. Kline, R. J.; McGehee, M. D.; Kadnikova, E. N.; Liu, J.; Fréchet, J. M. J., Controlling the Field-Effect Mobility of Regioregular Polythiophene by Changing the Molecular Weight. *Advanced Materials* **2003,** *15* (18), 1519-1522.

19. Yoon, S. E.; Kim, B.; Chun, S. Y.; Lee, S. Y.; Jeon, D.; Kim, M.; Lee, S.; Seo, B. E.; Choi, K. S.; Kim, F. S.; Kim, T.; Seo, H.; Kwak, K.; Kim, J. H.; Kim, B., Impact of Molecular Weight on Molecular Doping Efficiency of Conjugated Polymers and Resulting Thermoelectric Performances. *Advanced Functional Materials* **2022,** *32* (32), 2202929.

20. Zhou, J.; Guo, Q.; Zhang, B.; Cheng, S. X.; Hao, X. T.; Zhong, Y.; Tang, A.; Sun, X.; Zhou, E., Improving the Photovoltaic Performance of Dithienobenzodithiophene-Based Polymers via Addition of an Additional Eluent in the Soxhlet Extraction Process. *ACS Applied Materials & Interfaces* **2022,** *14* (46), 52244-52252.

21. Feiner, R.; Engel, L.; Fleischer, S.; Malki, M.; Gal, I.; Shapira, A.; Shacham-Diamand, Y.; Dvir, T., Engineered Hybrid Cardiac Patches with Multifunctional Electronics for Online Monitoring and Regulation of Tissue Function. *Nature Materials*

2016, *15* (6), 679-685.

22. Gouder, A.; Podjaski, F.; Jimenez-Solano, A.; Kroger, J.; Wang, Y.; Lotsch, B. V., An Integrated Solar Battery Based on A Charge Storing 2D Carbon Nitride. *Energy & Environmental Science* **2023,** *16* (4), 1520-1530.

23. Zhang, Y.; Huo, Z.; Wang, X.; Han, X.; Wu, W.; Wan, B.; Wang, H.; Zhai, J.; Tao, J.; Pan, C.; Wang, Z. L., High Precision Epidermal Radio Frequency Antenna via Nanofiber Network for Wireless Stretchable Multifunction Electronics. *Nature Communications* **2020,** *11* (1), 5629.

Chapter 2. Organic Memory Transistors

2.1. Background of OMTs

Memory devices have a paramount importance in modern electronic devices including smartphones, computers and data centers, as they allow users to access, store and process information quickly and efficiently. With the advent of the Internet of Things, 5G, big data, and artificial intelligence, the memory devices market has entered a new round of explosive growth.

Memory devices are operated by modifying the resistance of materials, enabling the storage and retrieval of data, wherein high and low voltages correspond to a 1 or a 0. Hitherto, three generation of storage technologies have been devised which differ on the type of input exploited to store data, *i.e.* magnetic, optical and electrical. The most common type of data storage devices used in computers and servers, e.g. in hard disk drives (HDDs), relies on magnetic field to modulate the resistance of materials inside devices. Optical writing is employed in compact discs (CDs) and digital versatile discs (DVDs), being an affordable and efficient technology. The electrical resistance of optically responsive molecules can be written and read by a laser. Solid state drives (SSDs) based on memristor or FETs allow the use of parallel processing to read and write data into multiple memory cells simultaneously, exhibiting a faster and more reliable process compared to HDDs that need spinning disks to access data.[1]

Three-terminal memory unit based on FETs can sufficiently circumvent the adjacent cell crosstalk problem, which in commonly found in two-terminal memory unit based on memristor, leading an improvement on stability of memory storage. In order to facilitate the commercialization of the next-generation of flexible radio frequency identification tags, integrated circuits and portable electronics, memory transistors based on OSC have been developed. Organic memory transistors (OMTs) have gained significant attention in recent years due to their potential applications in

various fields such as flexible electronics, wearable devices, artificial intelligence, and biosensors.[2] The key parameters of OMTs include:

i) Memory window (ΔV_{Th}): ΔV_{Th} of OMT indicates the operability of devices, which can be determined by the shift of V_{Th}, from the hysteresis transfer curves of transistors.

ii) Programed/erased current ratio ($I_{P/E}$): $I_{P/E}$ is the ratio of programed current (after programed signal stimulus) and erased current (after erased signal stimulus) of OMTs. $I_{P/E}$ should be high for distinguishing the data, but limited by the I_{on}/I_{off} of transistors.

iii) Memory storage time (known also as retention time): OMTs can be classified as either non-volatile or volatile devices according to their memory storage retention time, which refers to how long memory current remains at a high level. Although a precise value of time storage is absent defining memory as non-volatile or volatile, OMTs with a memory storage time in the range of seconds are generally considered as volatile ones. It is worth pointing out that OMTs displaying volatile feature are particularly desirable and well-suited for neuronal emulation.

2.2. Synaptic Memory Transistors

The von Neumann computer architecture is the basis for modern digital computers; it was proposed by mathematician and physicist John von Neumann in the late 1940s. Based on this concept, memory storage space (drives) and the computational processing space (CPU) in computer are separated. Data exchange between storage and processing units is done through a communication pathway, slowing down the system and determining a highly energy consumption. The rise of big data has brought about an unprecedented growth in data processing, posing significant challenges to the energy efficiency and processing speed of data-centric tasks. In this context, the limitations of traditional von Neumann digital computers have become increasingly evident.

Conversely, human brain is a highly efficient and low energy consumption system,

which compute and store information at the same time. Inside the brain there are a large amount of synapses (about 10^{15}), which are the junctions responsible for data communication between two neurons.[3] Neurotransmitters (*i.e.* Ca^{2+}, Na^{+}) are released from axon terminal of the presynaptic neuron into the synaptic cleft under an action potential input, and then diffuse across the gap to bind with receptor molecules on the postsynaptic neuron's dendrite or cell body, causing a change in the post-synaptic neuron's membrane potential. Synaptic plasticity controls how effectively two neurons communicate with each other; it can be increased or decreased depending on the frequency and timing of their activity, which is not fixed but can modulated by the amount of neurotransmitter. Based on synaptic plasticity, the brain processes data and information, wherein the memory function and calculation function are ruled by the "in-memory" computing system.[4,5]

Neuromorphic engineering and artificial intelligence demand hardware elements that emulates synapse algorithms. During the last decade, OMT based on OSC have been explored as a platform for artificial synapses for neuromorphic computing. Organic synaptic transistor is a device that can be used to mimic the behavior of synapses in artificial neural networks, as shown in Figure 2-1.[6,7] As pre-electrical signal input through gate terminal, one can use the change in resistance of OSC in response to post-electrical drain-source current output. Synaptic plasticity is of elemental significance for mimicking sensory perceptions such as learning, remembering, and forgetting. Organic synaptic transistor operates via the controlled occurrence of presynaptic events, with postsynaptic current (PSC) being the output enabling quantitative monitoring of the process. For example, facilitation can be achieved by repetitive presynaptic stimuli which allow to enhance ultrafast synaptic transmission and memory consolidation. Conversely, the opposite process is depression, which represents an inhibitory operation, avoiding over excitation and maintaining the stability of neural networks.[8]

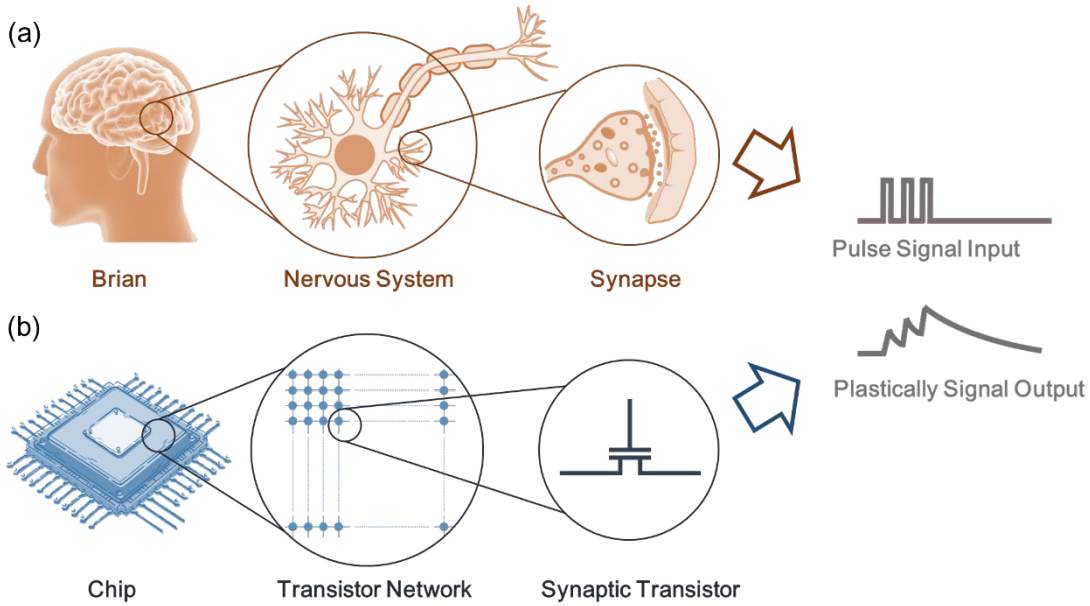

Figure 2-1. In order to mimic the function of (a) human brain, (b) artificial neuromorphic computing is designed as a cross-bar array network composited by synapse devices.

Artificial synapse aims to mimic two fundamental synaptic functions in biological neural networks: spike-timing-dependence-plasticity (STDP), and short-term memory (STM) to long-term memory (LTM) transition. The strength of PSC is modulated by the pre-synapse pulse strength, frequency, and width. In particular, repeated pre-synapse pulse with more powerful strength, faster frequency or wider width yield higher post-synaptic response. Short-to-long term transition is described, the retention time of PSC can transit from second level to day level or even month level after the rehearsal of pre-synaptic stimulation, being related to the important brain function of training to learning process.[9]

Paired-pulse facilitation (PPF) and paired-pulse depression (PPD) are dynamic enhancement or decline of neurotransmitter release, which are crucial in information processing in biological neural systems. PPF/PPD can be estimated from a pair of PSC under a pair of pre-synaptic signal input. PPF/PPD is a phenomenon where the second

of two closely spaced identical stimuli produces a larger/smaller response than the first one, which can be estimated by the ratio of PSC response to pulse 2 divided by the PSC responded to pulse 1. PPF/PPD index gradually decreases with the increasing time interval (Δt) between the pair of pulses. The decay trend of PPF/PPD can be fitted by exponential decay function: PPF/PPD index = $C_0 + C_1 \times \exp(-\Delta t/\tau_1) + C_2 \times \exp(-\Delta t/\tau_2)$, where C_1 and C_2 are the initial facilitation magnitudes of the rapid and slow phases, respectively; τ_1 and τ_2 are the characteristic relaxation times of the rapid and slow phases, respectively.

Yang *et al.* have developed InSe-based artificial synaptic transistor, wherein InO_x served as an effective charge trapping layer toward synaptic function (Figure 2-2a). Gate voltage bias applied as pre-synaptic signal input and the conductance of channel changing for mimic the variation of post-synaptic weight. Charge trapping (hole carrier here) by InO_x layer leads to an increase of synaptic weight to implement facilitation. Conversely, de-trapping process can be used to trigger depression. Figure 2-2b displays the spike-time-dependence facilitation/depression, which is consistent with Hebbian synaptic learning rules. Nonlinear synaptic weight variation was extracted from conductance of InSe under 100 continuous input spikes, as shown in Figure 2-2c. An artificial network based on the property parameter of InSe-based artificial synaptic transistor has been successfully simulated for system-level pattern recognition.[10]

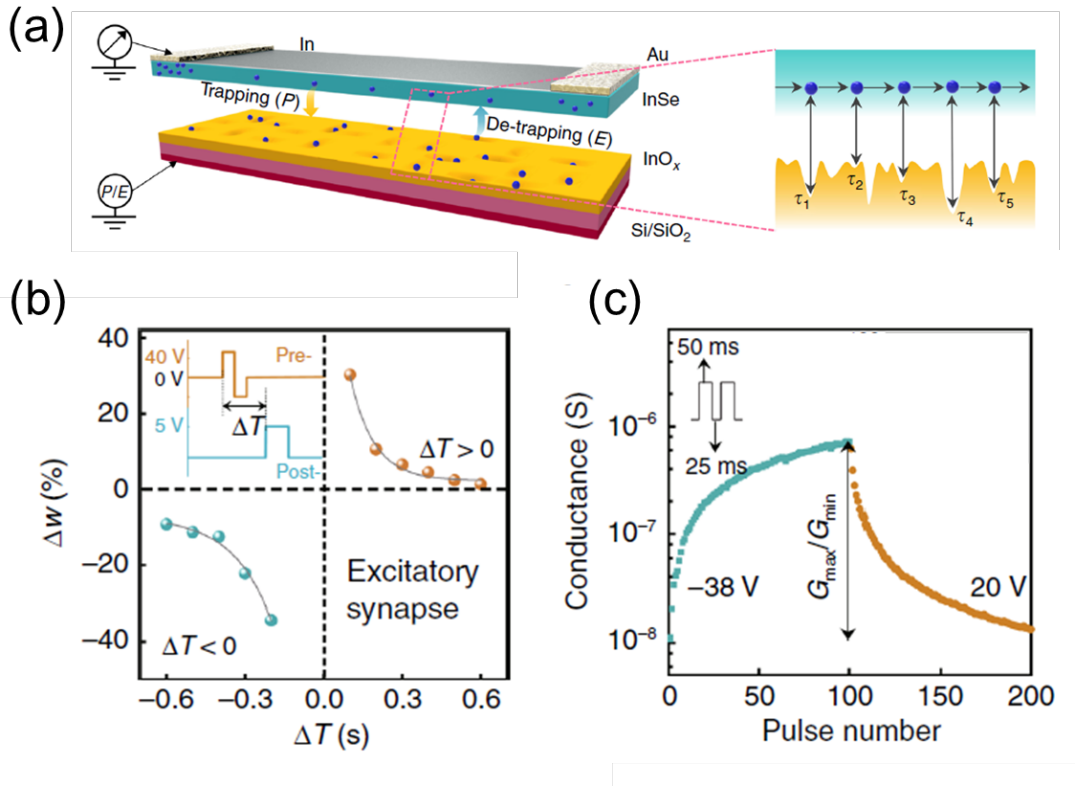

Figure 2-2. (a) Schematic of device structure of InSe-based artificial synaptic transistor. (b) PPF/PPD index (change value of synaptic weight, Δw) depending on the time interval (ΔT) and the corresponding fitted curves based on the exponential functions. (c) The facilitation and depression synaptic weight states mimicked by the conductance variation of InSe.[10]

2.3. Architecture and Memory Mechanism of OMTs

Three kinds of device architectures have been developed for electrical-spiked OMTs, *i.e.* floating gate OMTs, ferroelectric OMTs and electret OMTs, as illustrated in Figure 2-3a to 2-3c. The hysteresis in the transfer curves of these OMTs are markedly different. The transfer curves of floating gate OMTs present from-top-to-bottom direction (Figure 2-3d). In particular, the curves sweep as anticlockwise direction in negative V_G and as clockwise direction in positive V_G. Conversely, the transfer curves of ferroelectric OMTs and electret OMTs display a from-bottom-to-top direction

(Figure 2-3e). If one compares the electrical-programing operation in electrical-spiked OMTs, optical-spiked OMTs guarantee high density and multilevel data storage, wherein the write/read processing are orthogonal.[11]

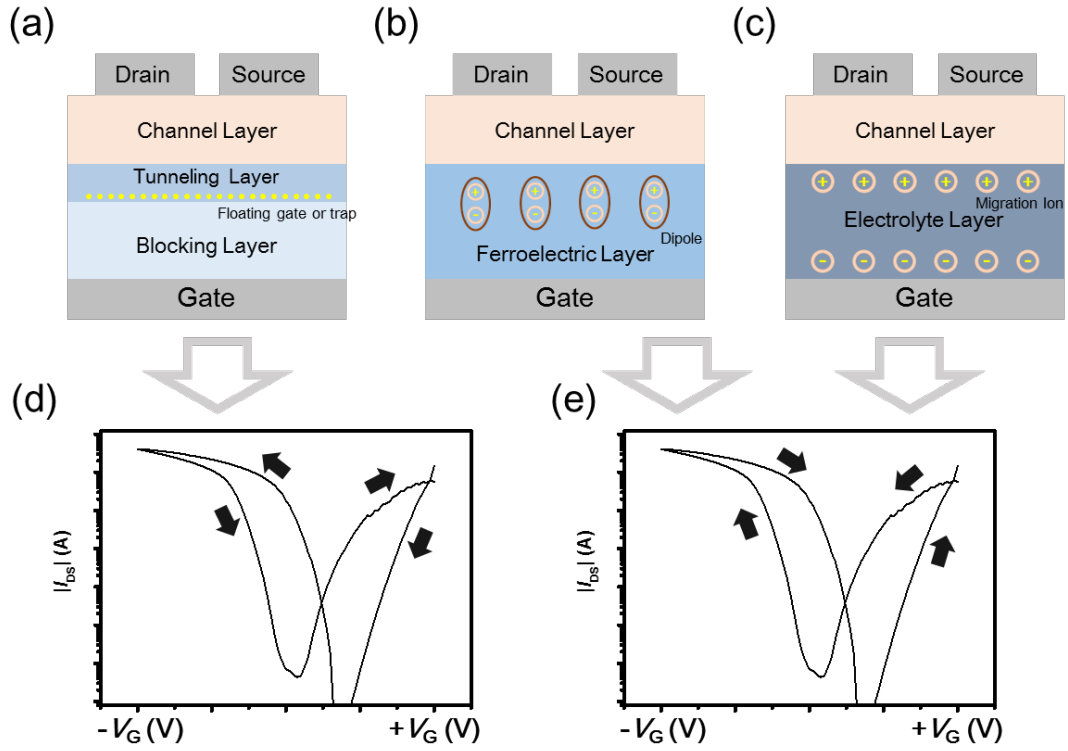

Figure 2-3. Three devices' architectures for OMTs: (a) floating gate OMTs, (b) ferroelectric OMTs, (c) electrolyte OMTs. (d,e) Two different hysteresis of transfer curve in OMTs.

2.3.1. Floating Gate OMTs

If one considers P-type devices, the working mechanism floating gate OMTs can be explained as follows: Electron from channel layer can be injected into the floating gate/trap through tunneling layer when a positive gate voltage is applied to the floating gate OMTs, and be stored intactly once this positive gate is removed, yielding an enhancement of conductivity of channel layer. When a negative gate voltage is applied, holes can be injected into the floating gate/trap and balance the storage electron. Such processes perform as write/erase of devices.[12]

Metal nanoparticles have been widely utilized in floating gate OMTs. Using poly ((N,N′-bis(2-octyldodecyl)-naphthalene-1,4,5,8-bis(dicarboximide)-2,6-diyl)-alt-5,5′-(2,2′-bithiophene)) P(NDI2OD-T2) as channel layer and polystyrene/poly(methyl methacrylate) (PS/PMMA) as dielectric layer, OMTs with different floating gate based on different thermal evaporated metal (Au, Ag, Cu, or Al) nanoparticles (NPs) have been compared by Kang *et al.*[13] The TEM images of these metallic NPs with 1.0 nm thermally grown thickness are shown in Figure 2-4a. Au NPs-based and Cu NPs-based OMTs displayed largest ΔV_{Th} of 45 V and longest storage time of 10^8 s, respectively. Furthermore, carbon materials can also perform as floating gate in OMTs. Sputtered carbon NPs (C NPs) have been also demonstrated operating as the floating gate by Liu *et al.*[14] The morphology of sputtered carbon with the sputtering time of 1 min and 2 min were evaluated by AFM. PS dissolved in toluene was spin-coated on the top of the C NPs to form a fully-covered tunneling layer, which were displayed in Figure 2-4b. Utilizing pentacene and N,N′-ditridecyl-3,4,9,10-perylenetetracarboxylic diimide (PTCDI-$C_{13}H_{27}$) as channel layer, P-type and N-type floating gate OMTs were fabricated successfully, which exhibited excellent ΔV_{Th} of 35 V and 60 V, respectively. Using fullerene/PMMA hybrid layer, Ren *et al.* fabricated low voltage flexible OMTs, which displayed a ΔV_{Th} of 2.95 V, $I_{P/E}$ of 10^3 and program/erase endurance cycle over 500 times.[15]

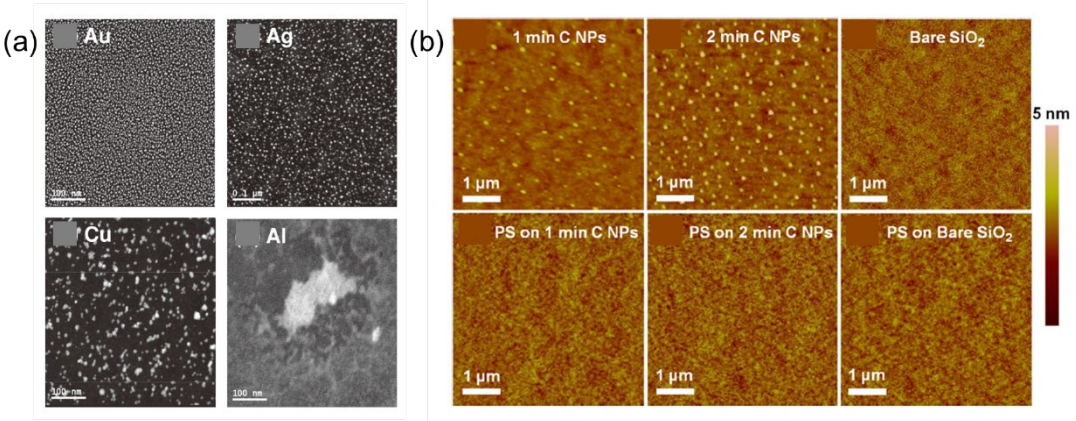

Figure 2-4. (a) TEM image of various metallic NPs.[13] (b) AFM image indicated the

morphology of sputtered carbon NPs with different condition and the PS layer covered on them.[14]

Differently from conducting materials, solution blending the OSC and insulation layer can be also operated as a floating gate. Higashinakaya *et al.* demonstrated that organic composite of PS and 6,13-bis(triisopropylsilylethynyl)pentacene (TIPS-pentacene) can be also forming an organic floating gate for top-gate bottom-contact OMTs which employed bipolar polymer, DPP-DTT, as channel layer.[16] DPP-DTT exhibited an excellent electron transport mobility and deep LUMO level of −3.5 eV, rendering it an ideal interlayer component in-between the Au source/drain electrodes and TIPS-pentacene, ensuring optimal electron injection from the Au electrodes, through the DPP-DTT, into the LUMO level of TIPS-pentacene floating gates under programmed gate voltage (Figure 2-5a and 2-5b). Similarly, Shih *et al.* also reported the incorporation of poly(methacrylic acid) (PMAA) and poly (9,9-dioctylfluorenyl-2,7-diyl) (PF) or poly[(9,9-dioctylfluorenyl-2,7-diyl)-alt-(benzo[2,1,3]thiadiazol-4,8-diyl)] (PFBT) as discrete trapping sites for the fabrication of OMTs.[17] The process exploited for the fabrication is portrayed in Figure 2-5c: Polymer NPs were generated by solvent-induced precipitation method by dropping a dilute solution of corresponding π-conjugated polymer into deionized water.

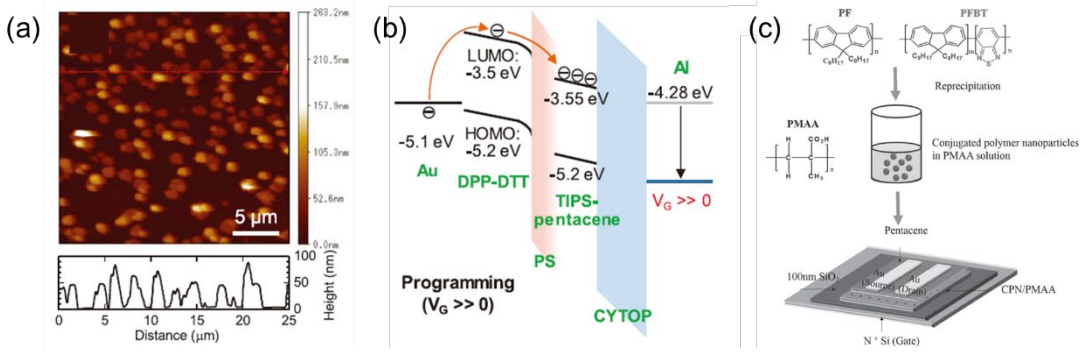

Figure 2-5. (a) AFM images of the PS:TIPS-pentacene (80:20) composite film in OSC-based floating gate OMTs and (b) work mechanism of these OMTs.[16] (c) Schematic of fabrication process of PF/PFBT NPs blending PMAA.[17]

Recently Wang *et al.* utilized the bicomponent of poly(vinyl pyrrolidone) (PVP) and perovskite ($CsBi_3I_{10}$) as photoactive material to fabricate floating gate OMTs, which can be programed by light and erased by electrical signal.[18]

2.3.2. Ferroelectric OMTs

The working mechanism in ferroelectric OMTs relies on the capacity to polarize ferroelectric materials, by exploiting their non-centrosymmetric structure. When a gate voltage is applied, the dipoles within the ferroelectric layer align in a specific direction, which is determined by the position of the displaced atoms within the (macro)molecule or material thereof. After removal of the gate voltage, this polarization effect is kept thereby enabling a memory retention.[19] The ferroelectricity of ferroelectric materials can be identified by ferroelectric hysteresis loops (*P*–*E* curve), as shown in Figure 2-6a. In this typical hysteresis loop curve, saturation polarization (P_s) region is achieved when all the dipoles in the materials are polarized, with the remanent polarization (P_r) region representing the maintaned polarization value at zero voltage after removal of the applied bias, whereas the coercive field (E_c) is the threshold electric field voltage for triggering the switch of the polarization direction in the (macro)molecule or material.[20]

Organic ferroelectric polymers are worth being explored as a strong dielectric layer for ferroelectric OMTs because they hold some advantages including their excellent chemical stability, facile solution-based processibility, large retention polarization and high dielectric constant. Schroeder *et al.* published the first ferroelectric OMTs in 2004, by using nylon polymer and poly(mxylylene adipamide) (MXD6) as a dielectric layer and pentacene as a channel layer.[21] Ferroelectric polymer synthesized from monomer 1,1-difluoroethylene (VDF) by free radical polymerization have drawn a great deal of attention because of the high vacuum dipole moment of 7.07×10^{-30} C·m generated by the potential difference between positively charged H atom and negatively charged F atoms in a lattice structure.[22] There are various molecular conformations in VDF-based

polymer, such as trans-gauche-trans-gauche′ (TGTG′), trans-trans-trans-gauche (TTTG) and all-trans (TTTT), which are packed into at least four distinct crystalline phases including the α, β, γ and δ phases (Figure 2-6b).[23] Theoretically, the β phase of VDF-based polymer exhibited largest spontaneous polarization of 13 μC cm^{-2} caused by the alignment of molecular dipoles along the same direction, which is superior compared with other crystal phases. Moreover, the dielectric constant (k) of poly(vinylidene fluoride) (PVDF), poly(vinylidene fluoride-co-trifluoroethylene) (P(VDF-TrFE)) and poly(vinylidene fluoride-trifluorethylene-chlorofluoroethylene) (P(VDF-TrFE-CFE)) amounts to 8, 11, and 60 respectively, demonstrating a huge potential for low voltage OMTs application.

Upon using P(VDF-TrFE) as ferroelectric layer and poly(1,4-phenylene-vinylene) (MEH-PPV) as semiconductor material, Naber *et al*. demonstrated a flexible, rewritable, non-volatile ferroelectric OMTs, which presented excellent $I_{P/E}$ of 10^3, long memory storage time (stable for a week), high programming cycle endurance (over 1000 cycles) and fast programming time (around 10^3 sec).[24] Similarly, Kang et al. developed single crystal ferroelectric OMTs wherein a single crystal of tri-isopropylsilylethynyl pentacene (TIPS-PEN) deposited as the active layer, which is environmentally stable for more than 40 days without additional passivation.[25]

Inorganic material including metal oxide (HfO_x, $HfZrO_x$) and perovskites ($PbTiO_3$, $PbZrO_3$) have been also suggested to display promising ferroelectric properties yielding ferroelectric inorganic memory transistors.[26-29] On the other hand, the combination of inorganic ferroelectric materials and OSC for the fabrication of ferroelectric OMTs is under explored.

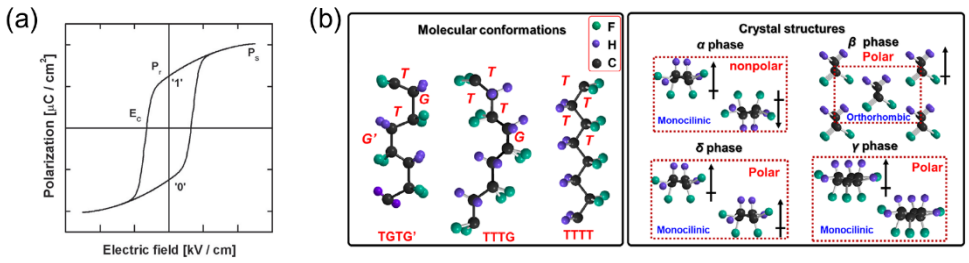

Figure 2-6. (a) The ferroelectric hysteresis loop of a ferroelectric materials-based capacitor.[19] (b) Molecular conformations of VDF-based polymer and the general crystal forms in them. Only α phase display a net zero dipole moment due to the antiparallel packing of the TGTG′ conformation.[23]

2.3.3. Electrolyte OMTs

The operation of electrolyte OMTs relies on the moving ions in electrolyte layer. Positive/negative charges in electrolyte layer move oppositely under the applied gate voltage, and then accumulate at the interface between the electrolyte/OSC and electrolyte/electrode, forming an electron-double layer (EDL) or directly penetrate into the OSC layer yielding a redox/oxide reaction, which can be categorized into two types: electrostatic modulation or electrochemical doping. Irreversible or partially reversible charge movement after gate voltage removal result in memory behavior of the electrolyte OMTs.[30]

Polymer-based electrolytes display some advantages including it solution-proccessability, extremely high capacitance around 10 μF cm^{-2} and versatile manufacturing. Huang *et al.* mixed bis-(trifluoromethane) sulfonimide lithium salt (LiTFSI) with polyvinyl alcohol (PVA) as the electrolyte insulation for strengthen the formation of EDLs in electrolyte OMTs, which enables a remarkable modulation of the memory current.[31] Chen *el al.* demonstrated stretchable electrochemical OMT based on prestretched honeycomb OSC of poly(2,5-bis(2-octyldodecyl)-3,6-di(thiophen-2-yl)-2,5-diketo-pyrrolopyrrole-alt-2,5-bis(3-triethyleneglycoloxy-thiophen-2-yl) (DPP-g2T)

as channel layer and aqueous KPF_6 as electrolyte, which exhibits stable output current under biaxial stretching of up to 30–140%.[32]

Interestingly, electrostatic modulation and electrochemical doping can be achieved into a single device. Yu *et al.* developed bi-modal electrolyte OMTs with two regimes of ion dynamic processes. As presented in Figure 2-7a, in the bottom-gate top-contact transistors, the PVA combined with malic acid served as electrolyte layer and the poly[2,5-bis(2-decyltetradecyl)pyrrolo[3,4-c]pyrrole-1,4(2H,5H)-dione-alt-5,50-di(thiophene-2-yl)-2,20-(E)-2-(2-(thiophen-2-yl)vinyl)-thiophene] (PVDF-10) served as channel layer. As illustrated in Figure 2-7b, when a negative gate voltage below the threshold voltage (ca. 1 V) was applied, free hydrogen ions and anions accumulate oppositely at the Si/PVA and PVA/PDVT-10 interfaces, respectively, yielding the formation EDL and facilitated PSC to 3 nA. However, when a negative gate voltage higher than threshold voltage (ca. 5 V) was applied, anions migrated towards PVDF-10 crossed the interface, resulting electrochemical doping and thus strengthening the PSC to 300 nA, also presenting longer retention time. Such bi-mode electrolyte OMTs can be utilized to mimic the nociceptive behavior (Figure 2-7c). Spike input with strength lower than threshold value yields short-term potential (STP) or fast pain, while a stronger spike stimulus will lead long-term potential (LTP) or injury pain.[33]

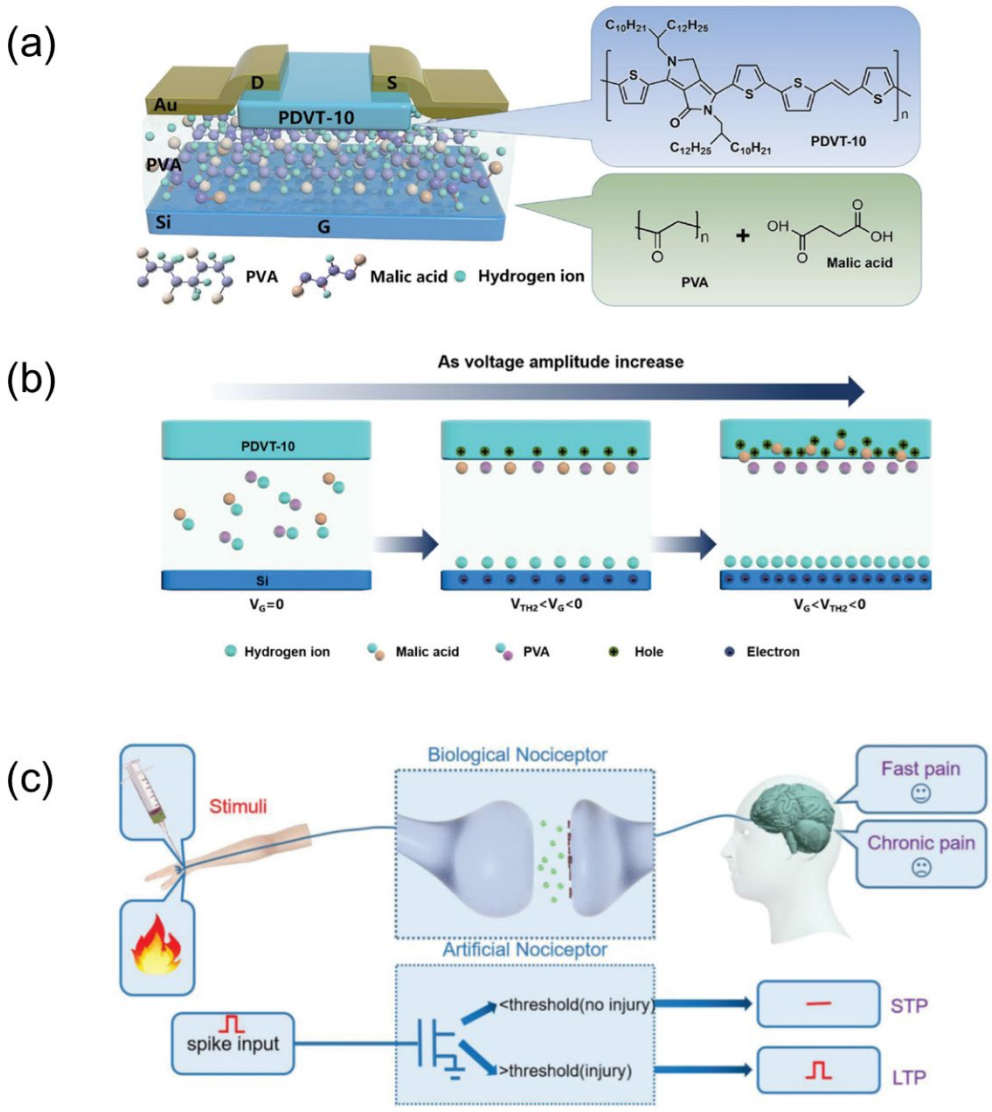

Figure 2-7. (a) Device structure and (b) work mechanism of the bi-mode electrolyte OMTs. (c) Schematic illustration of the biological nociceptor repsoned to stimuli with different strength.

2.3.4. Optical OMTs.

During the last decade, the controlled incorporation of functional molecules in semiconducting matrices has been demonstrated as a powerful approach to fabricate multifunctional devices. Such a strategy is particularly suitable when employing

photochromic molecules for the development of light-responsive and thus optically controllable and programmable electrical devices.

Hybrids comprising azobenzene,[34] spiropyran,[35] and diarylethene[36] have garnered great attention for application in data storage, imaging, and sensing. Among them, diarylethenes (DAEs) have particular advantages since they can undergo reversible isomerization between the open and the closed states when irradiated with ultraviolet (UV) and visible (Vis) light, respectively. While the two states are thermally stable at ambient conditions, they exhibit vastly different energy levels of their frontier molecular orbitals, *i.e.*, the LUMO and the HOMO.[37] Thus, DAEs are particularly adapt for optically modulating charge transfer in blends with organic semiconductors upon irradiation at distinct wavelengths. Optically switchable field-effect transistors (OSFETs) are non-volatile photonic memory devices holding a great potential for applications in optical information storage and telecommunications. Solution processing of blends of photochromic molecules and π-conjugated polymers is a low-cost protocol to integrate simultaneously optical switching and charge transport functions in large-area devices.[38] Leydecker *et al*. reported a multilevel non-volatile flexible OSFETs based on a solution blending thin film of poly(3-hexylthiophene) and diarylethene, as shown in Figure 2-8, which allow to define many distinct current levels by controlling irradiation time.[39]

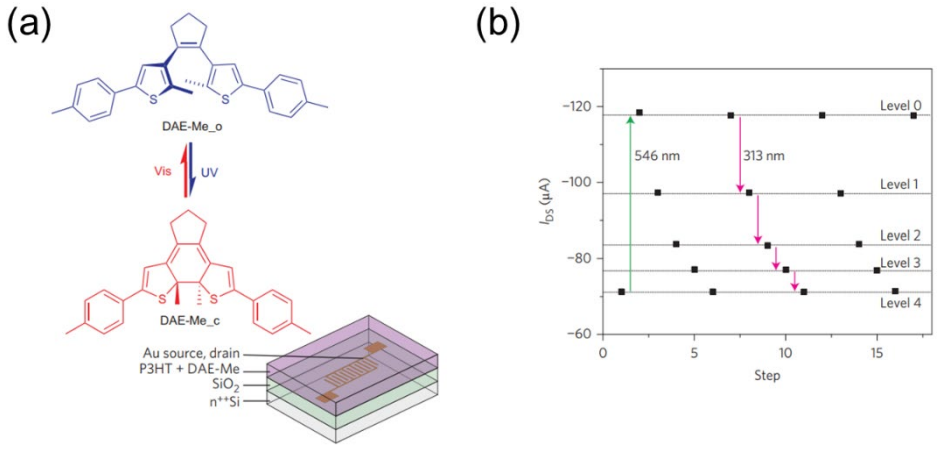

Figure 2-8. (a) Chemical structure of DAE molecules and P3HT. Device structure of optical switchable transistor, where P3HT and DAE were solution blending as active channel layer. (b) Multilevel photo-programed I_{DS} wrote by 313 nm and erased by 546 nm.[39]

Persistent photoconductivity (PPC) property is characterized by a photocurrent that can endure for hours or even days after light illumination and it represents a well-known phenomenon in metal oxide systems.[40] PPC materials-based optical inorganic memory transistors have been thoroughly studied in synaptic transistor. For example, Kim *et al.* manufactured synaptic transistors via exploiting indium gallium zinc oxide (IGZO) as PPC channel layer and zirconium-doped hafnium oxide ($HfZrO_x$) as ferroelectric layer. Oxygen vacancies of IGZO exhibited at shallow donor states (V_O^+ or V_O^{2+}) and deep localized states (V_O). Upon optical irradiation, electrons ionized from oxygen vacancies as the processes: single charged ($V_O \rightarrow V_O^+ + e^-$) or double charged (or $V_O \rightarrow V_O^{2+} + 2e^-$)), leading the enhancement of the conductance of IGZO, as illustrated in Figure 2-9a. Subsequently, charge slow recombination and slow neutralization can serve as synaptic function. Moreover, controllable relaxation properties of PSC can be achieved by applying different gate voltage bias (Figure 2-9b).[41]

Recently, PPC in OSC was also observed and provides an opportunity to achieve optical OMTs.[42,43] Jia *et al.* reveal the mechanism of organic PPC in optical OMT based on 2,8-difluoro-5,11-bis(triethylsilylethynyl) anthradithiophene (diF-TESADT) single crystal arrays. PPC property of diF-TESADT was operated for synaptic function research and characterized under different environmental conditions (Figure 2-9c). The devices under air and oxygen showed higher photocurrent and longer decay lifetime than that under vacuum and nitrogen, demonstrating that oxygen-induced deep levels in OSC trapping electron is essential for PPC behavior in OSC (Figure 2-9d).[44]

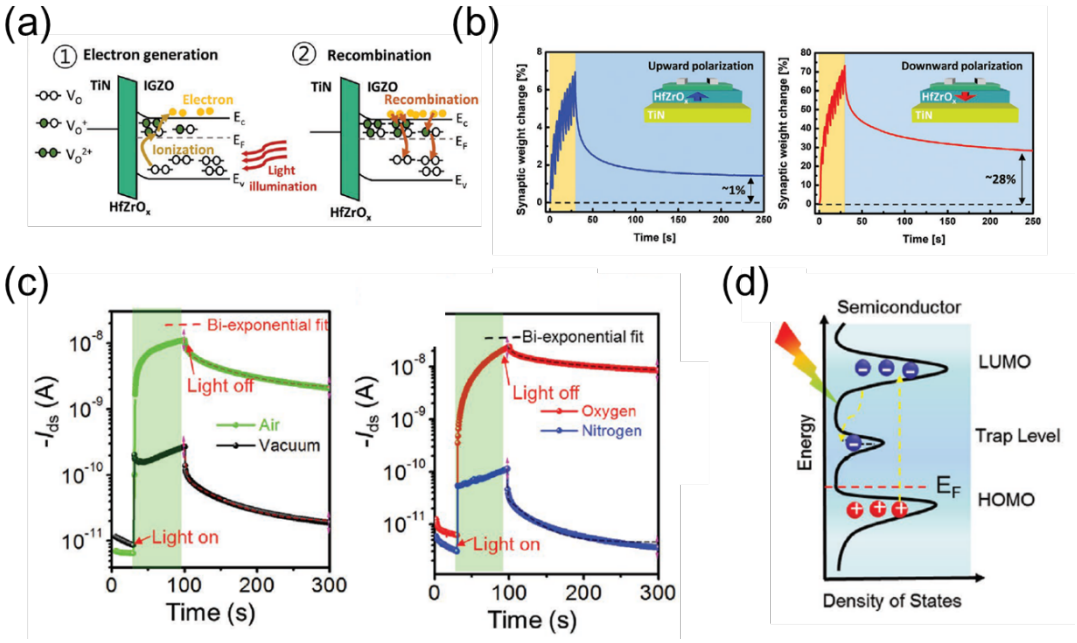

Figure 2-9. (a) Schematic mechanisms of PPC property in IGZO. (b) The long-term plasticity characteristics of IGZO-based synaptic transistors in upward and downward polarizations. (c) PSC decay curves of the diF-TESADT-based synaptic transistor measured under high vacuum, in air, in nitrogen and in oxygen, respectively. (d) Schematic mechanisms of PPC property in diF-TESADT which origin from oxygen trap energy level.

2.4. Reference

1. Zhu, Z.; Guo, Y.; Liu, Y., Application of Organic Field-effect Transistors in Memory. *Materials Chemistry Frontiers* **2020,** *4* (10), 2845-2862.

2. Han, S. T.; Zhou, Y.; Roy, V. A., Towards the Development of Flexible Non-volatile Memories. *Advanced Materials* **2013,** *25* (38), 5425-49.

3. Lu, K.; Li, X.; Sun, Q.; Pang, X.; Chen, J.; Minari, T.; Liu, X.; Song, Y., Solution-processed Electronics for Artificial Synapses. *Materials Horizons* **2021,** *8* (2), 447-470.

4. Dubnau, J.; Chiang, A. S.; Tully, T., Neural Substrates of Memory: from Synapse to System. *Journal of Neurobiology* **2003,** *54* (1), 238-253.

5. Pereda, A. E., Electrical Synapses and Their Functional Interactions with Chemical Synapses. *Nature Reviews Neuroscience* **2014,** *15* (4), 250-263.

6. Sangwan, V. K.; Hersam, M. C., Neuromorphic Nanoelectronic Materials. *Nature Nanotechnology* **2020,** *15* (7), 517-528.

7. Sebastian, A.; Le Gallo, M.; Khaddam-Aljameh, R.; Eleftheriou, E., Memory Devices and Applications for In-memory Computing. *Nature Nanotechnology* **2020,** *15* (7), 529-544.

8. Xia, Q.; Yang, J. J., Memristive Crossbar Arrays for Brain-Inspired Computing. *Nature Materials* **2019,** *18* (4), 309-323.

9. He, Y.; Jiang, S.; Chen, C.; Wan, C.; Shi, Y.; Wan, Q., Electrolyte-Gated Neuromorphic Transistors for Brain-like Dynamic Computing. *Journal of Applied Physics* **2021,** *130* (19), 190904.

10. Yang, F.-S.; Li, M.; Lee, M.-P.; Ho, I-Y.; Chen, J.-Y.; Ling, H.; Li, Y.; Chang, J.-K.; Yang, S.-H.; Chang, Y.-M.; Lee, K.-C.; Chou, Y.-C.; Ho, C.-H.; Li, W.; Lien, C.-H.; Lin, Y.-F., Oxidation-Boosted Charge Trapping in Ultra-Sensitive van der Waals Materials for Artificial Synaptic Features. *Nature Communications* **2021**, *11*, 2972.

11. Zhai, Y.; Yang, J.-Q.; Zhou, Y.; Mao, J.-Y.; Ren, Y.; Roy, V. A. L.; Han, S.-T., Toward Non-volatile Photonic Memory: Concept, Material and Design. *Materials Horizons* **2018,** *5* (4), 641-654.

12. Chou, Y.-H.; Chang, H.-C.; Liu, C.-L.; Chen, W.-C., Polymeric Charge Storage Electrets for Non-volatile Organic Field Effect Transistor Memory Devices. *Polymer Chemistry* **2015,** *6* (3), 341-352.

13. Kang, M.; Baeg, K.-J.; Khim, D.; Noh, Y.-Y.; Kim, D.-Y., Printed, Flexible, Organic Nano-Floating-Gate Memory: Effects of Metal Nanoparticles and Blocking Dielectrics on Memory Characteristics. *Advanced Functional Materials* **2013,** *23* (28), 3503-3512.

14. Liu, J.; Liu, C.-H.; She, X.-J.; Sun, Q.-J.; Gao, X.; Wang, S.-D., Organic Field-Effect Transistor Nonvolatile Memories Utilizing Sputtered C Nanoparticles as Nano-Floating-Gate. *Applied Physics Letters* **2014,** *105* (16), 163302.

15. Ren, Y.; Yang, J. Q.; Zhou, L.; Mao, J. Y.; Zhang, S. R.; Zhou, Y.; Han, S. T., Gate-Tunable Synaptic Plasticity through Controlled Polarity of Charge Trapping in Fullerene Composites. *Advanced Functional Materials* **2018,** *28* (50), 1805599.

16. Higashinakaya, M.; Nagase, T.; Abe, H.; Hattori R.; Tazuhara S.; Kobayashi T.; Naito, H., Electrically Programmable Multilevel Nonvolatile Memories Based on Solution-Processed Organic Floating-Gate Transistors. *Applied Physics Letters* **2021,** *118*, 103301.

17. Shih, C.-C.; Chiu, Y.-C.; Lee, W.-Y.; Chen, J.-Y.; Chen, W.-C., Conjugated Polymer Nanoparticles as Nano Floating Gate Electrets for High Performance Nonvolatile Organic Transistor Memory Devices. *Advanced Functional Materials* **2015,** *25* (10), 1511-1519.

18. Wang, R.; Chen, P.; Hao, D.; Zhang, J.; Shi, Q.; Liu, D.; Li, L.; Xiong, L.; Zhou, J.; Huang J., Artificial Synapses Based on Lead-Free Perovskite Floating-Gate Organic Field-Effect Transistors for Supervised and Unsupervised Learning. *ACS Applied Materials & Interfaces* **2021**, *13*, 43144-43154

19. Kim, J. Y.; Choi, M.-J.; Jang, H. W., Ferroelectric Field Effect Transistors: Progress and Perspective. *APL Materials* **2021,** *9* (2), 021102.

20. Hoffman, J.; Pan, X.; Reiner, J. W.; Walker, F. J.; Han, J. P.; Ahn, C. H.; Ma T. P., Ferroelectric Field Effect Transistors for Memory Applications. *Advanced Materials* **2010**, *22*, 2957-2961

21. Schroeder, R.; Majewski, L. A.; Grell, M., All-Organic Permanent Memory Transistor Using an Amorphous, Spin-Cast Ferroelectric-like Gate Insulator. *Advanced Materials* **2004,** *16* (7), 633-636.

22. Furukawa T., Ferroelectric Properties of Vinylidene Fluoride Copolymers. *Phase Transitions* **1989**, *18*, 143-211.

23. Zhu, H.; Fu, C.; Mitsuishi M., Organic Ferroelectric Field-effect Transistor Memories with Poly(vinylidene fluoride) Gate Insulators and Conjugated Semiconductor Channels: A Review. *Polymer International* **2021**, *70*, 404-413.

24. Naber, R. C. G.; Tanase, C.; Blom, P. W. M.; Gelinck, G. H.; Marsman, A. W.; Touwslager, F. J.; Setayesh, S.; de Leeuw, D. M., High-Performance Solution-processed Polymer Ferroelectric Field-effect Transistors. *Nature Materials* **2005,** *4* (3), 243-248.

25. Kang, S. J.; Bae, I.; Park, Y. J.; Park, T. H.; Sung, J.; Yoon, S. C.; Kim, K. H.; Choi, D. H.; Park, C., Non-volatile Ferroelectric Poly(vinylidene fluoride-co-trifluoroethylene) Memory Based on a Single-Crystalline Tri-isopropylsilylethynyl Pentacene Field-Effect Transistor. *Advanced Functional Materials* **2009,** *19* (10), 1609-1616.

26. Kim, M. K.; Lee, J. S., Ferroelectric Analog Synaptic Transistors. *Nano Letters* **2019,** *19* (3), 2044-2050.

27. Lu, Y.; Liu, K.; Yang, J.; Zhang, T.; Cheng, C.; Dang, B.; Xu, L.; Zhu, J.; Huang, Q.; Huang, R.; Yang, Y., Highly Uniform Two-terminal Artificial Synapses Based on Polycrystalline $Hf_{0.5}Zr_{0.5}O_2$ for Sparsified Back Propagation Networks. *Advanced Electronic Materials* **2020,** *6* (8), 2000204.

28. Chen, L.; Wang, L.; Peng, Y.; Feng, X.; Sarkar, S.; Li, S.; Li, B.; Liu, L.; Han, K.; Gong, X.; Chen, J.; Liu, Y.; Han, G.; Ang, K. W., A van der Waals Synaptic Transistor Based on Ferroelectric $Hf_{0.5}Zr_{0.5}O_2$ and 2D Tungsten Disulfide. *Advanced Electronic Materials* **2020,** *6* (6), 2000057.

29. Ko, C.; Lee, Y.; Chen, Y.; Suh, J.; Fu, D.; Suslu, A.; Lee, S.; Clarkson, J. D.; Choe, H. S.; Tongay, S.; Ramesh, R.; Wu, J., Ferroelectrically Gated Atomically Thin Transition-Metal Dichalcogenides as Nonvolatile Memory. *Advanced Materials* **2016,**

28 (15), 2923-2930.

30. He, Y.; Yang, Y.; Nie, S.; Liu, R.; Wan, Q., Electric-Double-layer Transistors for Synaptic Devices and Neuromorphic Systems. *Journal of Materials Chemistry C* **2018,** *6* (20), 5336-5352.

31. Huang, J.; Chen, J.; Yu, R.; Zhou, Y.; Yang, Q.; Li, E.; Chen, Q.; Chen, H.; Guo, T., Tuning the Synaptic Behaviors of Biocompatible Synaptic Transistor through Ion-Doping. *Organic Electronics* **2021,** *89,* 106019.

32. Chen, J.; Huang, W.; Zheng, D.; Xie, Z.; Zhuang, X.; Zhao, D.; Chen, Y.; Su, N.; Chen, H.; Pankow, R. M.; Gao, Z.; Yu, J.; Guo, X.; Cheng, Y.; Strzalka, J.; Yu, X.; Marks, T. J.; Facchetti, A., Highly Stretchable Organic Electrochemical Transistors with Strain-Resistant Performance. *Nature Materials* **2022,** *21* (5), 564-571.

33. Yu, R.; Yan, Y.; Li, E.; Wu, X.; Zhang, X.; Chen, J.; Hu, Y.; Chen, H.; Guo, T., Bi-Mode Electrolyte-Gated Synaptic Transistor Via Additional Ion Doping and Its Application to Artificial Nociceptors. *Materials Horizons* **2021,** *8* (10), 2797-2807.

34. Bartholomew, A. K.; Stone, I. B.; Steigerwald, M. L.; Lambert, T. H.; Roy, X., Highly Twisted Azobenzene Ligand Causes Crystals to Continuously Roll in Sunlight. *Journal of the American Chemical Society* **2022,** *144* (37), 16773-16777.

35. Liu, C. F.; Lin, H.; Li, S. S.; Xie, H.; Zhang, J. L.; Ji, D. Z.; Yan, Y.; Liu, X.; Lai, W. Y., Smart Responsive Photoelectric Organic Modulator Integrated with Versatile Optoelectronic Characteristics. *Advanced Functional Materials* **2022,** *32* (17), 2111276.

36. Zhang, Z.; Wang, W.; Jin, P.; Xue, J.; Sun, L.; Huang, J.; Zhang, J.; Tian, H., A Building-Block Design for Enhanced Visible-Light Switching of Diarylethenes. *Nature Communications* **2019,** *10* (1), 4232.

37. Herder, M.; Schmidt, B. M.; Grubert, L.; Patzel, M.; Schwarz, J.; Hecht, S., Improving the Fatigue Resistance of Diarylethene Switches. *Journal of the American Chemical Society* **2015,** *137* (7), 2738-2747.

38. Hou, L.; Leydecker, T.; Zhang, X.; Rekab, W.; Herder, M.; Cendra, C.; Hecht, S.; McCulloch, I.; Salleo, A.; Orgiu, E.; Samorì, P., Engineering Optically Switchable Transistors with Improved Performance by Controlling Interactions of Diarylethenes in Polymer Matrices. *Journal of the American Chemical Society* **2020,** *142* (25), 11050-11059.

39. Leydecker, T.; Herder, M.; Pavlica, E.; Bratina, G.; Hecht, S.; Orgiu, E.; Samorì, P., Flexible Non-volatile Optical Memory Thin-Film Transistor Device with over 256 Distinct Levels Based on An Organic Bicomponent Blend. *Nature Nanotechnology* **2016,** *11* (9), 769-775.

40. Lee, M.; Lee, W.; Choi, S.; Jo, J. W.; Kim, J.; Park, S. K.; Kim, Y. H., Brain-Inspired Photonic Neuromorphic Devices using Photodynamic Amorphous Oxide Semiconductors and their Persistent Photoconductivity. *Advanced Materials* **2017,** *29* (28), 1700951.

41. Kim, M. K.; Lee, J. S., Synergistic Improvement of Long-Term Plasticity in Photonic Synapses Using Ferroelectric Polarization in Hafnia-Based Oxide-Semiconductor Transistors. *Advanced Materials* **2020,** *32* (12), 1907826.

42. Yuan, Y.; Huang, J., Ultrahigh Gain, Low Noise, Ultraviolet Photodetectors with Highly Aligned Organic Crystals. *Advanced Optical Materials* **2016,** *4* (2), 264-270.

43. Zhang, J.; Liu, D.; Ou, Q.; Lu, Y.; Huang, J., Covalent Coupling of Porphyrins with Monolayer Graphene for Low-Voltage Synaptic Transistors. *ACS Applied Materials & Interfaces* **2022,** *14* (9), 11699-11707.

44. Jia, R.; Wu, X.; Deng, W.; Zhang, X.; Huang, L.; Niu, K.; Chi, L.; Jie, J., Unraveling the Mechanism of the Persistent Photoconductivity in Organic Phototransistors. *Advanced Functional Materials* **2019,** *29* (45), 1905657.

Chapter 3. Organic Light-Emitting Transistors

3.1. Background of OLETs

Organic light-emitting devices are key components for emerging opto- and nanoelectronics applications including health monitoring and smart displays. The working principle of organic light-emitting devices relies on the electroluminescence of organic molecules, which present unique advantages, such as high image quality, fast response times, and wide viewing angle.[1] During the last two decades, a notable research effort has been devoted to the development of high-performance organic light-emitting materials and devices to address the technological needs in the rapidly expanding flexible electronics consumer market. In 2021, the global organic light-emitting diode (OLED)-based display market was valued at 38.4 billion dollars, with a projected increase to 72.8 billion dollars by 2026.

The optimized device architecture of OLEDs comprises nine vertically stacked layers, as displayed in Figure 3-1a, wherein oppositely charged carriers (hole and electron) can migrate and be recombined under applied electrical voltage, yielding conversion of electrical energy into light emission. OLEDs require asymmetric electrodes, named anode and cathode, being characterized by a high and a low work function, respectively. To enable efficient light extraction, one of electrodes needs to be transparent such as indium tin oxide (ITO), thin Au, and graphene, while the other one is a reflective metal such as Al and Ag. Device engineering including embedding index-matched macroscopic lens, modifications of the layer stack with respect to thicknesses, utilizing of microcavity structures have been demonstrated as successful method to further improve device performance by enhancement of light outcoupling.[2] Charge transport layers and charge injection layers are employed to decrease the energy barrier between the electrodes and the light-emitting materials, thus pushing the hole and electron to higher energy levels under electrical filed. Some high-performance OLEDs also incorporate a charge-blocking layer to limit charge recombination zoom at the

emissive layer for improving the lifetime of devices. As a result, electrons/holes are injected into the LUMO/HOMO of light-emitting molecules forming the singlet and triplet excitons and subsequently emitting photons by radiative decay. The energy levels alignment of OLEDs is presented in Figure 3-1b.

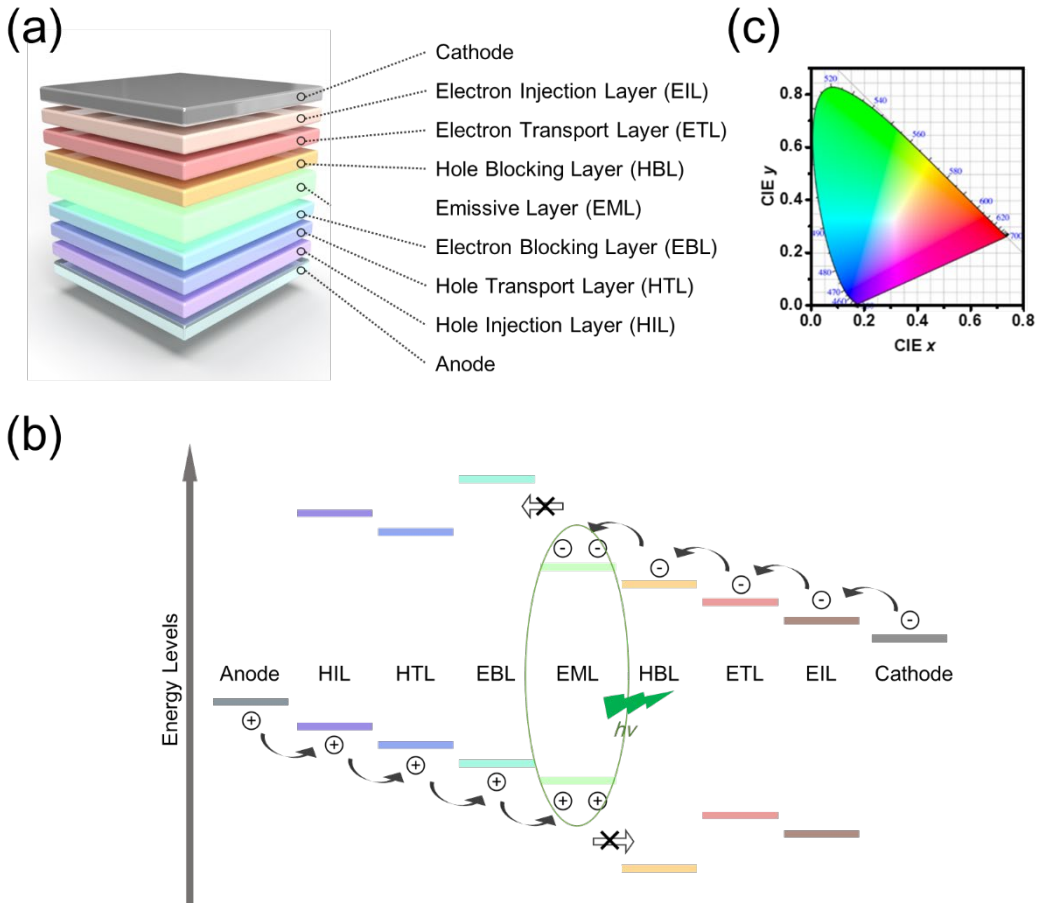

Figure 3-1. (a) Device architecture and (b) energy diagram of a typical OLEDs. (c) CIE1931 color space.

Compared with active-matrix OLEDs (AMOLED) which comprises one diode and one transistor, OLETs have been considered as core elements for the next-generation of active-matrix (AM) displays, as they integrate both the current-switching and the light emission functions into a single device. First OLETs device were reported in 2003.[3] Since then, significant progress in the understanding of the physics and chemistry of

OLETs have been achieved, as well as the development of new materials and device architectures. OLETs present huge potential to revolutionize the field of organic electronics and to facilitate the development of new types of multifunctional electronic devices.

Key parameters of OLETs include:

i) Radiant energy: The radiant energy of organic light-emitting devices is the energy of emitted light from the light-emitting molecules, which is expressed in Joule (J). On the other hand, the radiant flux (Watt, W) of light is defined as the radiant energy emitted per unit time.

ii) Brightness: Differently to the energy units, the brightness of light-emitting devices refers to its luminous intensity, which depends on the sensitivity of the human eye to different wavelengths of visible light, with its unit being Candela (cd) or nits (cd m^{-2}). Notably, green light is more sensitivity for human eyes compared with blue and red light.

iii) External quantum efficiency (EQE): EQE quantifies the percentage of the photons emitted in light-emitting devices versus the electron injected into the device. EQE stands for how effectively a light-emitting device converts electrical energy into light energy. A higher EQE indicates that more of the electrical energy can be converted into light energy, which can result in a brighter display.

iv) Turn-on voltage: The turn-on voltage of OLETs is the minimum voltage required for light emission, which is related to V_{Th} of devices. Lower turn-on voltages are desirable to achieve lower power consumption and higher efficiency of devices.

v) Light emission spectrum and CIE coordinates: The spectrum of the emitted light is relevant to the color of light. The purify of light can be evaluated by full width at half maximum (FWHM) of emitted peak. In 1931, the Commission Internationale de L'éclairage (CIE) defined all the visual color by CIE1931 Color Space (Figure 3-1c),

which are presented by X，Y，Z value. Because the sum of X, Y and Z is 1 (X + Y + Z = 1), the coordinates of (X, Y) is usually used to defined color of light.

3.2. Light-Emitting Molecules

According to the spin statistics, the relative probability for the formation of singlet and triplet excitons in electrical light emitting devices amounts to 25% and 75%, respectively, (Figure 3-2a). The excitons of light-emitting molecules existing at singlet excited state (S_1) and triplet excited state (T_1) can decay to ground state (S_0) for photonic emission. The process of exciton transferring from singlet to triplet is intersystem crossing (ISC). On the contrary, reverse process is reverse intersystem crossing (RISC). Light-emitting molecules are desired to harvest both singlet and triplet excitons for more generation of photons. According to different radiative decay processes, the light-emitting molecules are divided into fluorescence molecules, phosphorescence molecules and TADF molecules (Figure 3-2b).[4]

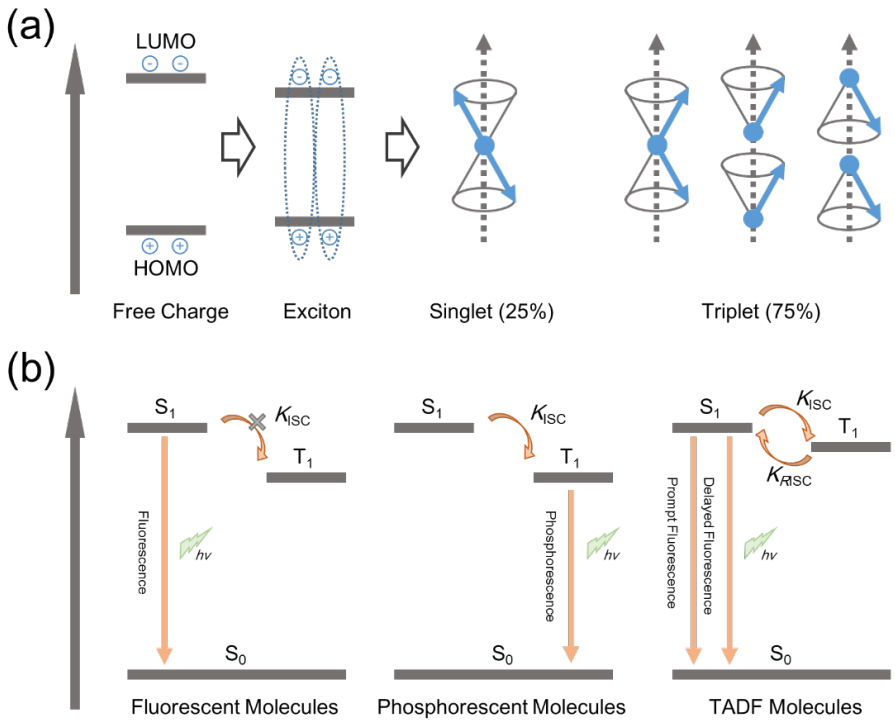

Figure 3-2. (a) Scheme of formation of singlet and triplet excitons in electrical light emitting devices. (b) *Jablonski* diagram for illustration the excitons decay process of

fluorescence molecules, phosphorescence molecules and TADF molecules.

3.2.1. Fluorescence Molecules

The first generation of light-emitting molecules comprises fluorescent molecules, which have a relatively large energetic gap between the S_1 and T_1 state, yielding quantum-mechanically forbidden energy transformation between S_1 and T_1. In other words, ISC and RISC is very weak. More importantly, any transitions between T_1 and the singlet ground state S_0 is forbidden, leading the energy dissipaton of triplet excitons.

In 1987, Tang *et al.* published a pioneering study on electroluminescence from organic molecules of tris(8-hydroxy-quinoline)aluminium (Alq_3). OLEDs were fabricated as simple 4 layers' architecture: ITO/aromatic diamine/Alq_3/alloyed Mg:Ag. Hole and electron can inject under the applied voltage lower than 10 V and thus recombine in Alq_3 layer, yielding unique devices performance with EQE of 1 %, luminous efficacy of 1.5 lm/W, and brightness over 1000 cd m^{-2}.[5] Thanks to the better mechanical property of fluorescent polymer, in 1992, Gustafsson *et al.* fabricated a fully flexible LED (Figure 3-3a) by using poly(ethylene terephthalate) (PET) as the substrate and ethylhexoxy-substituted poly(2-methoxy, 5-(2'-ethyl-hexoxy)-1,4-phenylenevinylene) (MEH-PPV) as the electroluminescent layer.[6] More recently, by employing polyurethane (PU) as the soft elastic matrix for blending light-emitting polymer, Zhang *et al.* demonstrated a fabrication of stretchable OLEDs (Figure 3-3b), which possess excellent brightness even when subjected to around 100% strain.[7]

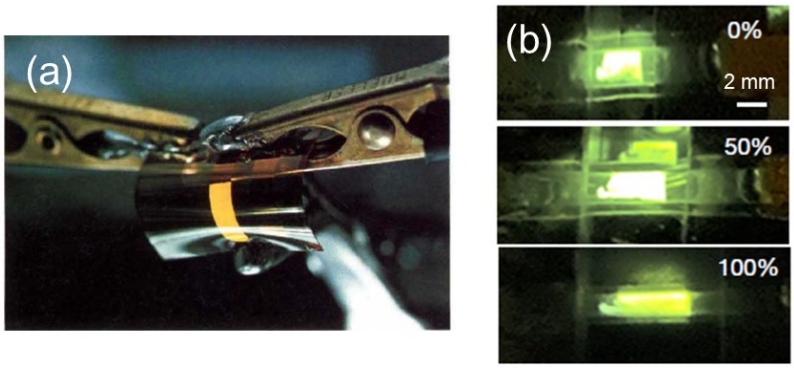

Figure 3-3. Photographs of (a) flexible OLEDs at 6 V appiled bias voltage and (b) stretchable OLEDs at 9 V appiled bias voltage.

3.2.2. Phosphorescence Molecules

Phosphorescent materials, which can be considered being the most employed second-generation organic light-emitting molecules, are significantly more efficient than standard fluorescent materials. Radiative transition from the T_1 to the S_0 is allowed in organometallic complexes when heavy metal (Ir, Pt, Eu, and Os) elements are introduced, due to a phenomenon of spin-orbit coupling. In these complexes, the heavy metal atom is surrounded by organic ligands, and the interaction between the electrons of the metal atom and the ligands leads to a coupling between the spin and orbital angular momentum of the electrons, known as the spin-orbit coupling. This coupling results in the mixing of the singlet and triplet excited states, allowing the radiative transition from T_1 to S_0 and thus yielding emission of a photon. The probability of this transition is usually low because it involves a change in the spin of the electron. However, the heavy metal atoms in organometallic complexes have high atomic numbers, resulting in strong spin-orbit coupling and a higher probability of radiative decay from T_1 to S_0.[4]

One well-known phosphorescent molecule is tris(2-phenylpyridine) iridium ($Ir(ppy)_3$). OLEDs can be fabricated based on emitter of $Ir(ppy)_3$ doped into a 4,4′-N,N′-

dicarbazole-biphenyl (CBP) as host, which present a high EQE of 8.0% and maximum luminance of 10^6 cd m^{-2}.[8] Nevertheless, phosphorescence molecules of organometallic complexes based on expensive element are characterized by a high cost due to their ultra-low abundance on the earth. Organometallic complexes based on earth-abundant metal ions (Cu, Zr, Fe, Cr) hold huge potential for eco-friendly applications in light-emitting devices.[9] For example, Ma *et al.* report and synthesized organometallic complexes, tetranuclear complex $Cu_4(CCph)_4L_2$ (L = 1,8-bis(diphenylphosphino)-3,6-dioxaoctane). Phosphorescence OLEDs with structure of ITO/$Cu_4(CCph)_4L_2$:Poly(9-vinylcarbazole) (PVK)/triazole derivative/Al exhibited brightness of 50 cd m^{-2} at current density 20 mA cm^{-2}.[10]

3.2.3. TADF Molecules

TADF is a phenomenon that can be found in TADF molecules, which exhibit a low energy difference between their singlet and triplet excited states (ΔE_{ST}), typically on the order of several hundred milli-electron volts (meV). Such small ΔE_{ST} can lead to small spatial overlap between the HOMO and LUMO, which created by strong donor and acceptor functional groups of TADF emitter. Although direct transitions between the first excited triplet state (T_1) and the ground state singlet (S_0) are still forbidden, it is possible for the excitons to return from T_1 to the S_1 via RISC if the thermal energy (kbT) is sufficient for activation. This phenomenon results in an excited state lifetime that is longer than typical fluorescence, often in the order of microseconds (μs) or more. Such mechanism of TADF allows the molecules harvesting of all excitons, which can theoretically yield 100% internal quantum efficiency (IQE).[11]

Three archetypical TADF emitters with different color are introduced here.

(1) Wu *et al.* report the designed and synthesized (D-A-D) type and rodlike TADF emitter, 9,10-bis(4-(9H-carbazol-9-yl)-2,6-dimethylphenyl)-9,10-diboraanthracene (CzDBA), which show excellent photoluminescence quantum yield of ~100% and an 84% horizontal dipole ratio in the thin film. Based on this molecule, OLEDs were

fabricated as the configuration of ITO/N,N′-Bis(naphthalen-1-yl)-N,N′-bis(phenyl)benzidine (NPB)/TCTA/CBP: 10% wt% CzDBA/1,3,5-Tri(m-pyridin-3-ylphenyl)benzene (TmPyPB)/LiF/Al, which has realized a high EQE of 37.8 %, low efficiency roll-off (only 0.3% roll-off of the EQE at 10^3 cd m^{-2}), and electroluminescence peak at 528 nm corresponding to CIE of (0.31, 0.61), making it attractive for full-color-display applications.[12]

(2) Zeng *et al.* designed and synthesized orange-red emitters NAI-DPAC based on the coupling of rigid 9,9-diphenyl-9,10-dihydroacridine donor and 1,8-naphthalimide acceptor. Density functional theory (DFT) calculations were performed to predict ΔE_{ST} of NAD-DPAC as 0.26 eV, allowing effective RISC process. Orange-red OLEDs with typical structures of ITO/MoO_3/1,1-bis[(di-4-tolylamino)phenyl]cyclohexane (TAPC)/N,N-dicarbazolyl-3,5-benzene (mCP)/9-(3-(9H-carbazol-9-yl)phenyl)-9H-carbazole-3-carbonitrile (mCPCN): 6 wt% NAI-DPAC/tris-[3-(3-pyridyl)mesityl]borane (3TPYMB)/LiF/Al were fabricated, which exhibited superior external quantum efficiencies of 29.2%.[13]

(3) Lin *et al.* designed and synthesized blue highly efficient TADF emitter, spiroacridine-triazine (SpiroAC-TRZ), simultaneously exhibiting high photoluminescence quantum yield (PLQY) of 100%, excellent thermal stability, and strongly horizontally oriented emitting dipoles based on the hybrid. Deep blue OLEDs with architecture of ITO/MoO_3/TAPC/mCP/mCPCN: 12 wt% SpiroAC-TRZ/3TPYMB/LiF/Al, display extremely efficient EL with IQE of nearly 100% and EQE of nearly 37% without incorporation of any optical outcoupling schemes.[14]

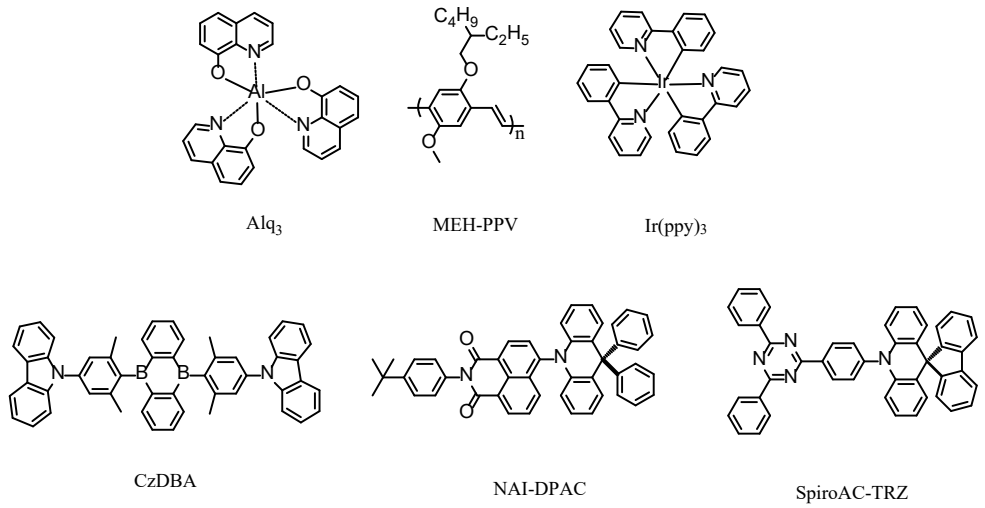

Figure 3-4. Chemical structures of light emitter mentioned in this part.

3.3. Device Architecture of OLETs

The device structure of OLETs can comprise a single layer, multilayers or hybrid structures with the aim of achieving high performance. Vertical OLETs are also attractive because of their conceptually simple fabrication process consisting in depositing a vertical transistor on a light-emitting diode, wherein the gate electrode, gate dielectric, porous source electrode, channel, and drain electrode are stacked vertically.[15]

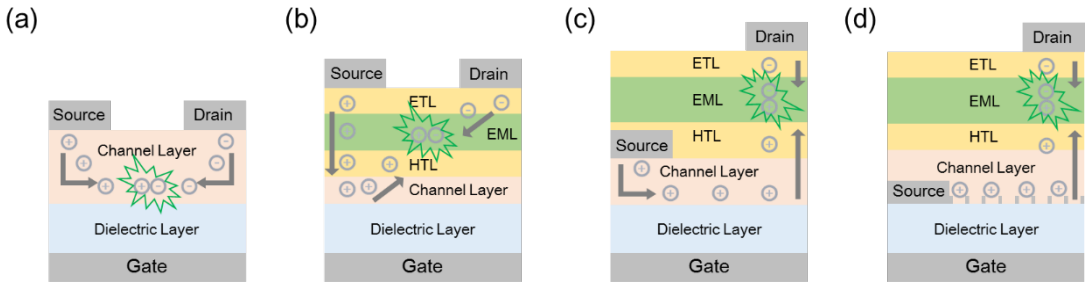

Figure 3-5. General device structures of P-type a) single-layer OLETs; b) multilayer OLETs; c) hybrid OLETs; d) vertical OLETs. Note, the pathway of hole/electron injection and transporting can be reversed in N-type devices.

3.3.1. Single Layer OLETs

As shown in Figure 3-5a, single layer OLETs can be fabricated by direct deposition on the dielectric layer of OSC, which should combine high carrier mobility and efficient solid-state emission. For example, as π-conjugated polymer, poly(9,9-din-octylfluorene-alt-benzothiadiazole) (F8T2) can be simply spin-coated from a p-xylene solution for the fabrication of single layer OLETs, leading the gate controllable light emission.[16] Natali *et al.* intoduced a high-capacitance photonic crystal as a gate dielectc layer to enhance the performance of single OLETs based on active layer of 2,3-thienoimide ended quaterthiophene derivative 2,2′-(2,2′-bithiophene-5,5′-diyl) bis(5-butyl-5H-thieno[2,3-c] pyrrole-4,6)-dione (NT4N). Multilayer photonic crystal of nine alternating high-density layers of ZrO_2 and Al_2O_3 were deposited by pulsed laser deposition (PLD) technique, presenting two advantages, *i.e.* a significantly incresed transistor source-drain current and an enhanced emitted light outcoupling. The device structure and optical image of NT4N-based single layer OLETs is presented in Figure 3-6a.[17]

Li *et al.* fabricated single layer OLETs based on single crystal of 2,6-di(2-naphthyl)anthracene (dNaAnt), which combined outstanding balanced ambipolar field-effect mobility (μ_h = 1.10 $cm^2\ V^{-1}\ s^{-1}$, μ_e = 0.87 $cm^2\ V^{-1}\ s^{-1}$) with efficient PLQY of 29.2%). The introduction of a naphthyl group into the 2,6-sites of the anthracene revealed the molecular designing strategy with the following features: (i) prolonged conjugation length and compact packing; (ii) promoted molecular J-aggregated; (iii) optimized of the energy levels with the electrodes.[18]

Moreover, Liu *et al.* reported the synthesis of organic laser molecule, 2,7- diphenyl-9H-fluorene (LD-1) integrating excellent mobility of 0.25 $cm^2\ V^{-1}\ s^{-1}$, high PLQY of 60.3%. Single layer OLETs based on LD-1 exhibited the versatile optoelectronic properties with superior deep-blue laser characteristics, which display low threshold pump density of 71 μJ cm^{-2} and 53 μJ cm^{-2} combining with high quality factor of

~3100 and ~2700 at emission peaks of 390 and 410 nm, respectively.[19]

A series of color-tunable and high-mobility single layer OLETs have been demonstrated by Qin *et al.*, via molecular doping of emitter into a high-mobility OSC, 2,6-diphenylanthracene, as the host. Tetracene (Tc) and pentacene (Pen) were employed as emitter molecules due to the well-matched molecular structures and sizes combination with efficient host-guest energy transfer, which enable the intrinsically high charge transport with tunable colors. The CIE coordinates of single layer OLETs based on DPA, Tc 8%-doped DPA, Pen 3% doped DPA, Tc 3% doped DPA, and Pen 0.5% doped DPA are (0.1617, 0.1101), (0.2750, 0.5361), (0.6535, 0.3223), (0.2819, 0.4401), and (0.5135, 0.2530), respectively. Optical images of DPA, Tc 8%-doped DPA and Pen 3% doped DPA- based OLETs are displayed in Figure 3-6b. The fabricated strategy of colorful high-mobility single layer OLET based on guest-doped single crystal is essential for achieving monolithic colorful and white lasers, as well as integrated optoelectronic applications in the future.[20]

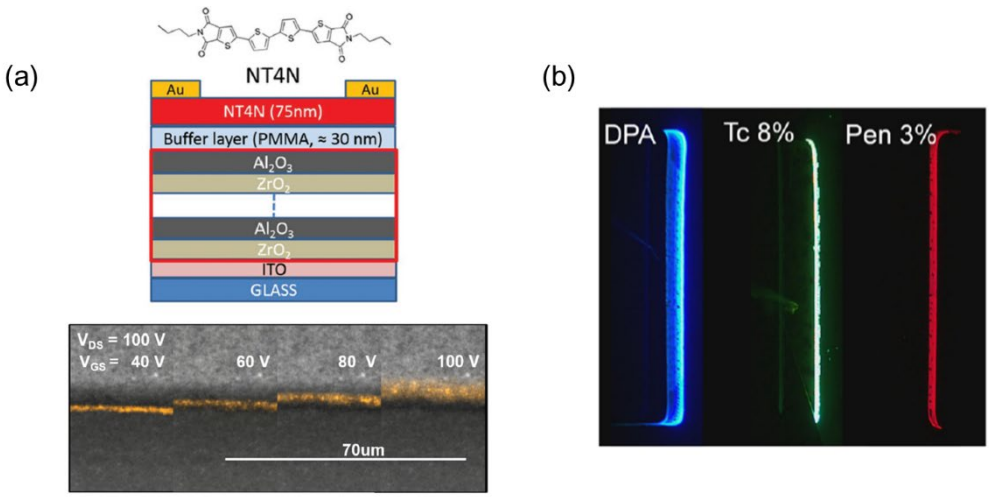

Figure 3-6. (a) Device structure schema and optical images of the NT4N-based single layer device. Light emission located within the channel layer which can be modulated by applied gate voltage.[17] (b) Optical image of full color single crystal OLETs based on DPA.[20]

3.3.2. Multilayer OLETs

π-conjugated molecules exhibit strong emission in dilute solutions or single molecule state, which is partially or even completely quenched in the solid state.[21] This aggregation-caused quenching (ACQ) phenomenon is mainly ascribed to the intense intermolecular π-π stacking interactions, inhibiting simultaneously high mobility and high PLQY of OSC. To overcome this limitation in efficiency in single layer OLETs, Muccini *et al.* developed ambipolar trilayer OLETs in 2010, wherein the p-channel layer, emission layer and n-channel layer were deposited sequentially (Figure 3-5b). By combining an ordered OSC material as channel layer and a high PLQY OSC in the emissive layer, the light emitting efficiency and EQE of the fabricated devices were over 10 times higher than that of single layer OLETs.[22] After this propaedeutic work, OLETs devices containing more functionalized layers (four layers or even five layers) have been fabricated and studied.

Yuan *et al.* synthesized and compared a series of semiladder polymers based on the building block of weak acceptor monomer 4,10-bis(2-butyloctyl)thieno[2′,3′:5,6]pyrido[3,4-g]thieno[3,2-c]-isoquinoline-5,11-dione or 5,11-bis(2-butyloctyl)-thieno[2′,3′:4,5]pyrido[2,3-g]thieno[3,2-c]quinoline-4,10-dione (TPTQ) and weak donor monomer carbazole or fluorene (F). They found that light-emitting copolymer TPTQ-F exhibited superior PLQY of 77% and balanced ambipolar field-effect mobilities of $\mu_h = 1.26 \times 10^{-3}$ cm^2 V^{-1} s^{-1} and $\mu_e = 3.53 \times 10^{-4}$ cm^2 V^{-1} s^{-1}. Multilayered OLETs fabricated by solution-processed embedded TPTQ-F into p-channel and n-channel displayed an excellent performance with an EQE of 5.3% and an electroluminescent intensity of 414 nW.[23]

To further balance carrier injection between the holes and electrons, Hu *et al.* investigated the role of the hole blocking layer (HBL) in multilayer OLETs. Their results indicated that, a deeper HOMO level of the HBL for facilitating exciton recombination efficiency is more important than a higher electron mobility of materials.

By adopting pentacence as channel layer, NPB as hole transport layer, CBP: 6 wt% $Ir(ppy)_3$ as emission layer, and bis[(4-tert-butylphenyl)-1,3,4-oxadiazolyl]phenylene (OXD-7) as the HBL, green multilayer OLETs with an EQE of 10.3% and a maximum brightness of around 8000 cd m^{-2} were achieved.[24] Similar conclusions were also demonstrated by Moschetto *et al.* They carried out an in-depth study on the interface layer in the multilayer OLETs via exploring various electron transport OSCs with different properties. Compared with ditridecylperylene-3,4,9,10-tetracarboxylic diimide (P13) which present misalignment energy level at the emission layer/P13 interface, multilayer OLETs based on (2,5-bis(4-(perfluorooctyl)phenyl)thieno-[3,2-b]thiophene (N-F2-6), and α,ω-diperfluorohexyl-quaterthiophene (DFH-4T) exhibited a good energy level alignment, yielding a higher EQE and maximum brightness.[25]

3.3.3. Hybrid OLETs

Light emission in light-emitting devices relies on the hole/electron recombination zoom. Carriers of hole/electron horizontally recombining in single layer OLETs and multilayer OLETs lead to a narrow emission zone on the edge of the drain electrode and moving in the middle of the channel, respectively, providing poor aperture ratio and restricted application of devices. Muhieddine *et al.* firstly demonstrated the area of light emission in OLETs based on a hybrid architecture in 2015 (Figure 3-5c). Upon using super yellow (SY) as light emission layer, hybrid OLETs displayed a special feature of the area light emission under drain electrode, that can be designed as circular shape for pixel display (Figure 3-7a).[26] Compared with multilayer structure, the source electrode was deposited before the charge transport layer and light emission layer, yielding a lower charge injection barrier between the source electrode and channel layer. More importantly, Gao *et al.* revealed the role of charge-transport buffer (CTB) layer deposited over channel layer, which can restrict the current density in the conventional lateral channel. As a result, vertically hole/electron recombination occurred under drain electrode, yielding the sufficiency area emission.[27] Expanding the area of drain electrode, hybrid OLETs with high aperture ratio of 80% was demonstrated.

Sobus *et al.* fabricated both P-type and N-type hybrid OLETs based on the TADF light emission layer comprised by (2,4,5,6-tetra[9H-carbazol-9-yl]isophthalonitrile) (4CzIPN) material as a guest in a host of CBP. Zinc-tin oxide (ZTO) and 2,7-dioctyl[1]benzothieno[3,2-b][1]benzothiophene (C8-BTBT-C8) were employed as the N-type and P-type channel layer because their advantages of ease of processing, robustness, and high filed-effect mobility. To improve light efficiency and EQE of hybrid OLETs, top contact electrode (drain electrode) based on ultra-thin metal with high conductivity included Au and Ag have been demonstrated to achieve light out-coupling because their high transparent on visible light range. As a result, these devices manifested a superior opto-electrical performance, being comparable to the equivalent OLEDs based on the same active materials.[28]

To reduce operation voltage of hybrid OLETs, Zhao *et al.* utilized high *k* materials of ZrO_x/cross-linked poly(vinyl alcohol) (C-PVA) bilayer as gate dielectric. An efficient organic phosphorescent molecule bis[2-(3,5-dimethylphenyl)-5-isobutylquinoline-C2,N′](acetylacetonato)iridium(III) was doped into bi-host system as an light emission layer. Capacitance of ZrO_x/C-PVA bilayer were emulated by 46.7 nF cm^{-2}, combining an ideal breakdown voltage of 36 V. As a result, hybrid OLETs exhibited an exceptional performance metrics, including a standard red color EL (CIE (0.66, 0.33)), a remarkably high maximum brightness of 20,030 cd m^{-2} under both low gate and drain voltage of −24 V.[29]

The development of flexible organic electronics offers the potential for creating wearable and intelligent products. Chen *et al.* firstly reported the fabrication flexible hybrid OLETs on transparent and flexible substrate of ITO/PET. Based on the dielectric layer comprised C-PVA and perfluoro(1-butenyl vinyl ether) polymer (CYTOP), the devices displayed a brightness of 8300 cd m^{-2} when gate voltage of −18 V and drain voltage of −24 V were applied. Moreover, light emission could be observed even tapped devices on the glass bottle with 10 mm diameter, as shown in Figure 3-7b.[30]

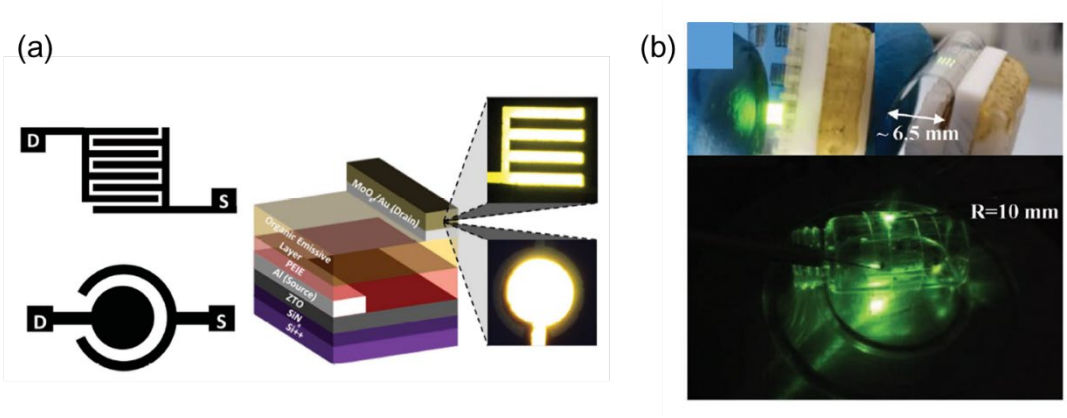

Figure 3-7. (a) Device structure and optical images of SY-based hybrid OLETs with interdigitated and pixel-like drain/source electrode.[26] (b) Photo images of flexible hybrid OLETs.[30]

3.3.4. Vertical OLETs

Vertical OLETs represent another novel kind of "area-emitting" OLETs , as shown in Figure 3-5d. From the device physics perspective, the short channel of OSC inserted in-between vertically stacked electrodes possesses three unique features: (i) a large decrease in the channel length down to the ~10 nm range, which is determined by the thickness of OSC layer, (ii) a higher current density at a lower operating voltage, (iii) a more efficient exciton separation yielding higher performance in practical applications based on light–matter interactions. As a result, the devices feature strong emitting light at low operation voltages due to the extremely short channel lengths on the nanometer scale. Several types of porous source electrodes have been reported for fabrication of OLETs, such as ultra-thin metal, graphene, carbon nanotube, and nano-pattern metal. Compared to the narrow emission zone typical of lateral OLETs, the vertically-stacked configuration ensures higher space utilization and aperture ratios.

Nanostructured conductors, which include carbon nanotubes and metal nanowires were utilized as porous source electrodes in vertical OLETs. McCarthy *et al.* have reported red, green, and blue vertical OLETs using single-wall carbon nanotubes as

source electrodes.[31] The carbon nanotubes transferred on the sample can form not only a dilute network with superior electrical percolation, but they can also exhibit a light transmittance exceeding 98% across the whole visible spectrum. The device structure of OLETs is displayed in Figure 3-8. By applying suitable V_D for each vertical OLETs (−6.8 V for red, −4.9 V for green and −5.7 V for blue), the devices were operated at a gate voltage V_G ranging from −3 V to +3 V. All these devices exhibited a maximum luminance around 500 cd m^{-2} and on/off ratios reaching 10^4. Similarly to single-wall carbon nanotubes, spin-coated Ag nanowires have been also employed as source electrodes to fabricate vertical OLETs.[32, 33]

Since a fine control of the source electrode porosity is essential for a homogeneous potential distribution within the channel layer at equilibrium, Yu *et al.* exploited the self-assembly of polystyrene (PS) nano-spheres to produce a close-packed nanopore array serving as a shadow mask for evaporating the ITO film. By controlling the particle size of PS nano-spheres by reactive ion etching, the pore size in the ITO film can be tuned from 40 to 150 nm. Based on the optimized vertical OTFT structure, the authors fabricated vertical OLETs with the structure illustrated in Figure 3-8. Transfer characteristics were collected at a constant V_D of 13 V. Without gate biasing, the electron injection at the ITO source electrode is negligible, resulting in poor luminance although holes are efficiently injected from the Al drain electrode. At a positive gate bias, the decreased Schottky barrier reflects the increased injection of electrons which then recombine with holes delivering a device luminance of 170 cd m^{-2} and a high luminance on/off ratio of 10^4 at V_G = 6 V.[34]

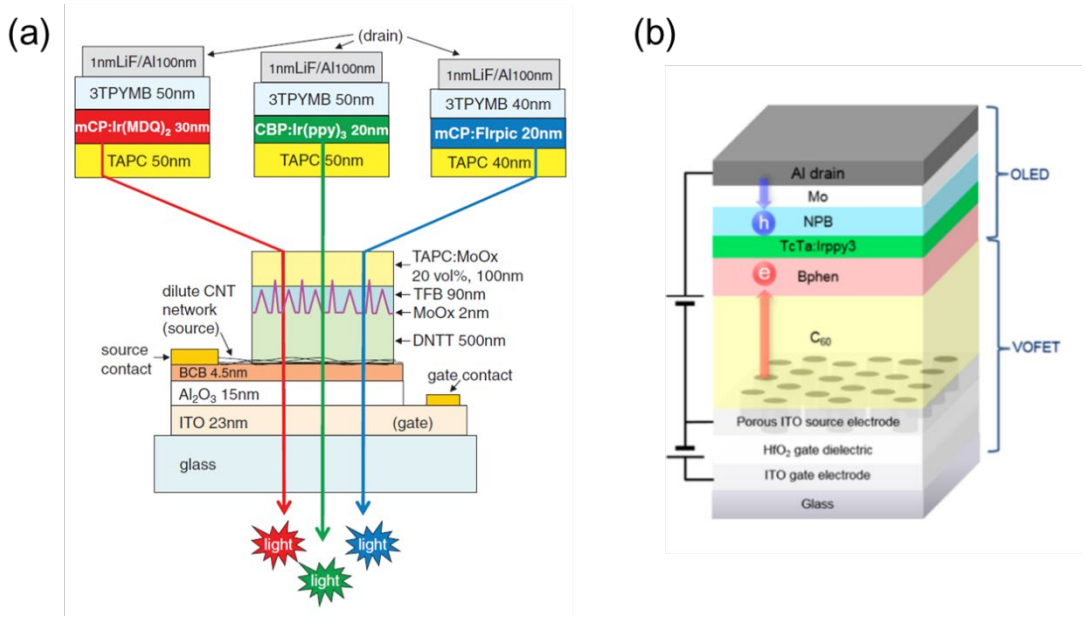

Figure 3-8. Device structure of vertical OLETs based on (a) CNT source electrode[31] and (b) porous ITO source electrode[34].

3.4. Reference

1. Fang, M.; Yang, J.; Li, Z., Light Emission of Organic Luminogens: Generation, Mechanism and Application. *Progress in Materials Science* **2022,** *125*, 100914.

2. Brütting, W.; Frischeisen, J.; Schmidt, T. D.; Scholz, B. J.; Mayr, C., Device Efficiency of Organic Light-Emitting Diodes: Progress by Improved Light Outcoupling. *Physica Status Solidi (a)* **2013,** *210* (1), 44-65.

3. Hepp, A.; Heil, H.; Weise, W.; Ahles, M.; Schmechel, R.; von Seggern, H., Light-Emitting Field-Effect Transistor Based on A Tetracene Thin Film. *Physical Review Letters* **2003,** *91* (15), 157406.

4. Minaev, B.; Baryshnikov, G.; Agren, H., Principles of Phosphorescent Organic Light Emitting Devices. *Physical Chemistry Chemical Physics* **2014,** *16* (5), 1719-1758.

5. Tang, C. W.; VanSlyke, S. A., Organic Electroluminescent Diodes. *Applied Physics Letters* **1987,** *51* (12), 913-915.

6. G. Gustafsson, Y. C., G. M. Treacy, F. Klavetter, N. Colaneri, A. J. Heeger, Flexible Light-Emitting Diodes Made from Soluble Conducting Polymers. *Nature* **1992,** *357* (11), 477-479.

7. Zhang, Z.; Wang, W.; Jiang, Y.; Wang, Y. X.; Wu, Y.; Lai, J. C.; Niu, S.; Xu, C.; Shih, C. C.; Wang, C.; Yan, H.; Galuska, L.; Prine, N.; Wu, H. C.; Zhong, D.; Chen, G.; Matsuhisa, N.; Zheng, Y.; Yu, Z.; Wang, Y.; Dauskardt, R.; Gu, X.; Tok, J. B.; Bao, Z., High-Brightness All-Polymer Stretchable LED with Charge-Trapping Dilution. *Nature* **2022,** *603* (7902), 624-630.

8. Baldo, M. A.; Lamansky, S.; Burrows, P. E.; Thompson, M. E.; Forrest, S. R., Very High-Efficiency Green Organic Light-Emitting Devices Based on Electrophosphorescence. *Applied Physics Letters* **1999,** *75* (1), 4-6.

9. Forster, C.; Heinze, K., Photophysics and Photochemistry with Earth-Abundant Metals-Fundamentals and Concepts. *Chemical Society Reviews* **2020,** *49* (4), 1057-1070.

10. Ma, Y.; Che, C.-M.; Chao, H.-Y.; Zhou, X.; Chan, W.-H.; Shen, J., High Luminescence Gold(I) and Copper(I) Complexes with a Triplet Excited State for Use in Light-Emitting Diodes. *Advanced Materials* **1999,** *11*, 852-857.

11. Volz, D., Review of Organic Light-Emitting Diodes with Thermally Activated Delayed Fluorescence Emitters for Energy-Efficient Sustainable Light Sources and Displays. *Journal of Photonics for Energy* **2016,** *6* (2), 020901.

12. Wu, T.-L.; Huang, M.-J.; Lin, C.-C.; Huang, P.-Y.; Chou, T.-Y.; Chen-Cheng, R.-W.; Lin, H.-W.; Liu, R.-S.; Cheng, C.-H., Diboron Compound-Based Organic Light-Emitting Diodes with High Efficiency and Reduced Efficiency Roll-Off. *Nature Photonics* **2018,** *12* (4), 235-240.

13. Zeng, W.; Lai, H. Y.; Lee, W. K.; Jiao, M.; Shiu, Y. J.; Zhong, C.; Gong, S.; Zhou, T.; Xie, G.; Sarma, M.; Wong, K. T.; Wu, C. C.; Yang, C., Achieving Nearly 30%

External Quantum Efficiency for Orange-Red Organic Light Emitting Diodes by Employing Thermally Activated Delayed Fluorescence Emitters Composed of 1,8-Naphthalimide-Acridine Hybrids. *Advanced Materials* **2018,** *30* (5), 1704961.

14. Lin, T. A.; Chatterjee, T.; Tsai, W. L.; Lee, W. K.; Wu, M. J.; Jiao, M.; Pan, K. C.; Yi, C. L.; Chung, C. L.; Wong, K. T.; Wu, C. C., Sky-Blue Organic Light Emitting Diode with 37% External Quantum Efficiency Using Thermally Activated Delayed Fluorescence from Spiroacridine-Triazine Hybrid. *Advanced Materials* **2016,** *28* (32), 6976-6983.

15. Xu, Z.; Li, S.-H.; Ma, L.; Li, G.; Yang, Y., Vertical Organic Light Emitting Transistor. *Applied Physics Letters* **2007,** *91* (9), 092911.

16. Mashiko, Y.; Taguchi, D.; Manaka, T.; Iwamoto, M.; Weis, M., Direct Visualization and Modeling of Carrier Distribution in Organic Light Emitting Transistor. *Thin Solid Films* **2014,** *554*, 162-165.

17. Natali, M.; Quiroga, S. D.; Passoni, L.; Criante, L.; Benvenuti, E.; Bolognini, G.; Favaretto, L.; Melucci, M.; Muccini, M.; Scotognella, F.; Fonzo, F. D., Toffanin, S., Simultaneous Tenfold Brightness Enhancement and Emitted-Light Spectral Tunability in Transparent Ambipolar Organic Light-Emitting Transistor by Integration of High-k Photonic Crystal. *Advanced Functional Materials* **2017**, *27*, 1605164

18. Li, J.; Zhou, K.; Liu, J.; Zhen, Y.; Liu, L.; Zhang, J.; Dong, H.; Zhang, X.; Jiang, L.; Hu, W., Aromatic Extension at 2,6-Positions of Anthracene toward an Elegant Strategy for Organic Semiconductors with Efficient Charge Transport and Strong Solid State Emission. *Journal of the American Chemical Society* **2017,** *139* (48), 17261-17264.

19. Liu, D.; De, J.; Gao, H.; Ma, S.; Ou, Q.; Li, S.; Qin, Z.; Dong, H.; Liao, Q.; Xu, B.; Peng, Q.; Shuai, Z.; Tian, W.; Fu, H.; Zhang, X.; Zhen, Y.; Hu, W., Organic Laser Molecule with High Mobility, High Photoluminescence Quantum Yield, and Deep-

Blue Lasing Characteristics. *Journal of the American Chemical Society* **2020,** *142* (13), 6332-6339.

20. Qin, Z.; Gao, C.; Gao, H.; Wang, T.; Dong, H.; Hu, W., Molecular Doped, Color-Tunable, High-Mobility, Emissive, Organic Semiconductors for Light-Emitting Transistors. *Science Advances* **2022,** *8*, eabp8775.

21. Förster, T.; Kasper, K., Ein Konzentrationsumschlag der Fluoreszenz. *Physical Chemistry* **1954,** *1* (1), 275-277.

22. Capelli, R.; Toffanin, S.; Generali, G.; Usta, H.; Facchetti, A.; Muccini, M., Organic Light-Emitting Transistors with An Efficiency that Outperforms the Equivalent Light-Emitting Diodes. *Nature Materials* **2010,** *9* (6), 496-503.

23. Yuan, D.; Awais, M. A.; Sharapov, V.; Liu, X.; Neshchadin, A.; Chen, W.; Yu, L., Synergy between Photoluminescence and Charge Transport Achieved by Finely Tuning Polymeric Backbones for Efficient Light-Emitting Transistor. *Journal of the American Chemical Society* **2021,** *143* (13), 5239-5246.

24. Hu, Y.; Song, L.; Zhang, S.; Lv, Y.; Lin, J.; Guo, X.; Liu, X., Improving the Efficiency of Multilayer Organic Light-Emitting Transistors by Exploring the Hole Blocking Effect. *Advanced Materials Interfaces* **2020,** *7* (17), 2000657.

25. Moschetto, S.; Benvenuti, E.; Usta, H.; Ozdemir, R.; Facchetti, A.; Muccini, M.; Prosa, M.; Toffanin, S., Interplay between Charge Injection, Electron Transport, and Quantum Efficiency in Ambipolar Trilayer Organic Light-Emitting Transistors. *Advanced Materials Interfaces* **2022,** *9* (5), 2101926.

26. Muhieddine, K.; Ullah, M.; Maasoumi, F.; Burn, P. L.; Namdas, E. B., Hybrid Area-Emitting Transistors: Solution Processable and with High Aperture Ratios. *Advanced Materials* **2015,** *27* (42), 6677-6782.

27. Gao, H.; Miao, Z.; Qin, Z.; Yang, J.; Wang, T.; Gao, C.; Dong, H.; Hu, W., Redistributed Current Density in Lateral Organic Light-Emitting Transistors Enabling

Uniform Area Emission with Good Stability and Arbitrary Tunability. *Advanced Materials* **2021**, e2108795.

28. Sobus, J.; Bencheikh, F.; Mamada, M.; Wawrzinek, R.; Ribierre, J. C.; Adachi, C.; Lo, S. C.; Namdas, E. B., High Performance p- and n-Type Light-Emitting Field-Effect Transistors Employing Thermally Activated Delayed Fluorescence. *Advanced Functional Materials* **2018,** *28* (28), 1800340.

29. Zhao, C.; Chen, H.; Ali, M. U.; Yan, C.; Liu, Z.; He, Y.; Meng, H., Improving the Performance of Red Organic Light-Emitting Transistors by Utilizing a High-k Organic/Inorganic Bilayer Dielectric. *ACS Applied Materials & Interfaces* **2022,** *14* (32), 36902-36909.

30. Chen, H.; Xing, X.; Miao, J.; Zhao, C.; Zhu, M.; Bai, J.; He, Y.; Meng, H., Highly Efficient Flexible Organic Light Emitting Transistor Based on High-k Polymer Gate Dielectric. *Advanced Optical Materials* **2020,** *8* (6), 1901651.

31. McCarthy, M. A.; Liu, B.; Donoghue, E. P.; Kravchenko, I.; Kim, D. Y.; So, F.; Rinzler, A. G., Low-Voltage, Low-Power, Organic Light-Emitting Transistors for Active Matrix Displays. *Science* **2011,** *332*, 570.

32. Mohd Sarjidan, M. A.; Shuhaimi, A.; Majid, W. H. A., Observation of Saturation Transfer Characteristics in Solution Processed Vertical Organic Field-Effect Transistors (VOFETs) with High Leakage Current. *Current Applied Physics* **2018,** *18* (11), 1415-1421.

33. Chen, Q.; Yan, Y.; Wu, X.; Lan, S.; Hu, D.; Fang, Y.; Lv, D.; Zhong, J.; Chen, H.; Guo, T., High-Performance Quantum-Dot Light-Emitting Transistors Based on Vertical Organic Thin-Film Transistors. *ACS Applied Materials & Interfaces* **2019,** *11* (39), 35888-35895.

34. Yu, H.; Dong, Z.; Guo, J.; Kim, D.; So, F., Vertical Organic Field-Effect Transistors for Integrated Optoelectronic Applications. *ACS Applied Materials & Interfaces* **2016,**

8 (16), 10430-10435.

Chapter 4. Synaptic Plasticity Powering LAOLETs

Organic light-emitting transistors (OLETs) have gained a notable attention during the last few years as opto-electronic functional element for the fabrication of the next generation of active-matrix display. OLETs indeed simultaneously integrates the functions of light-emission, gate-modulated electrical switching and optically switchable operation modes. Such multifunctional nature is instrumental for smart display technologies.[1-8] Upon conversion of triplet excitons into singlet excitons via "reverse intersystem crossing", thermally activated delayed fluorescence (TADF) materials can harvest energy electrons from both the singlet and triplet states thereby contributing to light-emission. Such unique class of materials are regarded as ideal candidates for low-cost and highly efficient light-emitting devices.[9-13] During the last few years, high-performance OLETs with high external quantum efficiencies based on TADF materials have been reported.[14]

Organic afterglow, also called persistent photoluminescence, is a well-known long-lived emission phenomenon in which photoluminescence of the pure organic materials can persists for several seconds after light irradiation is ceased.[15,16] Organic afterglow emitting materials have raised quite some interests in view of their potential application in the optical data storage, sensors, in-vivo imaging and anti-counterfeiting.[17-22] However, many are the challenges limiting the practical applications of organic afterglow, including the light-emitting color tunability, lifetimes of organic luminescence and phosphorescence quantum yield. Moreover, the need for stringent molecular design principles, e.g. promoting H-aggregates in solid state to stabilize the generated triplet exciton, jeopardizes the implementation of a long afterglow function in organic opto-electronic devices.[23]

Persistent photoconductivity (PPC) is another delayed response phenomenon common in opto-electronics which can be found in devices comprising various types of amorphous metal oxide semiconductors such as InZnO (IZO), InGaZnO (IGZO),

and ZnSnO (ZTO).[24-26] Due to the dynamic nature of the process relying on the ionization of oxygen vacancies, electron density is increased upon the irradiation of UV photons thus increasing the conductance of these materials. After ceasing the UV irradiation, conductance slowly decreases going gradually through low resistance states due to the slow recombination rate of electrons and oxygen vacancies.[27-30] Since this behavior highly resembles the plasticity phenomenon in biological synapses or neural systems, metal oxide semiconductors can be potentially exploited as active layers in the fabrication of artificial synaptic field-effect transistors to attain a short- and long-term memory.[31-37]

In this chapter, we present a long afterglow organic light-emitting field-effect transistor (LAOLETs), whose device architecture relies on an IGZO FET possessing synaptic characteristics. In particular, the IGZO channel has been designed to feature post-synaptic current flow capable of driving the light-emission. Synaptic plasticity is realized by generating oxygen vacancies in IGZO via UV irradiation, leading to slow electron-oxygen vacancy recombination kinetics. Moreover, synaptic characteristics of solution processed IGZO are investigated and tuned by varying the concentration of In atoms, thereby optimizing IGZO thin-film function as channel layer with a long-term potentiation property. Subsequently, TADF organic light-emissive layers have been deposited onto the IGZO channel yielding an area light-emission. We demonstrate that synaptic behaviour of IGZO is retained after deposition of the organic light-emissive layer. Significantly, our devices display electroluminescence with a unique synaptic property. By varying the gate bias, our LAOLETs exhibit persistent light-emission featuring variable lifetime after exposure to UV stimulus. In absence of an applied gate voltage, such a synaptic plasticity facilitated afterglow emission has a lifetime exceeding 270 s, after 50 s UV irradiation. In contrast to conventional long afterglow devices requiring specific design of room-temperature phosphorescence materials, our strategy makes use of electronic means arising from oxygen-vacancies in metal-oxides, to achieve similar device functions. Finally, time-dependent synaptic-type afterglow in

LAOLETs is displayed and systematically characterized.

4.1. Experimental Method

Indium nitrate hydrate ($In(NO_3)_3 \cdot xH_2O$, 99.9%), gallium nitrate hydrate ($Ga(NO_3)_3 \cdot xH_2O$, 99.9%), Zinc acetate dehydrate ($Zn(OAc)_2 \cdot 2H_2O$, 99.9%) and 4,4′-Bis(N-carbazolyl)-1,1′-biphenyl (CBP) were purchased from Sigma–Aldrich. Poly[9,9-bis(60-(N,Ndiethylamino)hexyl)-fluorene-alt-9,9-bis(3-ethyl(oxetane-3-ethyoxy)-hexyl)-fluorene] (PFNOX) and 9,10-bis(4-(9H-carbazol-9-yl)-2,6-dimethylphenyl)-9,10-diboraanthracene (CzDBA) were purchased from Lumtec. N,N′-Di(1-naphthyl)-N,N′-diphenyl-(1,1′-biphenyl)-4,4′-diamine (NPB) were purchased from Ossila. All the materials were used as received, without any further purification.

Preparation of IGZO Precursor Solution. $In(NO_3)_3 \cdot xH2O$, $Ga(NO_3)_3 \cdot xH_2O$ and $Zn(OAc)_2 \cdot 2H_2O$ were dissolved in 2-methoxyethanol at concentration at 0.2 M respectively and stirred at room temperature overnight. Upon mixture, IGZO precursor solution was obtained.

Preparation of PFNOX solution. 10 mg PFNOX were dissolved in 5 mL methanol and 50 μL acetic acid and then stirred at 80 °C overnight. The solutions were filtered through 0.22 μm PTFE filter before being spin-coated.

Preparation of green emitting solution. 90 mg CBP and 10mg CzDBA were dissolved in 10 mL toluene and then stirred at 80 °C overnight. The solutions were filtered through 0.22 μm PTFE filter before being spin-coated.

Devices were fabricated on the substrates of n++ Si as bottom gate and 230 nm of thermally grown SiO_2 as the gate dielectric (IPMS Fraunhofer Institute). The Si/SiO_2 substrates were cleaned with water, acetone, and alcohol in sequence and dried under N_2 flow. The cleaned substrates were further treated with UV-ozone for 20 min. The IGZO precursor solution was spin-coated at 3000 rpm for 45 s on the silicon wafer. Subsequently, the substrate was dried at 150 °C for 5 min and baked at 380 °C for 30

min.

For IGZO single layer transistor: Interdigitated Al electrodes (50 nm) were deposited on the IGZO film through shadow masks. (Figure 4-1a)

For LAOLETs: LAOLETs have been fabricated with a lateral IGZO channel and a vertically-stacked organic emissive layer. Figure 4-1b portrays the architecture of Si/SiO_2/IGZO/Al/PFNOX/light-emission layer/NPB/Au. The light-emission layer comprises CzDBA as a TADF green light-emitting material hosted in a CBP matrix.[38] To balance of electron and hole charge carrier concentration in emission layer, PFNOX and NPB were employed as electron and hole transporting layer, respectively. Complementary electrodes were deposited through aligned shadow masks and optical images of typical device were captured as Figure 4-1c and 4-1d. The energy levels and chemical structures of these materials are displayed in Figure 4-1e and 4-1f, respectively.

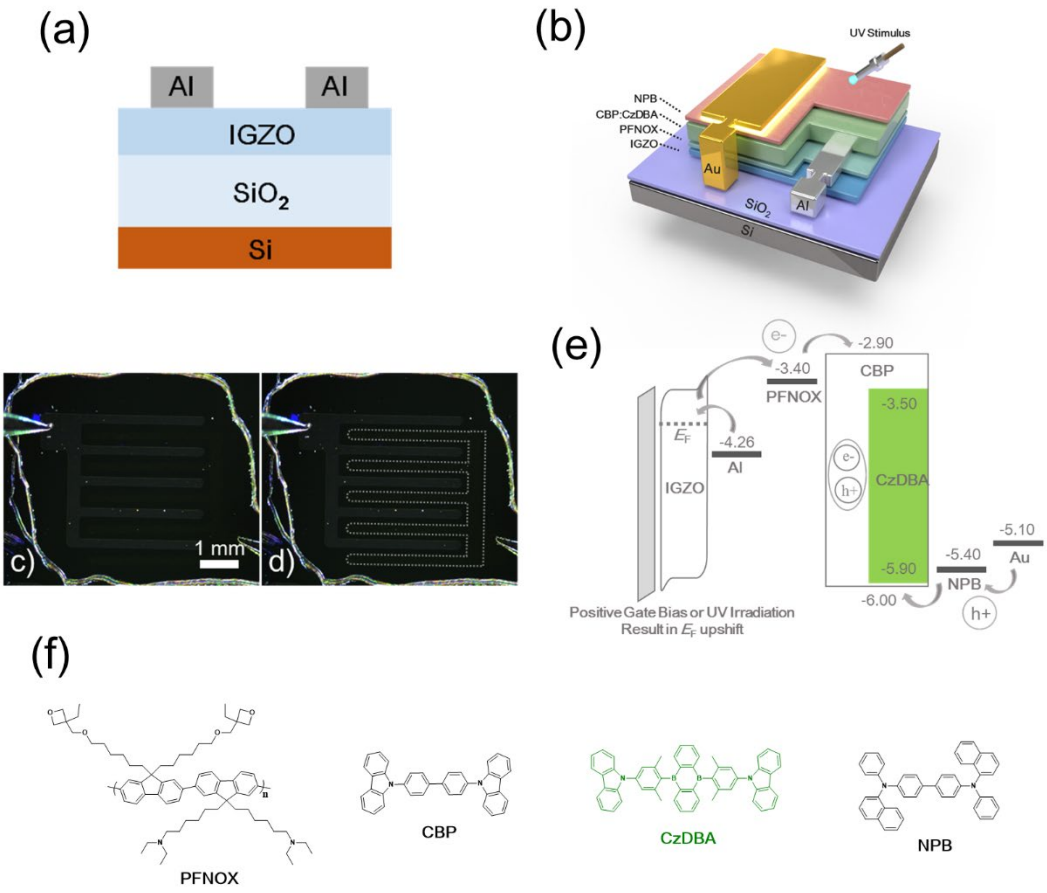

Figure 4-1. Device structure of (a) IGZO-single layer transistor and (b) IGZO-based LAOLETs. c) Optical micrograph of LAOLETs with d) the highlight of its emission zone. e) Energy levels and f) chemical structures of CBP, CzDBA, PFNOX, and NPB.

Devices were characterized in a dry and nitrogen-filled glove-box. The electrical characteristics and basic synaptic functions were measured by making use of a semiconductor parameter analyzer (Keithley 2636). Irradiation intensity of device were measured by a photodiode (HAMAMATSU S3204-08) which have been previously calibrated by a luminance meter (KONICA MINOLTA, LS-100). Light power of 312 nm UV irradiation for synaptic transistors was kept at 3 μW mm^{-2}. Light power of 312 nm UV irradiation for LAOLETs was kept at 3 μW mm^{-2} with 45° incident angle. Due to the oblique irradiation of UV light and the absorption by charge transport layer and emission layer, the post-synaptic current of LAOLETs were lower than that of IGZO

synaptic transistors after UV stimulus with the same light intensity.

4.2. Synaptic Transistors Based on Inorganic Metal Oxide

Firstly, transistors containing a mono-component IGZO layer as active material were fabricated to explore the synaptic behavior of IGZO. A bottom-gate, top-contact geometry, denoted as $Si/SiO_2/IGZO/Al$, was chosen. The IGZO layer with a thickness of ~20 nm was deposited through sol-gel method on the Si substrate covered with a 230 nm thick layer of thermally grown SiO_2. A formulation of metal precursors made of indium nitrate, gallium nitrate, and zinc acetate were dissolved in 2-methoxyethanol, respectively. 50 nm Al layer as top contacts was deposited through a shadow mask by thermal evaporation, serving as interdigitated source and drain electrodes.

An amorphous metal-oxide thin films have been employed not only as N-type channel layer but also memory function layer due to their high mobility and PPC characteristic. Upon UV irradiation, electrons present in excess on the IGZO surface absorb energy to be released into the bulk. This process is generally attributed to the ionization of oxygen vacancies (single charged ($V_O \rightarrow V_O^+ + e^-$) or double charged (or $V_O \rightarrow V_O^{2+} + 2e^-$)), as illustrated in Figure 4-2. This increase in electron density leads to the upshift of the Femi level (E_F) of IGZO, which in turn effectively reduces the injection barrier height between IGZO and metal (Al) contacts. In this way, IGZO based FETs can persistently retain their low resistance state without the application of a gate bias, as a result of the slow neutralization or recombination rate of released electron with oxygen vacancies.

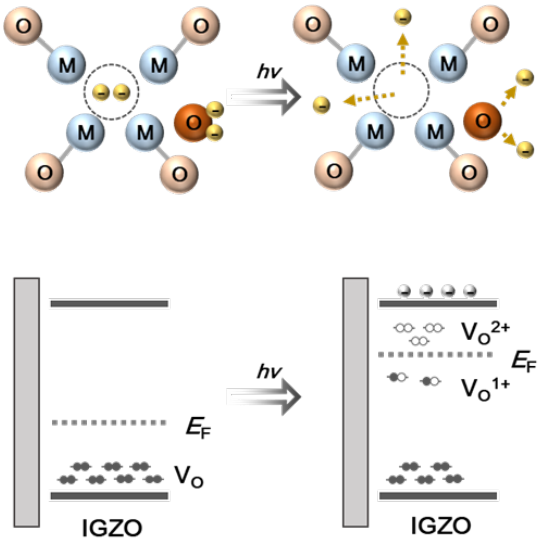

Figure 4-2. Schematic images of working mechanism of PPC.

The solution-processing of IGZO has the advantage that the atom ratio of the metal ion in the amorphous metal oxide can be optimized easily by tuning the mixing ratio of the precursor in the solution. Atom ratio of Ga and Zn were kept at 1:1, and the percentage of In was varied from 50%, 65% to 80%. Atomic force microscopy (AFM) topographical images revealed an ultra-smooth surface of the IGZO film with a root-square-mean roughness (R_{RMS}) of about 0.2 nm as determined in an area of 5 × 5 μm^2. The ultra-flatness of this surface is potentially advantageous for multilayer stack formation (Figure 4-3a to 4-3c). Transfer curves of IGZO-based transistors recorded by using different indium content are displayed in Figure 4.3d to 4.3f. We found that the atom ratio of indium in IGZO film strongly influences the device performance, including its threshold voltage (V_{Th}), its electron mobility and its light response behavior.[39] When irradiated for 5 second with a 312 nm UV light, IGZO films with low-indium-ratio (50%) did not show any obvious V_{Th} shift and current change, whereas IGZO films with 65% and 80%-In content exhibited a negative shift of the V_{Th}. However, before UV irradiation, high-indium-ratio (80%) IGZO films showed a notable negative shift of V_{Th} while the changes of the off-state current were modest.

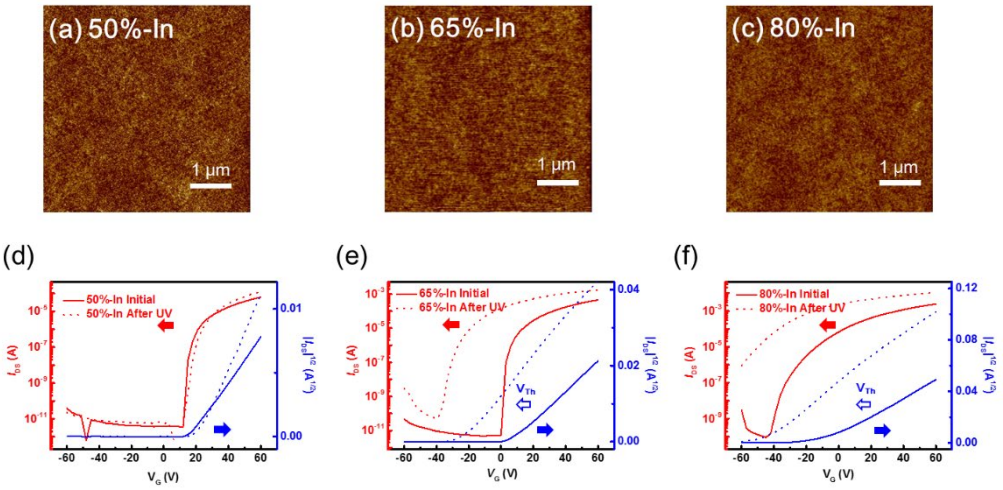

Figure 4-3. AFM images of IGZO thin film with different In-atom percentage of a) 50%-In, b) 65%-In, and c) 80%-In. Z-scales = 2 nm. Transfer curves for d) 50%-In, e) 65%-In, and f) 80%-In IGZO-based transistors.

For IGZO films with In ratio of 65%, the V_{Th} is positioned ca. at 0 V, thus allowing the device to be fabricated as two-terminal memory resistors as a comparative device for control experiments. Hence, 65%-In IGZO films were chosen in order to exploit its synapse behavior when integrated in LAOLETs. Normalized different gate-bias time-dependent measurement of the 65%-In IGZO-based transistors after UV light illumination were also measured and shown in Figure 4-4a. The lifetime (τ_l) of the devices can be determined from the decay curves according to the exponential equation $I(t) = I_0 \times \exp(-t/\tau_l) + I_\infty$, where I_0 is the initial current and I_∞ is the steady-state current. Under zero gate bias, the current undergoes a slow kinetics decay from on-state to off-state (baseline), with a lifetime of 190 s (Figure 4-4b). Conversely, when a gate voltage of −20 V and −40 V was applied we observed a negative gate bias induced faster current decay whose lifetime amounts to 118 s and 88.5 s, respectively (Figure 4-4c and 4-4d).[40] These changes in the decay dynamics of on-state currents clearly demonstrate that the V_{Th} and synaptic relaxation behavior can be well tuned by varying the indium ratio in the precursor solution and the operation gate voltage, respectively.

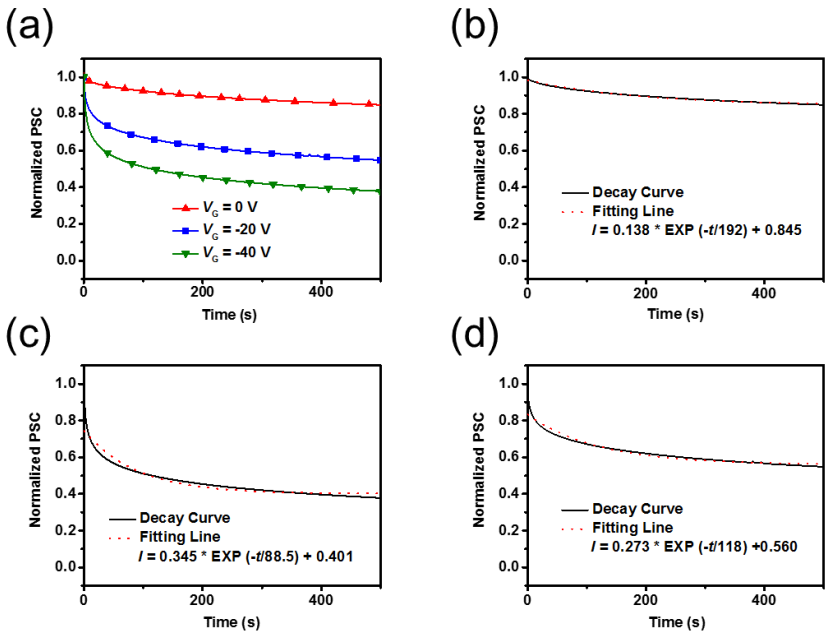

Figure 4-4. (a) Decay curve and fitting line of post-synaptic current (PSC) of 65%-In IGZO transistor after one UV stimulus when b) V_G = 0 V, c) −20 V, d) −40 V were applied.

After prolonged exposure time to UV irradiation, transfer curves of 65%-In IGZO-based transistor were immediately measured for comparison. Transfer curves of this transistor before and after UV irradiation are displayed in Figure 4-5a. The relevant devices parameters are summarized in Table 4-1. Upon the exposure to UV light the field-effect mobilities exhibited a modest yet gradual increase from 0.151 to 0.358 $cm^2 V^{-1} s^{-1}$. On the same time, V_{Th} shifted gradually towards negative value, from 4.86 V to −111 V, and the I_{on}/I_{off} ratio of device decreased correspondingly. This observation provides evidence that the enhanced-mode FET operation can be converted into depletion-mode upon 25 s exposure to 312 nm UV light with an increase of the I_{DS} (at V_G = 0 V) up to magnitude of 10^{-3} A. For the sake of comparison, the pristine IGZO in its off-state (at zero gate bias) displays I_{DS} of a few picoampere.

Synaptic plasticity is one of most crucial characteristics for synaptic devices and it

is associated with short- and long-term memory.[41] Decaying characteristics of post-synaptic current (PSC) with one UV-stimulus and five UV-stimulus are portrayed in Figure 4-5b. When a single 5 seconds lasting irradiation of 312 nm UV light with an intensity of 3 μW mm^{-2} was applied, the synaptic device exhibited short-term plasticity (STP) with a rapid decay of the PSC to its initial state after the UV stimulus on the few tens of seconds timescale. However, when five UV light irradiations with the same intensity and width at intervals of 1 min were applied, the device displayed long-term plasticity (LTP) behavior, with the high-current state persisting for a longer period of time (280 sec, Figure 4-5c). These observations can be attributed to the slow recombination kinetics of such electrons with oxygen vacancies, thereby producing an accumulated or high density of free electrons in the channel. This finding is in line with literature showing that the adjustment of memory behavior can be controlled by varying the exposure time to UV light.[42] Such a LTP behavior of the transistor provides the tool to power the light emitting material for a long-lasting emission.

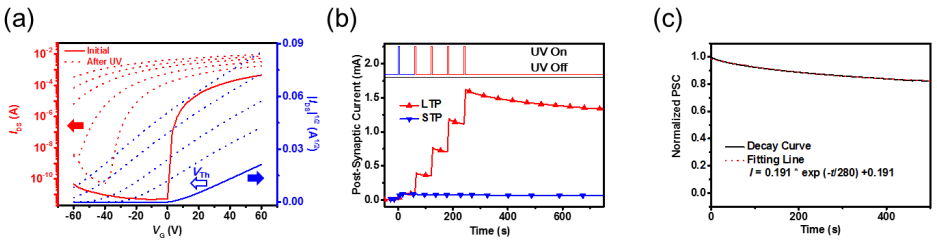

Figure 4-5. (a) Transfer curves for 65%-In IGZO-based transistors before and after five times 5 s UV irradiation. (b) Time dependent measurement of 65%-In IGZO-based transistors with five times stimulus and one time stimulus, which show the LTP and STP. (c) Decay curve and fitting line of post-synaptic current (PSC) of 65%-In IGZO transistor after five UV stimulus when V_G = 0 V.

4.3. Long Afterglow OLETs Based on Inorganic Metal Oxide

The synaptic memory behaviour of IGZO was observed also in the multi-layer LAOLETs devices. Device electrical and optical output curves are portrayed in Figure

4-6a where the applied gate voltages (V_G) ranged from −60 V to 60 V and drain voltages (V_D) was swept from −20 V to 40 V. The width (W) and length (L) of the channel amounted to 27×10^3 μm and 200 μm, respectively, whereas the emission area was defined as 4.22 mm^2. The brightness of devices was found to increase with the drain-source current. When V_G of 60 V and V_D of 40 V were applied, the brightness reached 196 cd m^{-2}. Photoluminescence spectra of the emission layer and electroluminescence spectra of LAOLETs are displayed (Figure 4-6b). The maximum emission peak of photoluminescence (PL) spectra was positioned at 525 nm, while that of electroluminescence spectra was observed at 549 nm. This value corresponds to color coordinates of (0.37, 0.57) from Commission Internationale de l'Eclairage (CIE) (Figure 4-6c). This slightly redshift in spectra of LAOLETs was caused by the presence of NPB and Au layer (Figure 4-6d) which can be further optimized in the future work.

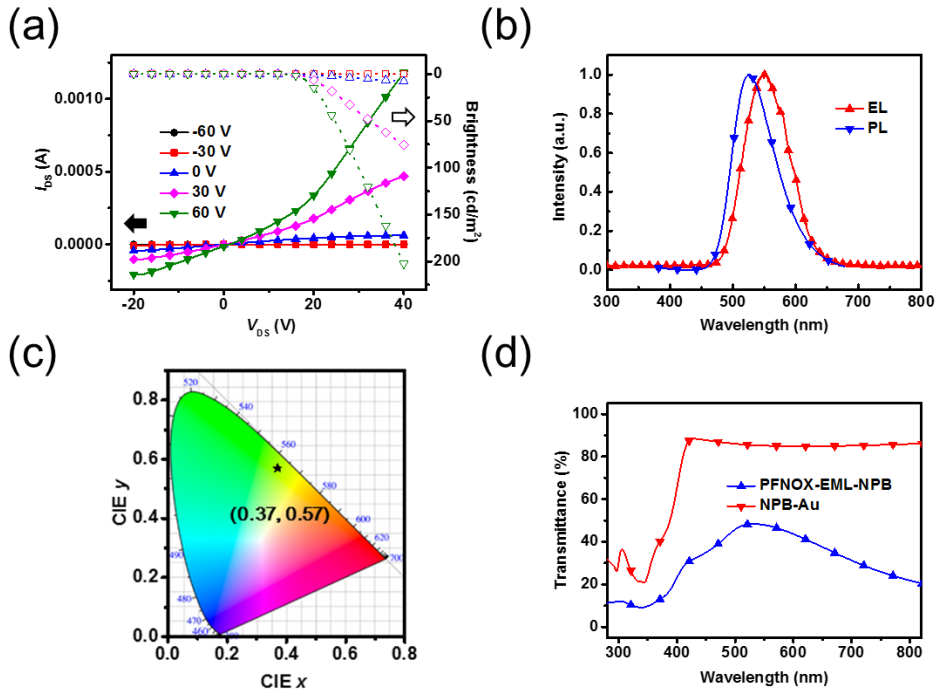

Figure 4-6. (a) Optical-electrical output curves for LAOLETs. (b) Electroluminescence spectra of CBP:CzDBA based LAOLETs and fluorescence spectra of CBP:CzDBA thin film (excitation wavelength = 350 nm). (c) The corresponding CIE coordinates of

electroluminescence spectra. (d) Transmittance spectra of PFNOX-EML-NPB layers and NPB-Au layers.

Electrical and optical transfer curves of LAOLETs were measured immediately after 10 second UV oblique irradiation with intensity of 3 μW mm^{-2} (Figure 4-7a). Similar to synaptic transistor based on a neat IGZO layer, V_{Th} of device also displayed a gradual negative shift with the UV irradiation, from −12.0 V to −29.4 V, accompanied by light turn-on voltage (V_{on}) negative shift from 3.0 V to −9.7 V, where V_{on} of the LAOLETs were defined from optical transfer curves by extrapolating the straight line portion of the curves (against the V_G axis, Figure 4-7b). The detailed device parameters are reported in Table 4-2. Time dependence measurement of the same LAOLETs device just differing by the absence of the IGZO layer, were carried out (see Figure 4-7c and 4-7d). The nearly negligible change in current as a result of UV irradiation indicates that the PSC in our LAOLETs is due to the light-responsive nature of the IGZO layer.

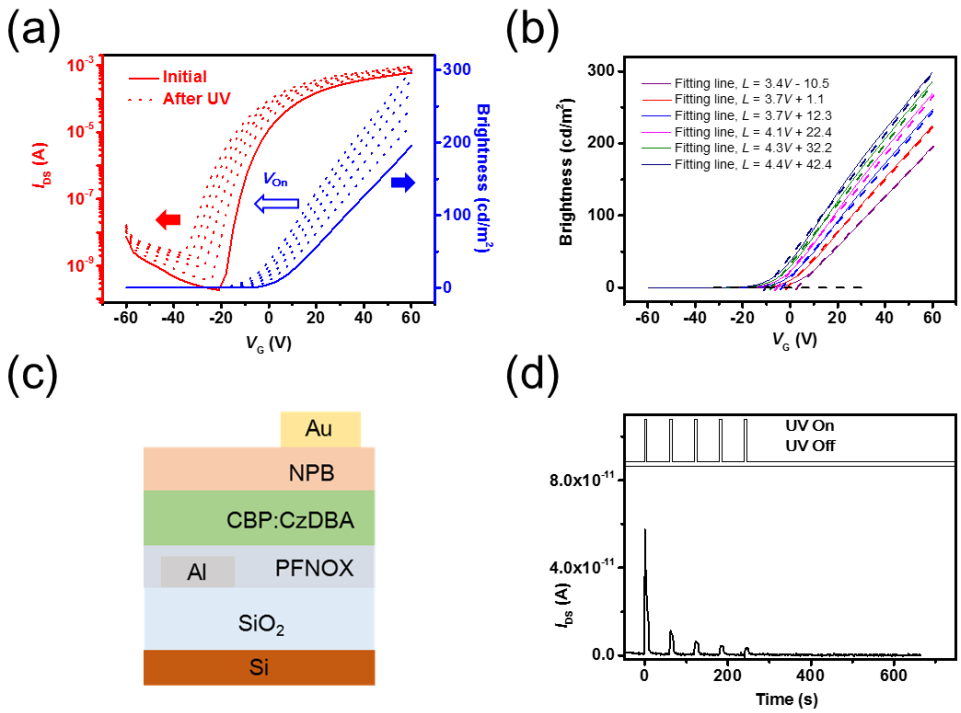

Figure 4-7. (a) Optical-electrical transfer curves for LAOLETs. (b) Fitting line of

optical transfer curves for LAOLETs before and after UV stimulus, where L is brightness and V is V_G. (c) Device structure of reference LET in absence of the IGZO layer. (d) Time-dependent measurement of this device response to five UV irradiations.

Time-dependence PSC and post-synaptic brightness (PSB) of the LAOLETs are displayed in Figure 4-8a and 4-8b. The reveal a similar PSC trend thus indicating that multi-layer fabrication process did not influence the PPC behavior of the channel layer. More importantly, electroluminescence of LAOLETs and post-synaptic brightness exhibited the similar trend with PSC, characterized by a long-lived emission after the UV light is turned off, providing unambiguous evidence for the afterglow nature of the emission. The decay ratio of PSB was attributed to the degeneration of organic emission materials, and it resulted being slightly faster than that of PSC, yet the latter can be optimized after encapsulation or embedding state-of-art light-emission materials.[43] Electroluminescence lifetime (τ_l) of LAOLETs can be also determined from the time-resolved decay of luminescent intensity in the exponential decay equation: $L(t) = L_0 \times \exp(-t/\tau_l) + L_\infty$, where L_0 is the initial fluorescence strength at starting time (t = 0). Under V_G = 0 V, after 50 s UV stimulus, brightness of 11 cd m^{-2} was achieved, and τ_l of 272 s was calculated (Figure 4-8c). However, under V_G = −30 V, lower brightness of 4 cd m^{-2} and shorter τ_l of 159 s were observed (Figure 4-8d), which indicates that V_G can be used as a remote control giving access to different decay constants. Moreover, for this kind of LAOLETs, the application of one and five UV irradiation stimuli under both V_G = 0 V and −30 V resulted in STP and LTP, respectively, being consistent with synaptic transistors and also indicating that luminescence efficiency and lifetime can be enhanced upon prolonging the UV irradiation. Time dependent measurement of LAOLETs with input duration five times longer (*i.e.* amounting to 20 sec) were carried out and the results are presented in Figure 4-8e and 4-8f. While the PSB retention was not prolonged being ruled by the decay of organic emitting materials, the PSC exhibited longer retention times. Compared with room-temperature phosphorescent materials,

which is well known that high quantum yield and long lifetime are difficult to be achieved simultaneously,[44,45] our LAOLETs display a greater technological potential for long afterglow display application.

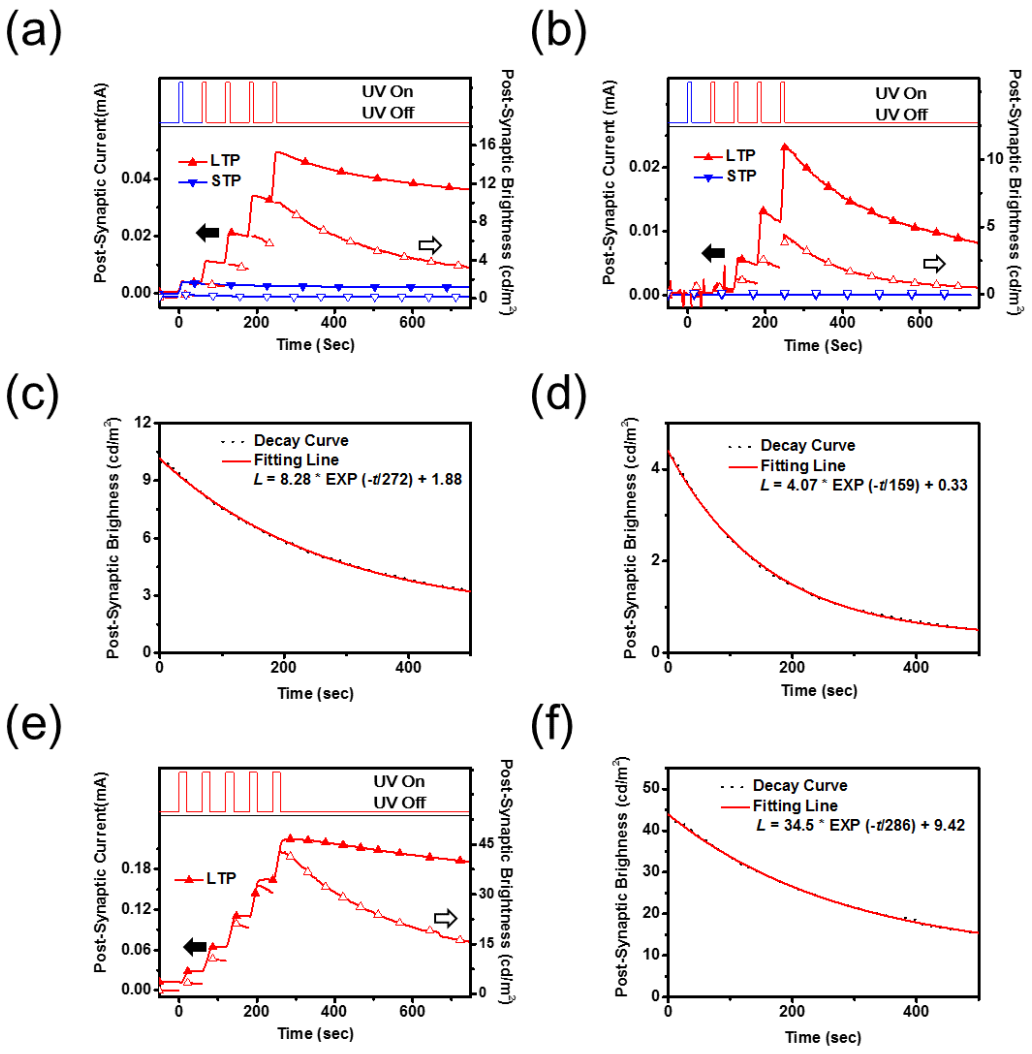

Figure 4-8. Time dependent measurement of LAOLETs with five times stimulus and one time stimulus, where V_G was (a) 0V and (b) −30 V. Decay curve and fitting line of post-synaptic brightness of LAOLETs when (c) V_G = 0 V and (d) V_G = −30 V were applied. (e) Time dependent measurement of LAOLETs with five times stimulus of 20 seconds width, where V_G was 0 V. (f) Corresponding decay curve and fitting line of post-synaptic brightness of LAOLETs.

Optical image of LAOLETs under driven voltage before and after UV irradiation are displayed in the Figure 4-9.

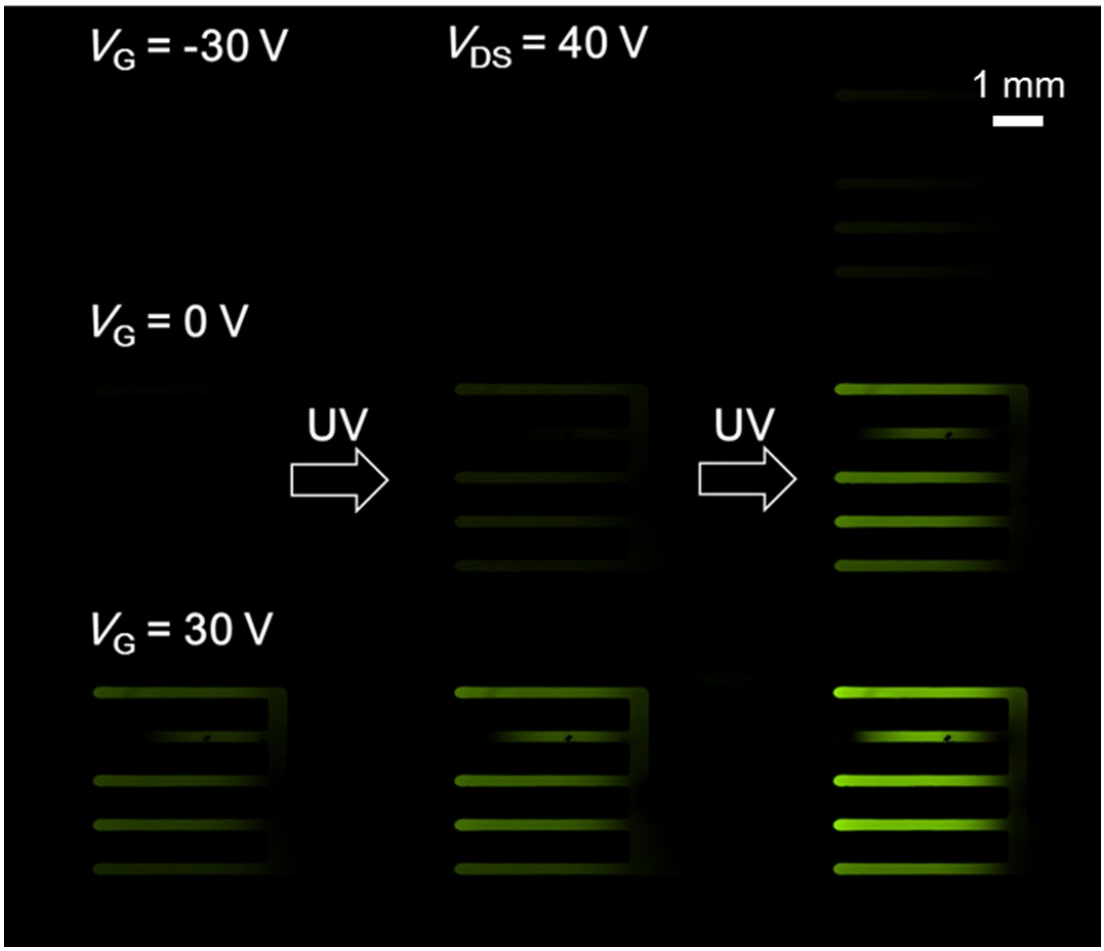

Figure 4-9. Typical microscopy images of LAOLETs after twice 20s UV stimulus when V_G with −30V, 0V and 30V were applied.

Table 4-1. Summary of parameter of 65%-In IGZO-based transistor under different times UV irradiation.

	Mobility ($cm^2\ V^{-1}\ s^{-1}$)	V_{Th} (V)	I_{on}/I_{off}
Initial	0.151	4.86	10^7
312nm-5s	0.275	−24.8	10^6

312nm-10s	0.322	−45.8	10^5
312nm-15s	0.331	−71.8	10^3
312nm-20s	0.348	−89.9	10^2
312nm-25s	0.358	−111	10

Table 4-2. Summary of parameter of LAOLETs under different times UV irradiation.

	Mobility ($cm^2\ V^{-1}\ s^{-1}$)	V_{Th} (V)	V_{on} (V)
Initial	0.128	−12.0	3.0
312nm-10 s	0.130	−16.2	0.3
312nm-20 s	0.130	−20.0	−3.1
312nm-30 s	0.132	−23.2	−5.3
312nm-40 s	0.132	−26.1	−7.5
312nm-50 s	0.129	−29.4	−9.7

4.4. Conclusions

In summary, in this chapter, we firstly developed the UV-spiked LAOLETs whose PSB was powered by PSC. This long afterglow function is achieved by coupling an optical synaptic IGZO channel layer with an organic TADF light-emissive layer. Irradiation with UV light at λ=312 nm leads to the production of oxygen vacancies in the IGZO layer which free electrons in excess yielding to an increase in the channel conductance and decay under the control of V_G. Upon UV irradiation, both V_{Th} of

electrical transfer curves and V_{on} of optical transfer curves shift negatively. As a result, PSB of 11 cd m^{-2} with lifetime of 272 sec were achieved without the applied V_G. And lower PSB of 4 cd m^{-2} with shorter lifetime of 159 sec were observed when V_G of −30 V is applied.

4.5. Reference

1. Chin, X. Y.; Cortecchia, D.; Yin, J.; Bruno, A.; Soci, C., Lead Iodide Perovskite Light-Emitting Field-Effect Transistor. *Nature Communications* **2015,** *6*, 7383.

2. Capelli, R.; Toffanin, S.; Generali, G.; Usta, H.; Facchetti, A.; Muccini, M., Organic Light-Emitting Transistors with An Efficiency that Outperforms the Equivalent Light-Emitting Diodes. *Nature Materials* **2010,** *9*, 496

3. Hou, L.; Zhang, X.; Cotella, G. F.; Carnicella, G.; Herder, M.; Schmidt, B. M.; Patzel, M.; Hecht, S.; Cacialli, F.; Samorì, P., Optically Switchable Organic Light-Emitting Transistors. *Nature Nanotechnology* **2019,** *14* (4), 347-353.

4. Qin, Z.; Gao, H.; Liu, J.; Zhou, K.; Li, J.; Dang, Y.; Huang, L.; Deng, H.; Zhang, X.; Dong, H.; Hu, W., High-Efficiency Single-Component Organic Light-Emitting Transistors. *Advanced Materials* **2019,** *31* (37), 1903175.

5. Muhieddine, K.; Ullah, M.; Pal, B. N.; Burn, P.; Namdas, E. B., All Solution-Processed, Hybrid Light Emitting Field-effect Transistors. *Advanced Materials* **2014,** *26* (37), 6410-6415.

6. Muhieddine, K.; Ullah, M.; Maasoumi, F.; Burn, P. L.; Namdas, E. B., Hybrid Area-Emitting Transistors: Solution Processable and with High Aperture Ratios. *Advanced Materials* 2015, 27 (42), 6677-6782.

7. Zaumseil, J.; Sirringhaus, H., Electron and Ambipolar Transport in Organic Field-Effect Transistors. *Chemical Reviews* **2007,** *107*, 1296-1323.

8. Zaumseil, J.; Friend, R. H.; Sirringhaus, H., Spatial Control of the Recombination

Zone in An Ambipolar Light-Emitting Organic Transistor. *Nature Materials* **2006,** *5*, 69-74.

9. Uoyama, H.; Goushi, K.; Shizu, K.; Nomura, H.; Adachi, C., Highly Efficient Organic Light-Emitting Diodes from Delayed Fluorescence. *Nature* **2012,** *492* (7428), 234-238.

10. Hirata, S.; Sakai, Y.; Masui, K.; Tanaka, H.; Lee, S. Y.; Nomura, H.; Nakamura, N.; Yasumatsu, M.; Nakanotani, H.; Zhang, Q.; Shizu, K.; Miyazaki, H.; Adachi, C., Highly Efficient Blue Electroluminescence Based on Thermally Activated Delayed Fluorescence. *Nature Materials* **2015,** *14* (3), 330-336.

11. Nakanotani, H.; Higuchi, T.; Furukawa, T.; Masui, K.; Morimoto, K.; Numata, M.; Tanaka, H.; Sagara, Y.; Yasuda, T.; Adachi, C., High-Efficiency Organic Light-Emitting Diodes with Fluorescent Emitters. *Nature Communications* **2014,** *5*, 4016.

12. Barnes, B., Reflected Phonons Reveal Strong Coupling. *Nature Photonics* **2021,** *15* (3), 169-170.

13. Jeon, S. O.; Lee, K. H.; Kim, J. S.; Ihn, S.-G.; Chung, Y. S.; Kim, J. W.; Lee, H.; Kim, S.; Choi, H.; Lee, J. Y., High-Efficiency, Long-Lifetime Deep-blue Organic Light-Emitting Diodes. *Nature Photonics* **2021**, *15* (3), 208-215.

14. Song, L.; Hu, Y.; Liu, Z.; Lv, Y.; Guo, X.; Liu, X., Harvesting Triplet Excitons with Exciplex Thermally Activated Delayed Fluorescence Emitters toward High Performance Heterostructured Organic Light-Emitting Field Effect Transistors. *ACS Applied Materials & Interfaces* **2017**, *9* (3), 2711-2719.

15. Zhao, W.; He, Z.; Tang, B. Z., Room-temperature phosphorescence from organic aggregates. *Nature Reviews Materials* **2020**, *5* (12), 869-885.

16. Xu, S.; Chen, R.; Zheng, C.; Huang, W., Excited State Modulation for Organic Afterglow: Materials and Applications. *Advanced Materials* **2016**, *28* (45), 9920-9940.

17. Yang, X.; Yan, D., Strongly Enhanced Long-Lived Persistent Room Temperature Phosphorescence Based on the Formation of Metal-Organic Hybrids. *Advanced Optical Materials* 2016, *4* (6), 897-905.

18. Katsurada, Y.; Hirata, S.; Totani, K.; Watanabe, T.; Vacha, M., Photoreversible On-Off Recording of Persistent Room-Temperature Phosphorescence. *Advanced Optical Materials* **2015,** *3* (12), 1726-1737.

19. Wang, S.; Wu, D.; Yang, S.; Lin, Z.; Ling, Q., Regulation of Clusterization-Triggered Phosphorescence from A Non-Conjugated Amorphous Polymer: A Platform for Colorful Afterglow. *Materials Chemistry Frontiers* **2020,** *4* (4), 1198-1205.

20. Xu, L.; Zhou, K.; Ma, H.; Lv, A.; Pei, D.; Li, G.; Zhang, Y.; An, Z.; Li, A.; He, G., Ultralong Organic Phosphorescent Nanocrystals with Long-Lived Triplet Excited States for Afterglow Imaging and Photodynamic Therapy. *ACS Applied Materials & Interfaces* **2020,** *12* (16), 18385-18394.

21. Xie, C.; Zhen, X.; Miao, Q.; Lyu, Y.; Pu, K., Self-Assembled Semiconducting Polymer Nanoparticles for Ultrasensitive Near-Infrared Afterglow Imaging of Metastatic Tumors. *Advanced Materials* **2018,** *30* (21), 1801331.

22. An, Z.; Zheng, C.; Tao, Y.; Chen, R.; Shi, H.; Chen, T.; Wang, Z.; Li, H.; Deng, R.; Liu, X.; Huang, W., Stabilizing Triplet Excited States for Ultralong Organic Phosphorescence. *Nature Materials* **2015,** *14* (7), 685-690.

23. Kabe, R.; Notsuka, N.; Yoshida, K.; Adachi, C., Afterglow Organic Light-Emitting Diode. *Advanced Materials* **2016,** *28* (4), 655-660.

24. Jang, J.; Hong, Y., Effects of Lithium Doping and Ultraviolet Photo-Patterning on Electrical Properties of InGaZnO Thin Film Transistors. *Thin Solid Films* **2020,** *707*, 138098.

25. Lee, S.; Nathan, A.; Jeon, S.; Robertson, J., Oxygen Defect-Induced Metastability in Oxide Semiconductors Probed by Gate Pulse Spectroscopy. *Scientific Reports* **2015,**

5, 14902.

26. Jeon, S.; Ahn, S. E.; Song, I.; Kim, C. J.; Chung, U. I.; Lee, E.; Yoo, I.; Nathan, A.; Lee, S.; Robertson, J.; Kim, K., Gated Three-Terminal Device Architecture to Eliminate Persistent Photoconductivity in Oxide Semiconductor Photosensor Arrays. *Nature Materials* **2012,** *11* (4), 301-305.

27. Kim, M. K.; Lee, J. S., Synergistic Improvement of Long-Term Plasticity in Photonic Synapses Using Ferroelectric Polarization in Hafnia-Based Oxide-Semiconductor Transistors. *Advanced Materials* **2020**, *32* (12), 1907826.

28. Yang, J. T.; Ge, C.; Du, J. Y.; Huang, H. Y.; He, M.; Wang, C.; Lu, H. B.; Yang, G. Z.; Jin, K. J., Artificial Synapses Emulated by an Electrolyte-Gated Tungsten-Oxide Transistor. *Advanced Materials* **2018**, *30*, 1801548.

29. Sun, J.; Oh, S.; Choi, Y.; Seo, S.; Oh, M. J.; Lee, M.; Lee, W. B.; Yoo, P. J.; Cho, J. H.; Park, J.-H., Optoelectronic Synapse Based on IGZO-Alkylated Graphene Oxide Hybrid Structure. *Advanced Functional Materials* **2018,** *28* (47), 1804397.

30. Zhu, L. Q.; Wan, C. J.; Guo, L. Q.; Shi, Y.; Wan, Q., Artificial Synapse Network on Inorganic Proton Conductor for Neuromorphic Systems. *Nature Communications* **2014,** *5*, 3158.

32. Zhou, Y.; Li, J.; Yang, Y.; Chen, Q.; Zhang, J., Artificial Synapse Emulated through Fully Aqueous Solution-Processed Low-Voltage In2O3 Thin-Film Transistor with Gd2O3 Solid Electrolyte. *ACS Applied Materials & Interfaces* **2020,** *12* (1), 980-988.

33. Chen, L.; Wang, L.; Peng, Y.; Feng, X.; Sarkar, S.; Li, S.; Li, B.; Liu, L.; Han, K.; Gong, X.; Chen, J.; Liu, Y.; Han, G.; Ang, K. W., A van der Waals Synaptic Transistor Based on Ferroelectric $Hf_{0.5}Zr_{0.5}O_2$ and 2D Tungsten Disulfide. *Advanced Electronic Materials* **2020,** *6* (6), 2000057.

34. Yang, C. S.; Shang, D. S.; Liu, N.; Shi, G.; Shen, X.; Yu, R. C.; Li, Y. Q.; Sun, Y., A Synaptic Transistor Based on Quasi-2D Molybdenum Oxide. *Advanced Materials*

2017, *29* (27), 1700906.

35. Bessonov, A. A.; Kirikova, M. N.; Petukhov, D. I.; Allen, M.; Ryhanen, T.; Bailey, M. J., Layered Memristive and Memcapacitive Switches for Printable Electronics. *Nature Materials* **2015,** *14* (2), 199-204.

36. Han, H.; Yu, H.; Wei, H.; Gong, J.; Xu, W., Recent Progress in Three-Terminal Artificial Synapses: From Device to System. *Small* **2019,** *15*, 1900695.

37. H.-L. Park, H. Kim, D. Lim, H. Zhou, Y.-H. Kim, Y. Lee, S. Park, T.-W. Lee, Retina-Inspired Carbon Nitride-Based Photonic Synapses for Selective Detection of UV Light. *Advanced Materials* **2020,** *32*, 1906899.

38. Wu, T.-L.; Huang, M.-J.; Lin, C.-C.; Huang, P.-Y.; Chou, T.-Y.; Chen-Cheng, R.-W.; Lin, H.-W.; Liu, R.-S.; Cheng, C.-H., Diboron Compound-Based Organic Light-Emitting Diodes with High Efficiency and Reduced Efficiency Roll-Off. *Nature Photonics* **2018,** *12* (4), 235-240.

39. Wu, Q.; Wang, J.; Cao, J.; Lu, C.; Yang, G.; Shi, X.; Chuai, X.; Gong, Y.; Su, Y.; Zhao, Y.; Lu, N.; Geng, D.; Wang, H.; Li, L.; Liu, M., Photoelectric Plasticity in Oxide Thin Film Transistors with Tunable Synaptic Functions. *Advanced Electronic Materials* **2018,** *4* (12), 1800556.

40. Lee, M.; Lee, W.; Choi, S.; Jo, J. W.; Kim, J.; Park, S. K.; Kim, Y. H., Brain-Inspired Photonic Neuromorphic Devices using Photodynamic Amorphous Oxide Semiconductors and their Persistent Photoconductivity. *Advanced Materials* **2017,** *29* (28), 1700951.

41. Di Lauro, M.; De Salvo, A.; Sebastianella, G. C.; Bianchi, M.; Carli, S.; Murgia, M.; Fadiga, L.; Biscarini, F., Tunable Short-Term Plasticity Response in Three-Terminal Organic Neuromorphic Devices. *ACS Applied Electronic Materials* **2020,** *2* (7), 1849-1854.

42. Yu, J.; Javaid, K.; Liang, L.; Wu, W.; Liang, Y.; Song, A.; Zhang, H.; Shi, W.;

Chang, T. C.; Cao, H., High-Performance Visible-Blind Ultraviolet Photodetector Based on IGZO TFT Coupled with p-n Heterojunction. *ACS Applied Materials & Interfaces* **2018,** *10* (9), 8102-8109.

43. Scholz, S.; Kondakov, D.; Lüssem, B.; Leo, K., Degradation Mechanisms and Reactions in Organic Light-Emitting Devices. *Chemical Reviews* **2015,** *115*, 8449–8503.

44. Bolton, O.; Lee, K.; Kim, H. J.; Lin, K. Y.; Kim, J., Activating Efficient Phosphorescence from Purely Organic Materials by Crystal Design. *Nature Chemistry* **2011,** *3* (3), 205-210.

45. Hirata, S.; Totani, K.; Zhang, J.; Yamashita, T.; Kaji, H.; Marder, S. R.; Watanabe, T.; Adachi, C., Efficient Persistent Room Temperature Phosphorescence in Organic Amorphous Materials under Ambient Conditions. *Advanced Functional Materials* **2013,** *23* (27), 3386-3397.

Chapter 5. Nano-Floating Gate Modulated LAOLETs

Organic light-emitting transistors (OLETs) are unique platforms for opto-electronics applications. Their dual functionality, combining in a single device the light generation characteristic of light-emitting diodes with the current modulation and signal amplification of field-effect transistors, renders them particularly appealing for the development of the next generation of active-matrix displays.[1–4] Optically responsive memory OLETs, based on photochromic molecules or metal oxide with persistent photoconduction characteristics, have demonstrated significant potential for smart display technologies.[5] However, these memory OLETs exhibit a major limitation: the memory current driving the light-emission could be modulated solely by the optical stimulus. Hence such devices do not fulfill the technological requirements for smart displays which should be endowed with responsiveness to distinct bionic stimuli. To broaden the control over the device operation, thereby enabling functional diversification, electric spiked memory transistors could offer a versatile solution when coupled with sensors, by collecting external physical or chemical stimuli and converting them into electrical inputs for data storage. The sensory data for intelligent bionic system could be thus encoded by employing different types of stimuli, whose precision and reliability for technological applications have been already demonstrated through the fabrication of tactile sensors,[6–9] light sensors,[10–12] humidity sensors,[13, 14] and chemical sensor.[15–17] As an alternative to conventional three-terminal memory architectures, nano-floating gate transistors (NFGTs) are particularly suitable for the realization of both volatile and non-volatile memory devices, since they combine a well-established working mechanism, reliable memory operations, and a gigantic memory capacity.[18–21] Recently, artificial synaptic devices based on NFGTs have been exploited to mimic synaptic learning rules in human brain including short-term potentiation (STP) to long-term potentiation (LTP) transition, and spike-timing-dependent plasticity (STDP), empowering the development of neuromorphic computing hardware.[22, 23]

On the other hand, materials and processing optimization in organic optoelectronics enabled the controlled manufacturing of homogenous large-area thin-films deposited with cost-efficient and scalable liquid-based processing technologies such as spray- and blade-coating as well as ink-jet and 3D printing.[24–29] Nevertheless, the step-wise assembly of superimposed multiple layers by mastering solution processing protocols requires the use of orthogonal solvents for the deposition of successive layers.[30,31] While alcohol-soluble N-type polymers have been integrated as electron transport layer in solution-processed hybrid OLETs,[32,33] the use of alcohol-soluble hole transport/extraction polymers in high-performance organic optoelectronics still needs to be fully demonstrated,[34,35] hitherto limiting their application in solution-processed P-type hybrid multilayer OLET architectures.[36–38]

In this chapter, we present full-color, nano-floating gate (NFG) modulated LAOLETs whose “soft components” are all deposited by spin-coating. The layout comprises superimposed layers of water dispersed gold nanoparticles (Au NPs) as floating gate and methyl glycol processed Al_2O_3 thin film as tunneling barrier, covered sequentially by a channel layer, a hole transport layer, a light-emitting layer and an electron transport layer which are deposited from solutions in hot dichlorobenzene, chlorobenzene, toluene and methanol, respectively. Significantly, after applying positive gate spike as presynaptic stimulus, long afterglow electroluminescence with synaptic function of STP to LTP transition and STDP was observed. Conversely, upon applying a negative gate spike as signal input, immediate sparked electroluminescence was recorded. The time-dependent characterization revealed that two different targeted operating modes of retardation display and real-time display can be achieved in a single device. Hence, reconfigurable displays can be realized by the selecting polarity of gate voltage.

5.1. Experimental Method

Gold nanoparticles solution, octylphosphonic acid, green light-emitting spiro-

copolymer (SpiroG), poly(2-methoxy-5-(3′,7′-dimethyloctyloxy)-1,4-phenylenevinylene) (MDMO-PPV), poly(9,9-dioctylfluorene-alt-bithiophene) (F8T2), and poly(9,9-dioctylfluorene-co-bis-N,N-(4-butylphenyl)-bis-N,N-phenyl-1,4-phenylenediamine) (PFB) were purchased from Sigma-Aldrich. PFNOX was purchased from Lumtec. DPPDTT (M_W > 100K) and PTPD (M_W ~ 80K) were purchased from 1-Materials. All the materials were used as received, without any further purification.

Preparation of AlO_x Precursor Solution. $Al(NO_3)_3 \cdot 9H_2O$ was dissolved in 2-methoxyethanol at concentration at 0.1 M, and stirred at room temperature overnight.

Preparation of DPPDTT Solution. 40 mg DPPDTT were dissolved in 10 mL dichlorobenzene, and then stirred at 80 °C overnight. The solutions were heated at 150 °C for 30 min before being spin-coated.

Preparation of PTPD Solution. 60 mg PTPD were dissolved in 10 mL chlorobenzene, and then stirred at 80 °C overnight.

Preparation of Light-Emitting Polymers Solution. 80 mg SpiroG, MDMO-PPV, F8T2 and PFB were dissolved in 10 mL toluene, and then stirred at 80 °C overnight.

Preparation of PFNOX Solution. 10 mg PFNOX were dissolved in 5 mL methanol and 50 μL acetic acid and then stirred at 80 °C overnight.

Devices were fabricated on the substrates of n^{++} Si as bottom gate coated with 230 nm of thermally grown SiO_2 as the gate dielectric (IPMS Fraunhofer Institute). The Si/SiO_2 substrates were cleaned with water, acetone, and alcohol in sequence and dried under N_2 flow. The cleaned substrates were further treated with UV-ozone for 20 min. Au NPs solution was spin-coated at 800 rpm for 2 min on the silicon wafer followed with 0.1 M Al_2O_3 precursor solution spinning coated at 3000 rpm for 45 s. Subsequently, the substrate was dried at 150 °C for 5 min and baked at 360 °C for 30 min. The substrates were soaked in 0.05 M octylphosphonic acid solution overnight before being

used. A channel layer with thickness of 50 nm were spin-coated on substrates from hot DPPDTT solution.

For NFGTs: Interdigitated Au electrodes (40 nm) were deposited on the DPPDTT film through shadow masks. Floating gate synaptic transistors comprising a DPPDTT channel layer as active material were fabricated by using a bottom-gate, top-contact geometry to investigate the synaptic behavior (Figure 5-1a). A stabilized suspension of 5 nm sized Au NPs in citrate buffer solution was spin-coated onto a Si/SiO_2 wafer to act as NFG. Successively, an Al_2O_3 tunneling layer with thickness of ~10 nm was spun from the Al_2O_3 precursor solution. The atomic force microscopy (AFM) images in Figure 5-1b and 5-1c confirms the relatively uniform microscale morphology of the Au NPs film after Al_2O_3 deposition. The space confinement of the Au NPs in-between the two dielectric layers (SiO_2 and Al_2O_3 based) is expected to provide presynaptic weight tuning.

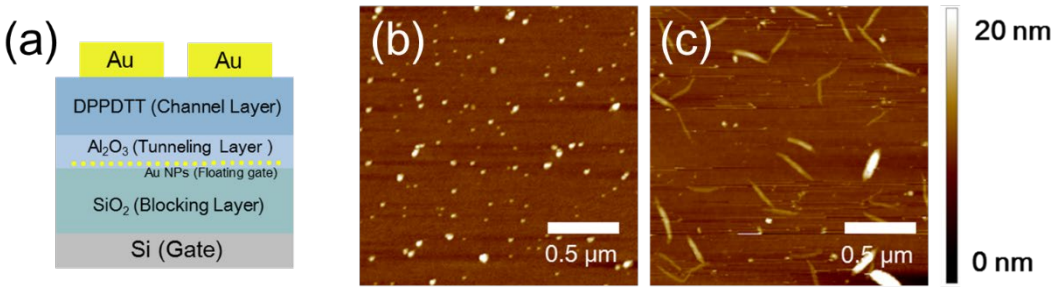

Figure 5-1. (a) Scheme of the multilayered NFGTs device. Atomic force microscopy (AFM) topographical images of Au NPs (b) before and (c) after Al_2O_3 thin film coverage. Z-scales = 20 nm.

For LAOLETs: Source electrode (Au, 50 nm) was evaporated on the DPPDTT film through shadow masks. Subsequently, hole transport layer with thickness of 10 nm was spun from PTPD solution, followed by a thermal annealing at 150 °C for 20 min. Light emitting layer of different color with thickness of 45 nm was spun from corresponding emitting solution, followed by thermal annealing at 130 °C for 20 min. Electron

transport layer with thickness of 10 nm was spun from PFNOX solution, followed by a thermal annealing at 130 °C for 20 min. Finally, the drain electrode (Au, 35 nm) was deposited through shadow masks. The device architecture is portrayed in Figure 5-2a. The width (W) and length (L) of the channel in LAOLETs amount to 27 mm and 200 μm, respectively, whereas the emission area was defined as 4.22 mm^2. The emission of different colors (green, red, yellow and blue) was obtained by using four commercial semiconducting light-emitting polymers, *i.e.* the green SpiroG, the red MDMO-PPV, the yellow F8T2, and the blue PFB. The chemical structure of the polymers is reported in Figure 5-2b.

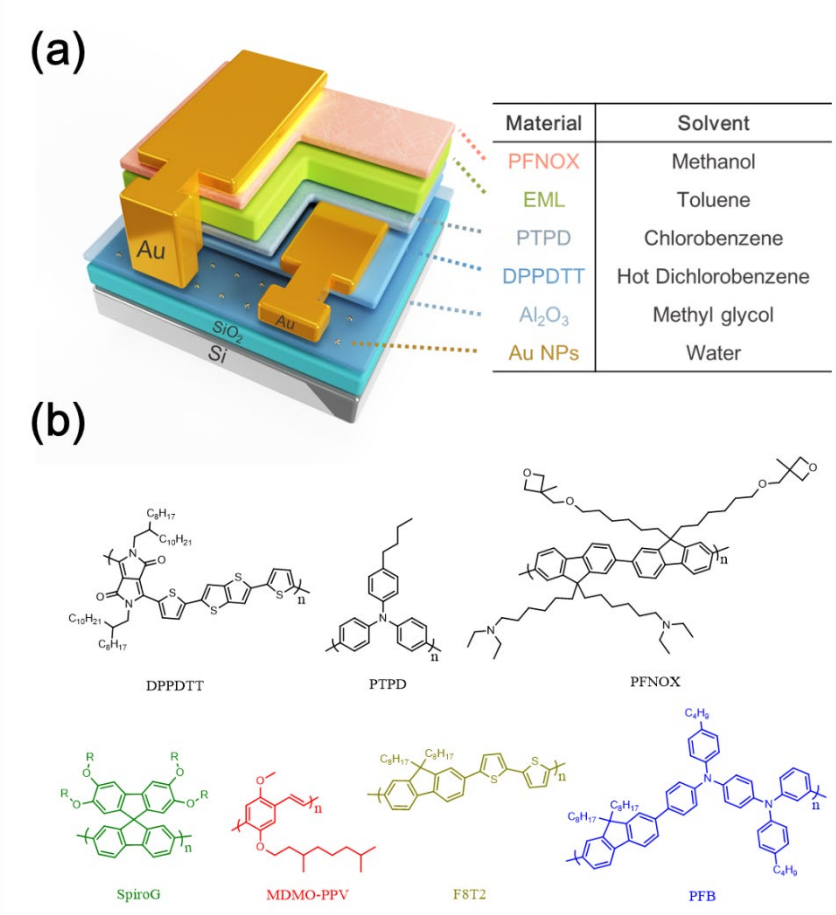

Figure 5-2. Schematic images of device structure and chemical structures. (a) Aerial view Device structure of LAOLETs. (b) Corresponding schematic cross section (front view) of LAOLETs. (c) Schematic demonstrating the reconfigurable displays (d)

Chemical structures of DPPDTT, PTPD, PFNOX, and the four EMLs, *i.e.* SpiroG, MDMO-PPV, F8T2 and PFB.

The optical images of the devices are displayed in Figure 5-3a. Aiming at superimposing via solution processing four layers of different functionalized polymers, we have selected three conjugate polymers soluble in non-polar solvents with specific order of solvent dissolvability, being specifically hot dichlorobenzene, chlorobenzene and toluene respectively, followed by the deposition of a final alcohol-soluble N-type polymer. AFM imaging of 2×2 μm^2 regions of these films before and after soaking of the solvent from upper layer was used to evaluate the quality of the layer-by-layer interface (Figure 5-3b to 5-3g). The morphology of DPPDTT films before and after chlorobenzene soaking exhibited relatively smooth surface with a root-square-mean roughness (R_{RMS}) of about 1.1 nm. Differently, the morphology of PTPD film after-soaking showed a slightly higher R_{RMS} of about 0.5 nm, when compared with its pristine film (with a R_{RMS} of about 0.2 nm), still confirming the ultra-smooth nature of the interface between HTL and EML. Expectedly, the R_{RMS} of SpiroG film remained 0.2 nm after methanol soaking. The sharp interface between individual layers in the stack can be also observed from cross-section scanning electron microscopy (SEM) imaging of the G-LAOLETs (Figure 5-3h), providing further confirmation of the viability of the employed process for the controlled deposition of four stacked polymers layer. The thickness of films was determined from such SEM images and confirmed by profilometry (Figure 5-3i).

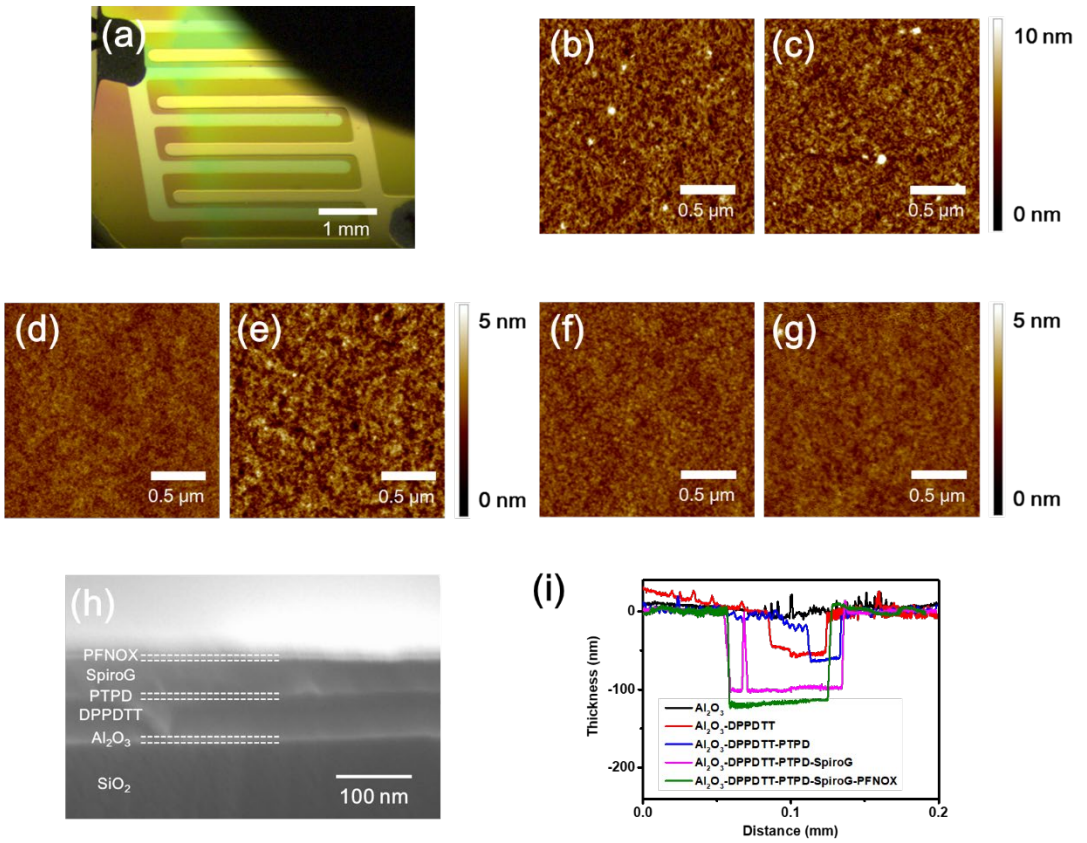

Figure 5-3. (a) Optical image of LAOLETs under light. AFM topographical images of DPPDTT thin film (b) before and (c) after chlorobenzene soaking. Z-scales = 10 nm. AFM topographical images of PTPD thin film (d) before and (e) after toluene soaking. Z-scales = 5 nm. AFM topographical images of SpiroG thin film (f) before and (g) after methanol soaking. Z-scales = 5 nm. (h) Cross-section SEM image of G-LAOLETs. (i) Profilometer results for emulating the thickness of Al_2O_3, DPPDTT, PTPD, SpiroG and PFNOX as 10 nm, 50 nm, 10 nm, 45 nm and 10 nm, respectively, consistently with the results obtained through the cross-section SEM analysis.

Devices were characterized in a dry and nitrogen-filled glove-box. The electrical characteristics and basic synaptic functions were measured by a semiconductor parameter analyzer (Keithley 2636). Irradiation intensity of device were measured by a photodiode (HAMAMATSU S3204-08) which have been previously calibrated by a luminance meter (KONICA MINOLTA, LS-100). Electroluminescence spectrum of

OLETs were measured by Ocean Optics FLAME-S. AFM images were recorded with a Bruker Dimension Icon set-up operating under ambient conditions, in tapping mode. SEM images were taken with Quanta FEG 250 from FEI Company. The thickness of films was determined by the Alpha-Sep IQ Surface Profiler.

5.2. Synaptic Transistors Based on Floating Gate Architecture

The gate-source voltage (V_G) and the drain-source voltage (V_D) of NFGTs can be conceived as the pre- and post-synaptic terminals, respectively. The transfer curves of NFGTs under a variety of different ranges of V_G scanning conditions are displayed in Figure 5-4a. As marked by the arrows, the V_G sweeping direction started from positive to negative (backward sweep direction), and then reversed to positive (forward sweep direction), resulting in a counterclockwise hysteresis. The NFGTs exhibited a predominant P-type behavior with a hole mobility of ca. 0.5 $cm^2 V^{-1} s^{-1}$. Typically, two distinct states were observed at two sweeping directions when the applied sweeping voltage exceeds ±40 V, revealing a negatively shifted threshold voltage (V_{Th}) in the backward sweep. Upon gradual expansion of the sweep range, the memory window of the devices, defined as the shifted V_{Th} (ΔV_{Th}), increased significantly. Maximum ΔV_{Th} with value of 45 V was obtained after applying ±100 V to the gate. The transfer curves of NFGTs without Au NPs are plotted in Figure 5-4b for comparison Despite the existence of natural traps in the SiO_2 and Al_2O_3 which could lead the hysteresis in the transfer curves, the NFGTs without Au NPs exhibit a lower memory window (ΔV_{Th}) of 20 V when compared with the 45 V observed when NFGTs comprises Au NPs.

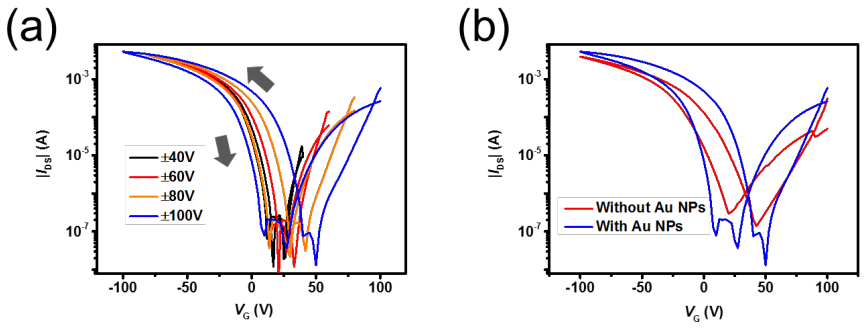

Figure 5-4. (a) Transfer hysteresis curves of NFGTs under difference V_G sweeping range. (b)Transfer curves of NFGTs with and without Au NPs.

This ΔV_{Th} can be exploited for writing/erasing operations in functional devices, whose working mechanism is displayed in Figure 5-5a and 5-5b. When a suitable positive gate bias (> 40 V) was applied to the gate terminal, electrons accumulated at the interface between the tunneling (Al_2O_3) layer and the channel layer, and some among them tunneled through the Al_2O_3 layer to be injected into Au NPs. These electrons were stored even after the removal of V_G because of the barrier provided by the Al_2O_3 layer, leading to an increased drain-source current (I_{DS}) due to the enhanced channel conductance. Conversely, when a negative gate bias was applied, the opposite process was achieved, resulting in an "erasing" action.[39, 40]

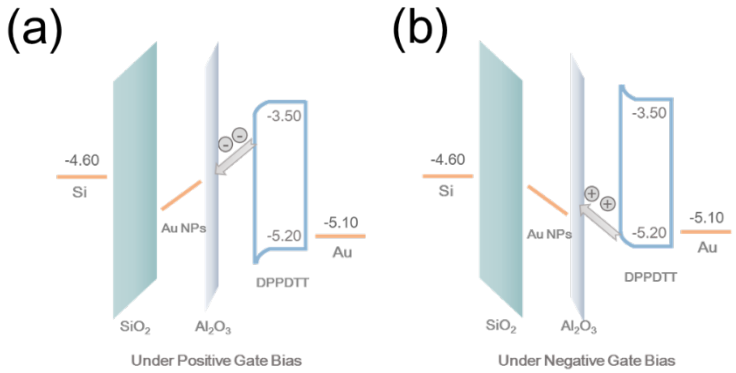

Figure 5-5. Schematic energy-band diagrams and charge flow of the NFGTs device during (a) writing and (b) erasing operation.

By exploiting this floating-gate effect, biological synaptic functions were emulated upon applying $V_D = -60$ V combined with 8 stimulus V_G pulses. The writing and erasing operations can be reversibly controlled by the polarity of the gate bias, as plotted in Figure 5-6a and 5-6b, respectively. The excitatory postsynaptic current (PSC, measured as I_{DS}) could be triggered by applying a positive V_G stimulus (100 V, 12 s). Once the stimulus was ceased, the PSC raised to approximately 0.3 mA. Logically, one of most

important neuronal functions is the STP to LTP transition, which was observed after applying in-series an increased number of stimuli, from one to eight, thereby enhancing the intensity of PSC from 0.3 mA to 0.6 mA. Another key synaptic function in neuromorphic systems is represented by the changes in the synaptic weight modulated by the spike timing to master STDP. The PSC response to one stimulus having a width ranging from 6 s to 24 s (Figure 5-6c and 5-6d) clearly show that a longer stimulus width resulted in greater PSC values with longer retention time. In addition, the erasing of PSC in synaptic device could also be mimicked. A typical erasing current at amplitude of 0.1 μA could be triggered by a negative V_G spike (−100 V, 12 s), providing a superior writing/erasing current ratio ($I_{W/E}$) of 10^3 (Figure 5-6e). Apart from postsynaptic depression, there is an increasing current > 1 mA as a result of each negative V_G spike, revealing the "on-state" of the devices. Starting from the third negative V_G spike, such an on-state current maintained an amplitude of 2.5 mA, because of the charge saturation absorption of Au NPs, offering a mean to power light emission. The results of such real-time writing/erasing process provide unambiguous evidence that, NGFTs can be turned on both "after positive gate voltage" and "under negative gate voltage".

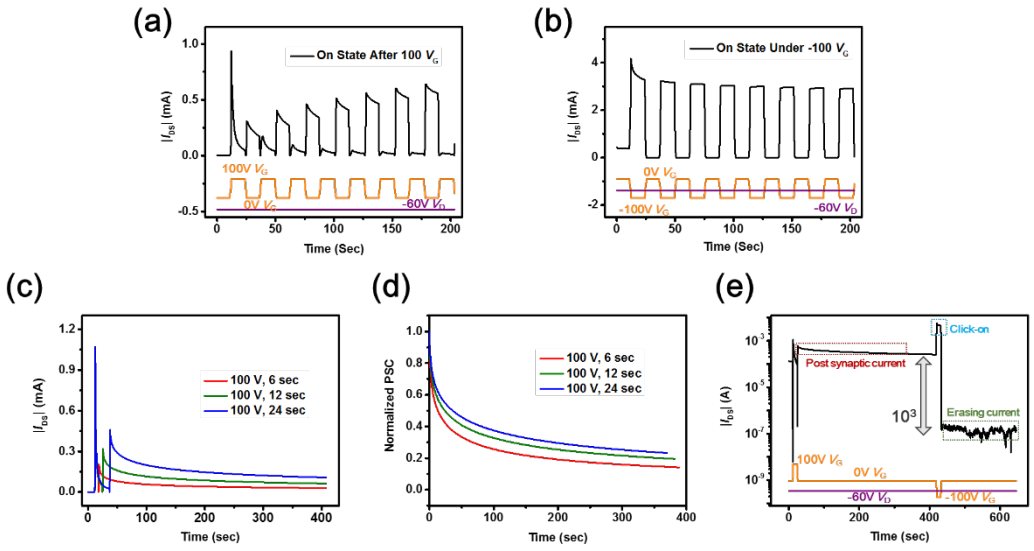

Figure 5-6. Time dependence measurement of devices with eight positive and negative

VG spiked as (a) writing and (b) erasing operation, respectively. Orange and purple line represent the real-time V_G and V_D, respectively. (c) Time-resolved decay curves and (d) corresponding normalized curves of PSC after applying V_G = 100 V with different stimulus width. (e) I_{DS} expressed in log-scale after having applied once a positive and a negative gate.

5.3. Long Afterglow OLETs Based on Floating Gate Architecture

To impart a synaptic function to light-emitting devices, green emitting long afterglow OLETs (G-LAOLETs) were fabricated and characterized by utilizing SpiroG as light-emitting material. The energy levels of the polymers forming the multilayer structure and the working mechanism, including memory and display processes, are illustrated in Figure 5-7a and 5-7b. As previously explained, when a suitable presynaptic voltage is applied to the gate terminal, electrons accumulating at interface between the tunneling layer and the channel layer can be injected into NFG and are stored, resulting in enhancement of the conductance of DPPDTT when the voltage stimulus is ceased. Predictably, an enhancement of the conductance of DPPDTT can be also attained upon applying a negative gate bias. Yet, for the light emission operation, a negative drain bias needs to be also applied. Hole carriers are injected from the source electrode to the channel layer and then transported to PTPD, while electron carriers are injected from drain electrode to the PFNOX, leading to the hole-electron carriers recombination in the light-emitting polymer and forming a uniform drain-shaped region of emission.

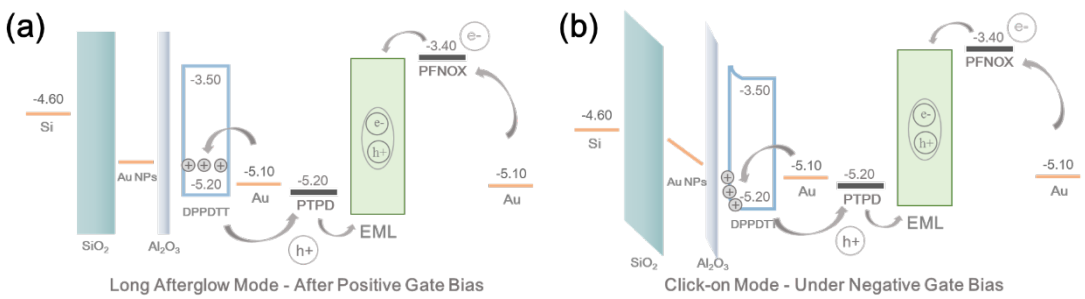

Figure 5-7. LAOLET's working mechanisms: (a) long afterglow mode, (b) click-on mode.

Electrical combined optical hysteresis transfer curves and optical output curves of G-LAOLETs are displayed in Figure 5-8a and 5-8b/c, respectively. The maximum current and brightness of G-LAOLETs reached 3 mA and 2500 cd m^{-2} when $V_D = -60$ V and $V_G = -100$ V were applied. A saturation hole field-effect mobility of 0.25 cm^2 V^{-1} s^{-1}, and an I_{on}/I_{off} ratio of 10^5 were also obtained. To demonstrate the reproductively of these devices, transfer curves of 10 G-LAOLETs from five batches are plotted in Figure 5-8d. Similar to the NFGTs, the NFG driven memory behavior was also observed in the G-LAOLETs, as evidenced by two distinct states in two sweeping directions. In backward sweep direction, V_{Th} of devices was set at −2 V and light turn-on voltage (V_{on}) at 1 V, whereas in the forward sweep direction, V_{Th} and V_{on} were set at −41 V and −40 V, respectively. Both current and brightness memory window (ΔV_{Th} and ΔV_{on}) are calculated as ~ 40 V, allowing the devices to operate as memory displays.

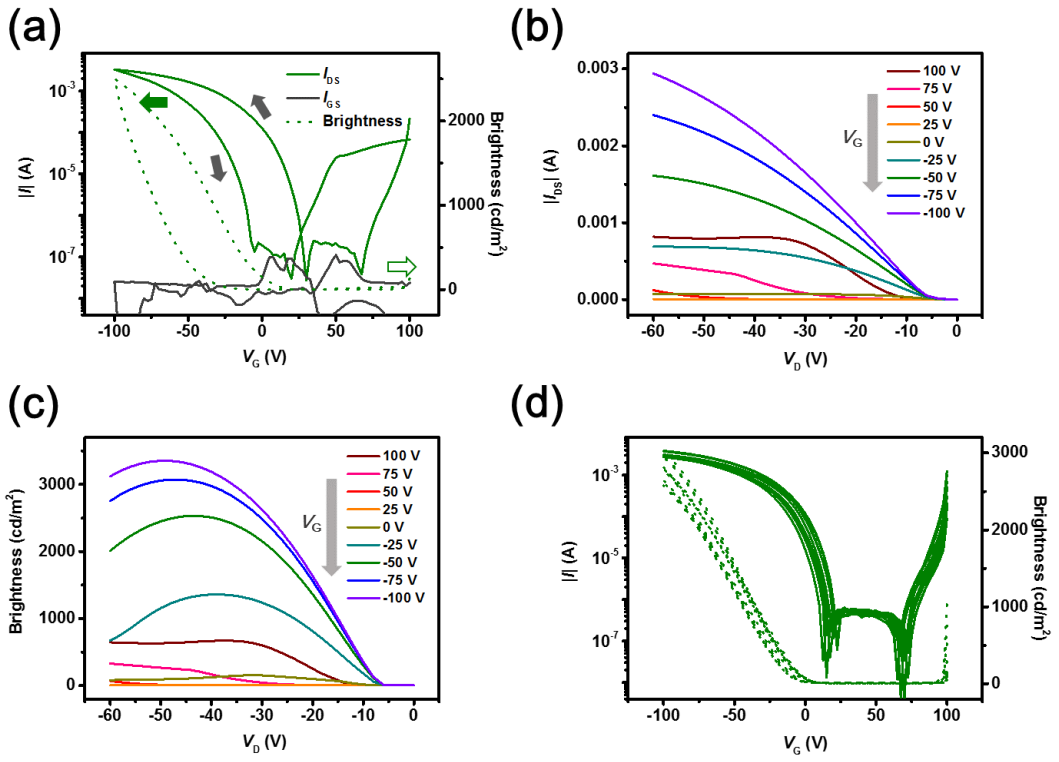

Figure 5-8. (a) Electric and optical transfer curves of G-LAOLETs. The solid line represents the electric curves while dot line represents the brightness curves. (b) Electrical output curves of G-LAOLET. (c) Electrical output curves of G-LAOLET. The applied gate voltage were scanned from 100 V to –100V. (d) Electrical and optical transfer curves of ten G-LAOLETs from five batches. The error of maximum current, maximum brightness, V_{Th} and V_{on} of these devices are ~ ±10%.

To further elucidate the memory display properties of G-LAOLETs, electric time dependence measurements of device's intergraded brightness under V_D = −60 V upon varying V_G were carried out and displayed in Figure 5-9a and 5-9b. Not surprisingly, exploiting the memory current to power the memory display, the device's postsynaptic brightness (PSB) featured a trend similar to the PSC in both writing/erasing operations. Analogous to the long afterglow phenomenon which have attracted quite some interests for applications in optical data storage, in-vivo imaging and anti-counterfeiting (42, 43), this time-resolved decay behavior of PSB can be exploited to achieve similar device functions, working as "long afterglow mode". Initially, the device's PSC was about 4 μA, being too low to drive the light emission. Once a positive spike (V_G = 100 V, 12 s) stimulus finished, the PSC and PSB became measurable and were found to amount to 0.12 mA and 81 cd m^{-2}, respectively. Since DPPDTT is an ambipolar semiconductor with narrow bandgap, when a positive V_G is applied, hole carrier can inject from source electrode to the LUMO level of DPPDTT. For practical applications, this current peak can be inhibited by exploiting wide bandgap polymer as channel material. After repeating these spikes eight times, the PSC and PSB have grown reaching 0.24 mA and 142 cd m^{-2}, hence demonstrating that a greater current and light emission could be simultaneously reached by repeating the signal input, also indicating the lifetime of this long afterglow emission is limited by the lifetime of PSC. The mechanism ruling this process consisted in the step-wise enhancement of the amount of electrons being trapped into the NFG upon increasing the number of spikes. Figure 5-9c shows the PSC

and PSB response to a single stimulus having a width ranging from 6 s to 24 s. According to the fitting (Figure 5-9d), after having applied a stimulus of V_G = 100 V for 6 sec, a L_0 of 18 cd m^{-2} with a lifetime (τ_l) of 12.8 sec was obtained. Upon gradual increase of the stimulus width to 12 sec and 24 sec, enhanced L_0 to 60 cd m^{-2} and 127 cd m^{-2} with prolonged τl to 14.1 sec and 17.2 sec of PSB were observed. On the other hand, PSC and PSB of devices can be inhibited by one negative spike (V_G = −100 V, 12 s), decreasing to 0.1 μA and 0 cd m^{-2}, hence revealing an $I_{W/E}$ of 10^3. Apparently, the current intensity of > 1 mA under each negative V_D spikes could drive the light emission in the devices, defining another work mode as "click-on". According to the time-dependence measurements shown in Figure 5-9e, although the current exhibited a slight decay upon applying a negative gate voltage, a stable on-state current of ~ 1 mA accompanied with stable brightness of ~ 300 cd m^{-2} was observed after 150 sec of continuous application of a negative V_G, due to the nearly saturated absorption of NFG. These results provide evidence that two different display operating modes, *i.e.* "long afterglow" and "click-on", can be achieved simultaneously in the same display unit by employing positive gate voltage and negative gate voltage spike, respectively.

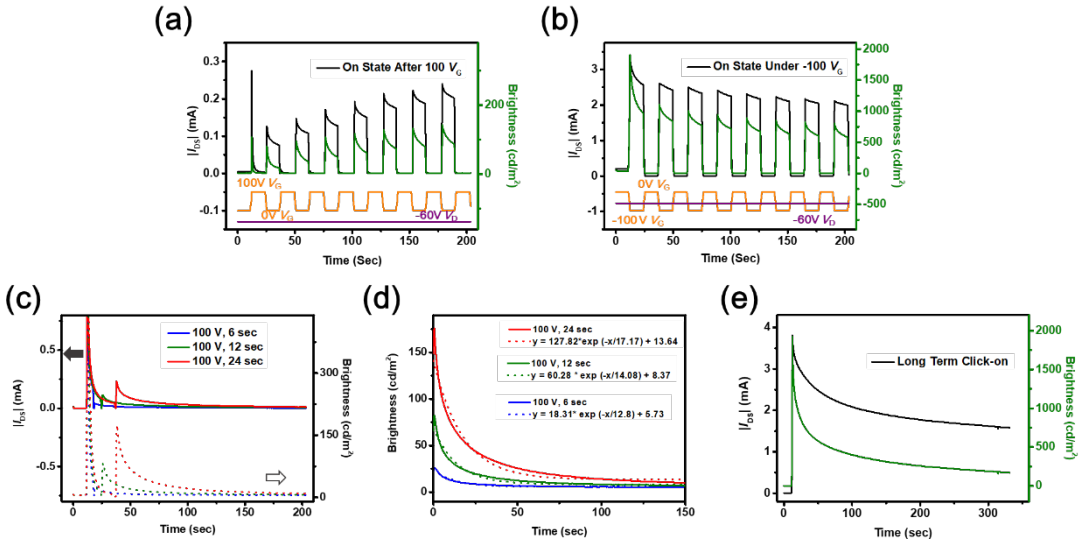

Figure 5-9. (a) Long afterglow mode and (b) click-on mode, respectively. Orange and purple lines represent the real-time gate and drain voltage, respectively. (c) Time-

resolved electrical and optical decay curves of G-LAOLETs after the application of V_G = 100 V with different stimulus width. (d) Optical decay curves included fitting line of PSB after application of V_G = 100 V with different stimulus width. Electroluminescence lifetime (τl) of G-LAOLETs can be also determined from the time-resolved decay of the luminescent intensity as described by the exponential decay equation: $L(t) = L_0 \times \exp(-t/\tau_l) + L_\infty$, where L_0 is the initial fluorescence strength at starting time (t = 0) (e) Stabilized measurement of G-LAOLETs when negative V_G was applied continuously.

Devices capable to emit light with three different colors were fabricated by employing different light-emitting polymers as active components. In particularly, we used MDMO-PPV for red (R-LAOLET), F8T2 for yellow (Y-LAOLET) and PFB for blue (B-LAOLET). Electric and optical hysteresis transfer curves of red, yellow and blue LAOLETs are measured (Figure 5-10a to 5-10c). All these devices exhibited a maximum current of around 3 mA and an I_{on}/I_{off} ratios reaching 10^5. Upon applying V_G = −100 V and V_D = −60 V to the LAOLETs, we observed maximum brightness values of 493 cd m^{-2}, 1666 cd m^{-2} and 66 cd m^{-2}, for red, yellow and blue light-emitting devices, respectively. On the same time, all these LAOLETs exhibited approximately ΔV_{Th} and ΔV_{on} of ~30 V and $I_{W/E}$ of ~10^4, indicating that the synaptic behavior was retained regardless of the employed light-emitting polymers. The electroluminescence peaks of the red, yellow, blue and green LAOLETs were located at 603 nm, 550 nm, 450 nm and 542 nm, respectively (Figure 5-10d).

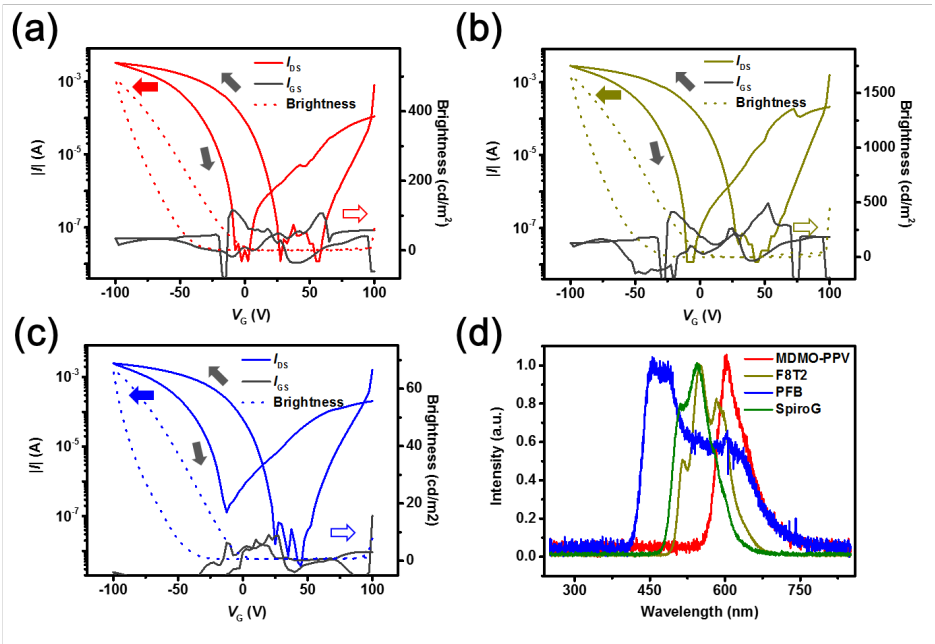

Figure 5-10. Electrical and optical characterization of full-color LAOLETs. Electrical and optical transfer curves of (a) R-LAOLET, (b) Y-LAOLET and (c) B-LAOLET. The solid and dot lines represent the electric and the brightness curves, respectively. (d) Electroluminescence spectra of LAOLETs incorporating MDMO-PPV, F8T2, PFB and SpiroG.

To further evaluate influence of light-emitting material on the memory display properties, electric and optical time dependence measurements of full-color LAOLETs under $V_D = -60$ V upon varying V_G were carried out and displayed in Figure 5-11a to 5-11f. It is clear that two different work modes were realized successfully whatever the light-emitting materials using. These results demonstrate that LAOLETs with optimized color emission could be achieved by simply selecting the ideal light-emitting materials.

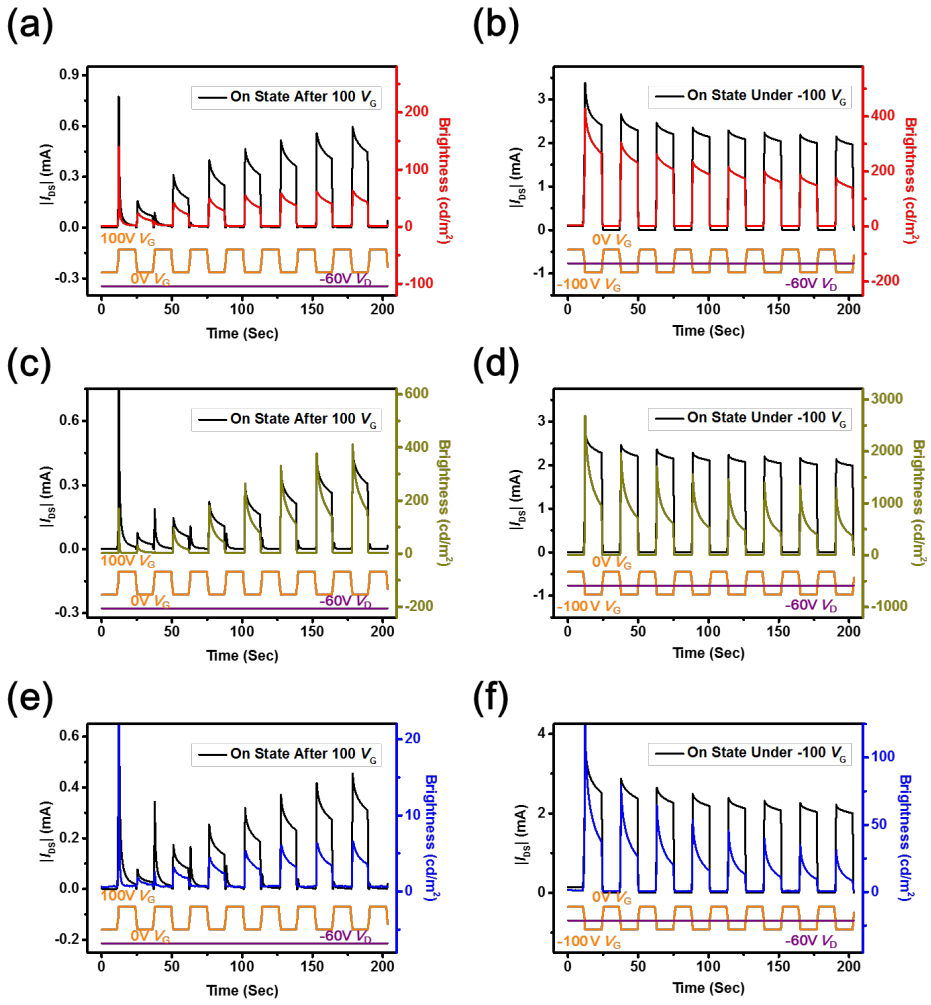

Figure 5-11. Time dependence electric and optical measurement of R-, Y-, B-LAOLETs with eight positive and negative gate spiked employed as (a, c. e) long afterglow mode and (b, d, f) click-on mode, respectively. Orange and purple lines represent the real-time gate and drain voltage, respectively.

The optical images of the devices including the initial state and the two working modes in the dark of G-LAOLETs are presented in Figure 5-12a. The optical images of full-color LAOLETs are also displayed in Figure 5-12b.

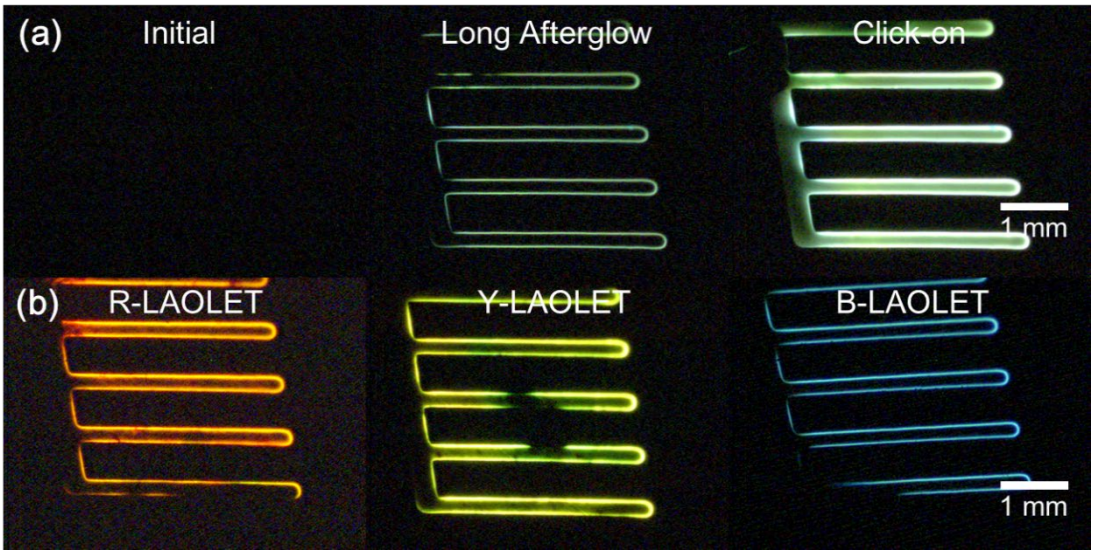

Figure 5-12. (a) Optical image of LAOLETs under same V_D = −60 V and different VG conditions: initial state of device, under dark and V_G = 0; long afterglow mode, after 20 sec spiked V_G = 100 V; and click-on mode, under spiked V_G = −100 V. (b) Optical images of R-, Y-, and B-LAOLETs when −60 V V_D and V_G = −100 V was applied.

5.4. Conclusions

In summary, in this chapter, electrical spiked LAOLET have been realized. Importantly, the "soft components" in these LAOLETs were all processed by spin-coating. Six superimposed functional layers, with sharp interfaces among them, supported on a Si/SiO_2 wafer, were stacked. Being based on a nano-floating gate architecture, these LAOLETs can work in two different operating modes: “long afterglow” and “click-on”. For “long afterglow”, after applying positive gate spike as presynaptic stimulus, long afterglow display could be attained. This brightness and lifetime of long-lasting emission can be enhanced and prolonged by repeating the stimulus and increasing stimulus width, respectively. For “click-on”, a prompt light-emission under each negative gate spiked was observed in the same device.

5.5. Reference

1. Wu, Z.; Liu, Y.; Guo, E.; Darbandy, G.; Wang, S. J.; Hubner, R.; Kloes, A.; Kleemann, H.; Leo, K., Efficient and Low-Voltage Vertical Organic Permeable Base Light-Emitting Transistors. *Nature Materials* **2021,** *20* (7), 1007-1014.

2. McCarthy, M. A.; Liu, B.; Donoghue, E. P.; Kravchenko, I.; Kim, D. Y.; So, F.; Rinzler, A. G., Low-Voltage, Low-Power, Organic Light-Emitting Transistors for Active Matrix Displays. *Science* **2011,** *232*, 570-573.

3. Capelli, R.; Toffanin, S.; Generali, G.; Usta, H.; Facchetti, A.; Muccini, M., Organic Light-Emitting Transistors with An Efficiency that Outperforms the Equivalent Light-Emitting Diodes. *Nature Materials* **2010,** *9* (6), 496-503.

4. Chaudhry, M. U.; Muhieddine, K.; Wawrzinek, R.; Sobus, J.; Tandy, K.; Lo, S. C.; Namdas, E. B., Organic Light-Emitting Transistors: Advances and Perspectives. *Advanced Functional Materials* **2019,** *30* (20), 1905282.

5. Hou, L.; Zhang, X.; Cotella, G. F.; Carnicella, G.; Herder, M.; Schmidt, B. M.; Patzel, M.; Hecht, S.; Cacialli, F.; Samorì, P., Optically Switchable Organic Light-Emitting Transistors. *Nature Nanotechnology* **2019,** *14* (4), 347-353.

6. Wang, S.; Xu, J.; Wang, W.; Wang, G. N.; Rastak, R.; Molina-Lopez, F.; Chung, J. W.; Niu, S.; Feig, V. R.; Lopez, J.; Lei, T.; Kwon, S. K.; Kim, Y.; Foudeh, A. M.; Ehrlich, A.; Gasperini, A.; Yun, Y.; Murmann, B.; Tok, J. B.; Bao, Z., Skin Electronics from Scalable Fabrication of An Intrinsically Stretchable Transistor Array. *Nature* **2018,** *555* (7694), 83-88.

7. Ma, Y.; Liu, N.; Li, L.; Hu, X.; Zou, Z.; Wang, J.; Luo, S.; Gao, Y., A Highly Flexible and Sensitive Piezoresistive Sensor Based on MXene with Greatly Changed Interlayer Distances. *Nature Communications* **2017,** *8*, 1207.

8. Yamada, T.; Hayamizu, Y.; Yamamoto, Y.; Yomogida, Y.; Izadi-Najafabadi, A.;

Futaba, D. N.; Hata, K., A Stretchable Carbon Nanotube Strain Sensor for Human-Motion Detection. *Nature Nanotechnology* **2011,** *6*, 296-301.

9. Lee, S.; Reuveny, A.; Reeder, J.; Lee, S.; Jin, H.; Liu, Q.; Yokota, T.; Sekitani, T.; Isoyama, T.; Abe, Y.; Suo, Z.; Someya, T., A Transparent Bending-Insensitive Pressure Sensor. *Nature Nanotechnology* **2016,** *11*, 472-478.

10. Zhu, Q. B.; Li, B.; Yang, D. D.; Liu, C.; Feng, S.; Chen, M. L.; Sun, Y.; Tian, Y. N.; Su, X.; Wang, X. M.; Qiu, S.; Li, Q. W.; Li, X. M.; Zeng, H. B.; Cheng, H. M.; Sun, D. M., A Flexible Ultrasensitive Optoelectronic Sensor Array for Neuromorphic Vision Systems. *Nature Communications* **2021,** *12* (1), 1798.

11. Yao, Y.; Ou, Q.; Wang, K.; Peng, H.; Fang, F.; Shi, Y.; Wang, Y.; Asperilla, D. I.; Shuai, Z.; Samorì, P., Supramolecular Engineering of Charge Transfer in Wide Bandgap Organic Semiconductors with Enhanced Visible-to-NIR Photoresponse. *Nature Communications* **2021,** *12* (1), 3667.

12. Lee, Y.; Oh, J. Y.; Xu, W.; Kim, O.; Kim, T. R.; Kang, J.; Kim, Y.; Son, D.; Tok, J. B.-H.; Park, M. J.; Bao, Z.; Lee, T.-W., Stretchable Organic Optoelectronic Sensorimotor Synapse. *Science Advances* **2018,** *4*, eaat7387.

13. Chen, W. Y.; Jiang, X.; Lai, S. N.; Peroulis, D.; Stanciu, L., Nanohybrids of a MXene and Transition Metal Dichalcogenide for Selective Detection of Volatile Organic Compounds. *Nature Communications* **2020,** *11* (1), 1302.

14. Turetta, N.; Stoeckel, M.-A.; Oliveira, R. F.; Devaux, F.; Greco, A.; Cendra, C.; Gullace, S.; Gicevičius, M.; Chattopadhyay, B.; Liu, J.; Schweicher, G.; Sirringhaus, H.; Salleo, A.; Bonn, M.; Backus, E. H. G.; Geerts, Y. H.; Samorì, P., High-Performance Humidity Sensing in Pi-conjugated Molecular Assemblies through the Engineering of Electron/Proton Transport and Device Interfaces. *Journal of the American Chemical Society* **2022,** *144*, 2546-2555.

15. Cicoira, F.; Sessolo, M.; Yaghmazadeh, O.; DeFranco, J. A.; Yang, S. Y.; Malliaras,

G. G., Influence of Device Geometry on Sensor Characteristics of Planar Organic Electrochemical Transistors. *Advanced Materials* **2010,** *22* (9), 1012-1016.

16. Escobedo, P.; Fernández-Ramos, M. D.; López-Ruiz, N.; Moyano-Rodríguez, O.; Martínez-Olmos, A.; Pérez de Vargas-Sansalvador, I. M.; Carvajal, M. A.; Capitán-Vallvey, L. F.; Palma, A. J., Smart Facemask for Wireless CO_2 Monitoring. *Nature Communications* **2022,** *13*, 72.

17. Song, Y.; Min, J.; Yu, Y.; Wang, H.; Yang, Y.; Zhang, H.; Gao, W., Wireless Battery-Free Wearable Sweat Sensor Powered by Human Motion. *Science Advances* **2020,** *6*, eaay9842.

18. Wang, P.-F.; Lin, X.; Liu, L.; Sun, Q.-Q.; Zhou, P.; Liu, X.-Y.; Liu, W.; Gong, Y.; Zhang, D. W., A Semi-Floating Gate Transistor for Low-Voltage Ultrafast Memory and Sensing Operation. *Science* **2013,** *341*, 640-643.

19. Han, S.-T.; Zhou, Y.; Wang, C.; He, L.; Zhang, W.; Roy, V. A. L., Layer-by-Layer-Assembled Reduced Graphene Oxide/Gold Nanoparticle Hybrid Double-Floating-Gate Structure for Low-Voltage Flexible Flash Memory. *Advanced Materials* **2013,** *25*, 872-877.

20. Shi, W.; Guo, Y.; Liu, Y., When Flexible Organic Field-effect Transistors Meet Biomimetics: A Prospective View of the Internet of Things. *Advanced Materirals* **2020,** *32*, 1901493.

21. Liu, C.; Yan, X.; Song, X.; Ding, S.; Zhang, D. W.; Zhou, P., A Semi-Floating Gate Memory Based on van der Waals Heterostructures for Quasi-Non-Volatile Applications. *Nature Nanotechnology* **2018,** *13*, 404-410.

22. Fuller, E. J.; Keene S. T.; Melianas, A.; Wang, Z.; Agarwal, S.; Li, Y.; Tuchman, Y.; James, C. D.; Marinella, M. J.; Yang, J. J.; Salleo, A.; Talin, A. A., Parallel Programming of An Ionic Floating-Gate Memory Array for Scalable Neuromorphic Computing. *Science* **2019,** *364*, 570-574.

23. Krauhausen, I.; Koutsouras, D. A.; Melianas, A.; Keene, S. T.; Lieberth, K.; Ledanseur, H.; Sheelamanthula, R.; Giovannitti, A.; Torricelli, F.; Mcculloch, I.; Blom, P. W. M.; Salleo, A.; van de Burgt, Y.; Gkoupidenis, P., Organic Neuromorphic Electronics for Sensorimotor Integration and Learning in Robotics. *Science Advanced* **2021,** *7*, eabl5068.

24. Viola, F. A.; Barsotti, J.; Melloni, F.; Lanzani, G.; Kim, Y. H.; Mattoli, V.; Caironi, M., A Sub-150-Nanometre-Thick and Ultraconformable Solution-Processed All-Organic Transistor. *Nature Communications* **2021,** *12* (1), 5842.

25. Molina-Lopez, F.; Gao, T. Z.; Kraft, U.; Zhu, C.; Ohlund, T.; Pfattner, R.; Feig, V. R.; Kim, Y.; Wang, S.; Yun, Y.; Bao, Z., Inkjet-Printed Stretchable and Low Voltage Synaptic Transistor Array. *Nature Communications* **2019,** *10* (1), 2676.

26. Chu, S.; Chen, W.; Fang, Z.; Xiao, X.; Liu, Y.; Chen, J.; Huang, J.; Xiao, Z., Large-Area and Efficient Perovskite Light-Emitting Diodes Via Low-Temperature Blade-Coating. *Nature Communications* **2021,** *12* (1), 147.

27. Yuk, H.; Lu, B.; Lin, S.; Qu, K.; Xu, J.; Luo, J.; Zhao, X., 3D Printing of Conducting Polymers. *Nature Communications* **2020,** *11* (1), 1604.

28. Droguet, B. E.; Liang, H. L.; Frka-Petesic, B.; Parker, R. M.; De Volder, M. F. L.; Baumberg, J. J.; Vignolini, S., Large-Scale Fabrication of Structurally Coloured Cellulose Nanocrystal Films and Effect Pigments. *Nature Materials* **2021**, *21*, 352–358.

29. Pecunia, V.; Nikolka, M.; Sou, A.; Nasrallah, I.; Amin, A. Y.; McCulloch, I.; Sirringhaus, H., Trap Healing for High-Performance Low-Voltage Polymer Transistors and Solution-Based Analog Amplifiers on Foil. *Advanced Materials* **2017,** *29* (23), 1606938.

30. Arias, A. C.; MacKenzie, J. D.; McCulloch, I.; Rivnay, J.; Salleo, A., Materials and Applications for Large Area Electronics: Solution-Based Approaches. *Chemical Reviews* **2010,** *110*, 3–24.

31. Lee, S.; Choi, M. J.; Sharma, G.; Biondi, M.; Chen, B.; Baek, S. W.; Najarian, A. M.; Vafaie, M.; Wicks, J.; Sagar, L. K.; Hoogland, S.; de Arquer, F. P. G.; Voznyy, O.; Sargent, E. H., Orthogonal Colloidal Quantum Dot Inks Enable Efficient Multilayer Optoelectronic Devices. *Nature Communications* **2020,** *11* (1), 4814.

32. Muhieddine, K.; Ullah, M.; Pal, B. N.; Burn, P.; Namdas, E. B., All Solution-Processed, Hybrid Light Emitting Field-Effect Transistors. *Advanced Materials* **2014,** *26* (37), 6410-6415.

33. Muhieddine, K.; Ullah, M.; Maasoumi, F.; Burn, P. L.; Namdas, E. B., Hybrid Area-Emitting Transistors: Solution Processable and with High Aperture Ratios. *Advanced Materials* **2015,** *27* (42), 6677-6782.

34. Zhou, H.; Zhang, Y.; Mai, C. K.; Collins, S. D.; Nguyen, T. Q.; Bazan, G. C.; Heeger, A. J., Conductive Conjugated Polyelectrolyte as Hole-Transporting Layer for Organic Bulk Heterojunction Solar Cells. *Advanced Materials* **2014,** *26* (5), 780-785.

35. Lee, B. R.; Yu, J. C.; Park, J. H.; Lee, S.; Mai, C. K.; Zhao, B.; Wong, M. S.; Jung, E. D.; Nam, Y. S.; Park, S. Y.; Di Nuzzo, D.; Kim, J. Y.; Stranks, S. D.; Bazan, G. C.; Choi, H.; Song, M. H.; Friend, R. H., Conjugated Polyelectrolytes as Efficient Hole Transport Layers in Perovskite Light-Emitting Diodes. *ACS Nano* **2018,** *12* (6), 5826-5833.

36. Chen, H.; Xing, X.; Miao, J.; Zhao, C.; Zhu, M.; Bai, J.; He, Y.; Meng, H., Highly Efficient Flexible Organic Light Emitting Transistor Based on High-k Polymer Gate Dielectric. *Advanced Optical Materials* **2020,** *8* (6), 1901651.

37. Gao, H.; Miao, Z.; Qin, Z.; Yang, J.; Wang, T.; Gao, C.; Dong, H.; Hu, W., Redistributed Current Density in Lateral Organic Light-Emitting Transistors Enabling Uniform Area Emission with Good Stability and Arbitrary Tunability. *Advanced Materials* **2021**, e2108795.

38. Prosa, M.; Benvenuti, E.; Kallweit, D.; Pellacani, P.; Toerker, M.; Bolognesi, M.;

Lopez-Sanchez, L.; Ragona, V.; Marabelli, F.; Toffanin, S., Organic Light-Emitting Transistors in A Smart-Integrated System for Plasmonic-Based Sensing. *Advanced Functional Materials* **2021,** *31*, 2104927.

39. Sebastian, A.; Gallo, M. L.; Khaddam-Aljameh, R.; Eleftheriou, E., Memory Devices and Applications for In-Memory Computing. *Nature Nanotechnology* **2020,** *15*, 529-544.

40. Sangwan, V. K.; Hersam, M. C., Neuromorphic Nanoelectronic Materials. *Nature Nanotechnology* **2020,** *15*, 517-528.

Chapter 6. Fabrication of Versatile Low Voltage LAOLETs

Organic light-emitting transistors (OLETs) have been considered as key components for the next generation of active-matrix display to replace active-matrix display organic light-emitting diodes (AMOLED) due to their cost-efficiency combining of switching function and luminescence function.[1-6] Hybrid OLETs are perfect platforms to study multifunctional devices due to their facile processibility by making use of individually deposition of dielectric layer, channel layer and light emitting layer.[7-9] By embedding the floating gate into hybrid OLETs, electric-spiked long afterglow organic light-emitting transistor (LAOLETs) have been demonstrated as single device integrating a triple functionality, *i.e.* the light generation characteristic of light-emitting diodes, the signal amplification of field-effect transistors, and the memory current modulation imparted by the charges storage units. Such multifunctional devices can become key components for the emergence of the next-generation of electronic technologies in the context of more-than-Moore and Internet of Everything. Moreover, upon incorporating bionic sensing elements in the device, LAOLET can become particularly appealing for the development of the long afterglow bio-sensor for health monitoring.

Despite the great advancements made in this field, an inevitable limitation for OLET technology toward real applications in displays is their too high working voltage (ca. 100 V). Such problem can be solved by either shrinking the channel length, utilizing high-*k* materials as dielectric layer, or employing higher mobility materials as channel layer.[10] Among them, increasing capacitance of dielectric layer by replacing SiO_2 with low-dielectric constant (*k*) to high-*k* materials have been demonstrated as a successful method to solve this problem. Both inorganic and organic high *k* materials, including zirconia (ZrO_x), neodymium-doped aluminum oxide (Al_2O_3:Nd), cross-linked poly(vinyl alcohol) (C-PVA), poly(vinylidene fluoride-trifluoroethylene-chlorofloroethylene) (P(VDF-TrFE-CFE)), have been embedded into OLET for

decreasing the operation voltage to the amplitude of ~20 V.[11-14]

On the other hands, harnessing postsynaptic current (PSC) to drive long-lasting luminescence in LAOLET holds a disruptive potential for the next-generation of reconfigurable displays. Notably, there are two distinct synaptic behaviors according to device architectures with various memory mechanisms. In floating gate synaptic devices, depletion voltage represents a pre-synaptic stimulus for facilitation while amplification voltage can be used to accomplish the depression process.[15-18] Conversely, in ferroelectric synaptic transistors[19-20] and electrolyte synaptic transistors[21-24], depression and facilitation can be attained by tuning the depletion and amplification voltages, respectively. The advantage of the floating gate transistors former one is that depletion voltage induced a low programming current to avoid the interference of PSC. However, in ferroelectric synaptic transistors and electrolyte synaptic transistors, the use of amplification voltages yield an enlarge PSC in facilitation. So far, research on electrical spiked LAOLETs has been mainly focused on devices based on a floating gate structure whereas the use of electrolyte gate or ferroelectric gate structures is unexplored.

In this chapter we exploit the deposition of lanthanum aluminum oxide ($LaAlO_x$) dielectric layer by sol-gel method in the fabrication of both N-type and P-type low voltage LAOLETs. The dielectric constant (k) of $LaAlO_x$ quasi quantified as 13 by performing impedance measurements. Such a high k value enables to exploit low operation voltages, *i.e.* around 12 V, to run the synaptic transistors and LAOLETs which represents a significant decrease compared with previously reported devices. Furthermore, two different synaptic behaviors were observed as a result of the dielectric layer functionalization. Long afterglow emission after depletion voltage stimulus occurred in P-type low voltage LAOLETs, which can be summed-up to the contribution of the floating-gate of Au NPs embedded in the $LaAlO_x$ layer. Conversely, in N-type low voltage LAOLETs, PSC and post-synaptic brightness (PSB) facilitated by amplification voltage relied on the presence of electrolyte layer of aluminum oxide

(AlO_x). In-depth studies on long afterglow displays mimicked by distinct synaptic behavior under a human-safety operation voltage provides clear evidence of the versatility of our low voltage LAOLETs.

6.1. Experimental Method

Octylphosphonic acid, green light-emitting spiro-copolymer (SpiroG), indium nitrate hydrate ($In(NO_3)_3 \cdot xH_2O$, 99.9%), gallium nitrate hydrate ($Ga(NO_3)_3 \cdot xH_2O$, 99.9%), zinc acetate dehydrate ($Zn(OAc)_2 \cdot 2H_2O$, 99.9%) were purchased from Sigma-Aldrich. Poly[9,9-bis(60-(N,Ndiethylamino)hexyl)-fluorene-alt-9,9-bis(3-ethyl(oxetane-3-ethyoxy)-hexyl)-fluorene] (PFNOX) and Poly(9,9-bis(6-trimethyl-ammoniumiodide)-hexylfluorene-2,7-diyl-alt-(benzo[2,1,3]thiadiazol-4,7-diyl)) (PFNBT) were purchased from Lumtec. Poly(2,5-bis(2-octyldodecyl)pyrrolo[3,4-c]pyrrole-1,4(2H,5H)-dione-3,6-diyl)-alt-(2,2′;5′,2″;5″,2‴-quaterthiophen-5,5‴-diyl)) (DPP4T) (M_W > 100K) and poly(4-butylphenyl-diphenyl-amine) (PTPD) (M_W ~ 80K) were purchased from 1-Materials. All the materials were used as received, without any further purification.

Preparation of AlO_x Precursor Solution. $Al(NO_3)_3 \cdot xH_2O$ were dissolved in 2-methoxyethanol at concentration at 0.3 M and stirred at room temperature overnight.

Preparation of $LaAlO_x$ Precursor Solution. 375 mg $Al(NO_3)_3 \cdot xH_2O$ and 433 mg $La(NO_3)_3 \cdot xH_2O$ were dissolved in 4 mL 2-methoxyethanol and stirred at room temperature overnight.

Preparation of IGZO Precursor Solution. $In(NO_3)_3 \cdot xH_2O$, $Ga(NO_3)_3 \cdot xH_2O$ and $Zn(OAc)_2 \cdot 2H_2O$ were dissolved in 2-methoxyethanol at concentration at 0.2 M respectively and stirred at room temperature overnight. Upon mixture, IGZO precursor solution was obtained.

Preparation of DPP4T Solution. 40 mg DPP4T were dissolved in 10 mL dichlorobenzene, and then stirred at 80 °C overnight. The solutions were heated at

150 °C for 30 min before being spin-coated.

Preparation of PFNOX solution. 10 mg PFNOX were dissolved in 5 mL methanol and 50 μL acetic acid and then stirred at 80 °C overnight.

Preparation of PFNBT solution. 10 mg PFNBT were dissolved in 9.5 mL 2-methoxyethanol and 0.5 mL methanol and then stirred at 70 °C overnight.

Preparation of PTPD solution. Preparation of PTPD Solution. 60 mg PTPD were dissolved in 10 mL chlorobenzene, and then stirred at 80 °C overnight.

Preparation of SpiroG solution. 80 mg SpiroG were dissolved in 10 mL toluene and then stirred at 80 °C overnight.

Devices were fabricated on the ultra-flat glass substrates (Ossila Company). The glass substrates were cleaned with water, acetone, and alcohol in sequence and dried under N_2 flow. 30 nm Cr was deposited thorough shadow mask on the glass substrate as gate electrode. The substrates with gate electrode were further treated with UV-ozone for 30 min. The morphology of Cr electrode before and after annealing at 360°C for 2h were evaluated by atomic force microscopy (AFM), as illustrated in Figure 6-1a and 6-1b respectively. The subtle increase in the roughness (R_{RMS}) of gate electrode from 0.85 nm to 1.10 nm indicates the morphology of Cr is robust enough to avoid aggregation during device fabrication process.

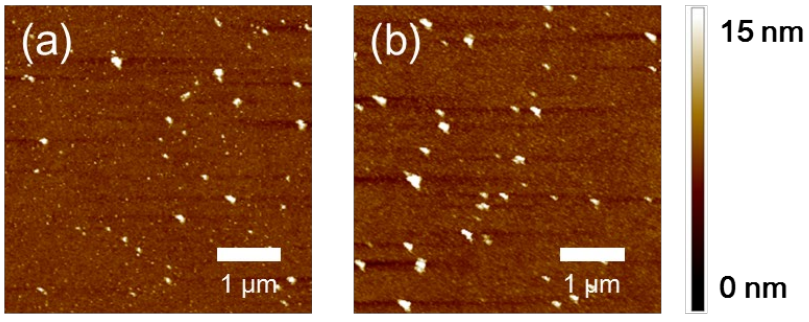

Figure 6-1. AFM topographical images of gate electrode before (a) and after (b) high temperature annealing.

High *k* materials $LaAlO_x$ (La:Al = 1:1) was utilized as dielectric layer in this work. For N-type dielectric layer deposition: The $LaAlO_x$ precursor solution was spin-coated at 3000 rpm for 60 s on a glass substrate, following dried at 160 °C for 5 min and baked at 360 °C for 30 min. Subsequently, the AlO_x precursor solution was spin-coated at 2000 rpm for 60 s on the substrate, followed by a drying up at 160 °C for 5 min and annealing at 360 °C for 30 min. As a result, the N-type dielectric layer comprised one layer of $LaAlO_x$ with thickness of 30 nm preventing breakdown and one layer of AlO_x with thickness of 40 nm operating as electrolyte layer. For P-type dielectric layer deposition: The $LaAlO_x$ precursor solution was spin-coated at 1500 rpm for 60 s on a glass substrate, followed by a drying up at 160 °C for 5 min and annealing at 360 °C for 30 min for the forming of 60 nm thin film layer. Au NPs with a diameter of ~ 2-4 nm were thermally evaporated onto the devices to act as nano-floating gate electrode.[25] (Figure 6-2a) Subsequently, the $LaAlO_x$ precursor solution was spin-coated at 3500 rpm for 60 s on glass substrate, followed by a drying up at 160 °C for 5 min and annealing at 360 °C for 30 min forming of 15 nm tunneling layer.

The *k* values of AlO_x and $LaAlO_x$ were quantified by performing measurements in sandwich capacitor of Cr/AlO_x or $LaAlO_x$/Al. More precisely, the *k* value of dielectric materials can be extracted from equation of $k = C \times t / \varepsilon_0$, where C and *t* is the capacitance and thickness of thin film layer and ε_0 is vacuum permittivity. From *k*-frequency (*k*-*F*) curves plotted in Figure 6-2b, the *k* value of $LaAlO_x$ were defined as 13 at 1000 Hz, which are drastically large than that of SiO_2 (2.3). Notably, the *k* value of AlO_x increases with the decreasing frequency applied, demonstrating the ions displacement exhibited in the bulk.[26] This enhanced *k* value of AlO_x dielectric films under low-frequency electrical field is originated from the electrical double layers (EDL) forming by the moving ion in AlO_x films.[27] Conversely, such ions displacement was inhibited in $LaAlO_x$ film, which can contribute to the doping of La atom with higher Gibbs energy of oxidation.[28] The morphology of N-type and P-type dielectric layer are portrayed in Figure 6-2c and 6-2d, respectively. The R_{RMS} of these two dielectric layers amount to

0.18 nm and 0.53 nm, respectively, indicating the ultra-flat nature of the surface, making them suitable for multilayer materials deposition. The capacitance of P-type and N-type dielectric layer was estimated by impedance measurements as 150 nF·cm^{-2} and 125 nF·cm^{-2}, respectively (Figure 6-2d).

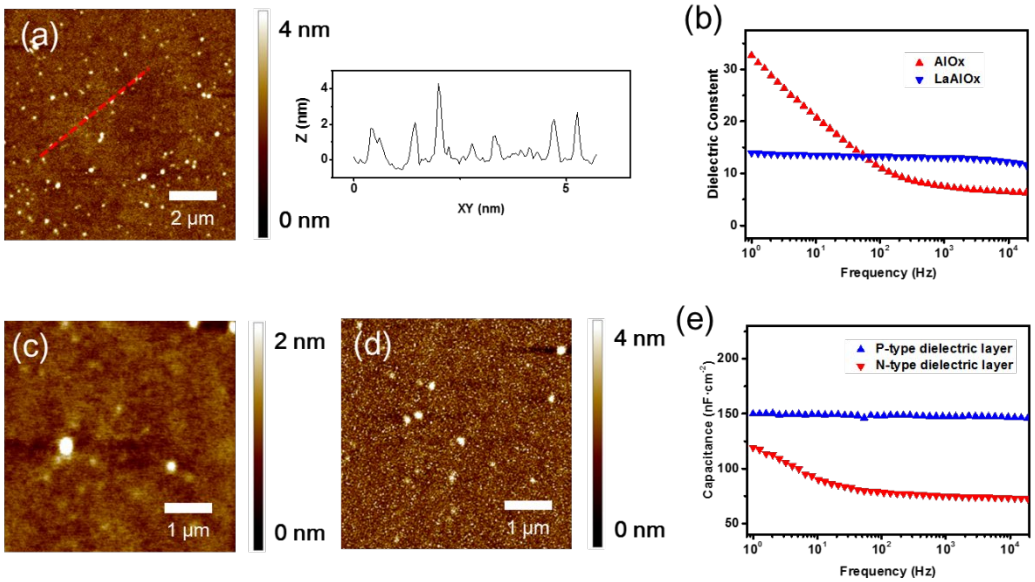

Figure 6-2. (a) AFM topographical image and profile of Au floating gate. (b) *k-F* curve of sandwich capacitor based on AlO_x and $LaAlO_x$ thin films. AFM topographical images of (c) N-type dielectric layer and (c) P-type dielectric layer, respectively. (e) *C-F* curve of sandwich capacitor based on N-type and P-type dielectric layer.

For P-type low voltage devices fabrication: The substrates were soaked in 0.05 M octylphosphonic acid solution overnight before being used. A channel layer with thickness of 50 nm was spin-coated on substrates from hot DPP4T solution. For P-type synaptic transistor: Interdigitated Au electrodes (50 nm) were evaporated on the DPP4T film through shadow masks. (Figure 6-3a) For P-type LAOLETs: Au electrodes (50 nm) were evaporated on the DPP4T film through shadow masks. Hole transport layer with thickness of 10 nm was spun from PTPD solution, followed by a thermal annealing at 150 °C for 10 min. The SpiroG layer with thickness of 60 nm was spun from SpiroG solution, followed by thermal annealing at 150 °C for 10 min. 15 nm PFNOX was spin-

coated on the top at 1800 rpm for 60s, followed by thermal annealing at 150 °C for 10 min. Finally, 25 nm Au were deposited through shadow masks. The three-dimensional scheme of the device architecture is displayed in Figure 6-3b.

For N-type low voltage devices fabrication: The IGZO precursor solution was spin-coated at 3000 rpm for 45 s on the top of $LaAlO_x$, then dried up at 160 °C for 5 min and thermally annealed at 360 °C for 30 min. For N-type synaptic transistor: Interdigitated Al electrodes (50 nm) were evaporated on the IGZO film through shadow masks (Figure 6-3c). For N-type LAOLETs: Al electrodes (50 nm) were evaporated on the IGZO film through shadow masks. Electron transport layer with thickness of 15 nm was spun from PFNOX solution, followed by a thermal annealing at 150 °C for 10 min. The SpiroG layer with thickness of 60 nm was spun from SpiroG solution, followed by thermal annealing at 150 °C for 10 min. 20 nm PFNBT was spin-coated on the top at 1800 rpm for 60s, followed by thermal annealing at 150 °C for 10 min. Finally, 25 nm Au were deposited through shadow masks. The three-dimensional scheme of the device architecture is displayed in Figure 6-3d.

The optical images of the P-type and N-type LAOLETs are displayed in Figure 6-3e and 6-3f, respectively. The width (W) and length (L) of the channel in LAOLETs amount to 32 mm and 200 μm, respectively, whereas the emission area is defined as 4.36 mm^2. The chemical structures of the molecules used in this work are depicted in Figure 6-3g.

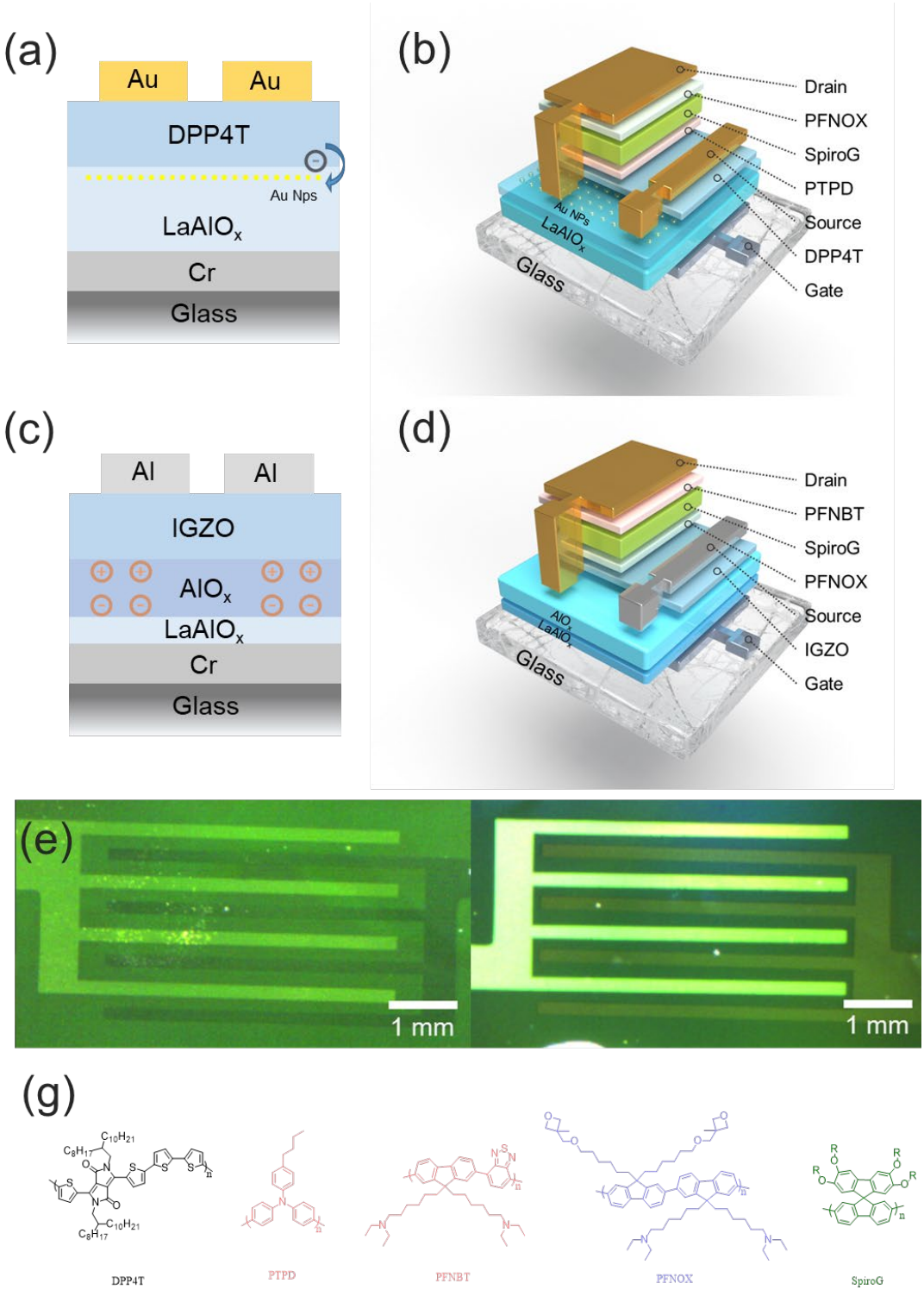

Figure 6-3. Side-view scheme of the low voltage (a) P-type and (c) N-type synaptic transistors. Three-dimensional scheme of the low voltage (b) P-type and (d) N-type LAOLETs. Optical image of low voltage (e) P-type and (f) N-type LAOLETs. (g) Chemical structures of DPP4T, PTPD, PFNBT, PFNOX and SpiroG.

The devices were characterized in a dry, nitrogen-filled glove-box. The electrical characteristics and basic synaptic functions were measured by a semiconductor parameter analyzer (Keithley 2636). The irradiation intensities of the devices were measured with a photodiode (HAMAMATSU S3204-08) which has been previously calibrated by a luminance meter (KONICA MINOLTA, LS-100). Electrochemical impedance spectroscopy (EIS), employing by Metrohm Autolab PGSTAT204 potentiostat/galvanostat, was used to characterize the capacitance of dielectric layer with metal-insulator-metal structure. The frequency range for the impedance spectra was from 1 Hz to 100 kHz with a sine-wave voltage signal amplitude of 0.3 V. AFM images were recorded with a Bruker Dimension Icon set-up operating under ambient conditions, in tapping mode. The thicknesses of the films were determined by the Alpha-Sep IQ Surface Profiler.

6.2. Low Voltage Synaptic Transistors

The transfer curves of low voltage P-type synaptic transistors are displayed in Figure 6-4a; they exhibit an anticlockwise hysteresis. When −8 V drain-source voltage (V_D) applied, two distinct states are observed at the two applied gate-source voltage (V_G) sweeping directions, from 5V to −15 V and then backward from −15 V to 5 V, yielding a negatively shifted threshold voltage (ΔV_{Th}). Memory window (ΔV_{Th}) can be exploited to mimic the biological synaptic function, whose working mechanism is displayed in Figure 6-4b. When positive V_G was applied on the P-type transistors, electrons are injected from channel layer into the floating gate with a short time retention, resulting in the increased hole concentration in the P-type channel layer as synaptic weight enhancement.

Spike-timing-dependent plasticity (STDP) and short-term memory (STM) to long-term memory (LTM) transitions are two fundamental synaptic learning rules in neuroscience for “in-memory” calculation. To mimic these two synaptic functions, the real-time measurement of devices was carried out by applying V_G and V_D as the pre-

and post-synaptic terminals, respectively. Pulse V_G spiked of 10 V with frequency of 0.25 Hz, 0.5 Hz and 1.0 Hz were stimulus as presynaptic signal input. Under continued V_D of −8 V electric field, the responding I_{DS} operates as PSC. The spike-frequency-dependent PSC is plotted in Figure 6-4c to 6-4e. Upon applying V_G for 25 sec with frequency of 0.25 Hz, the PSC increases from 0.07 mA to 0.12 mA, and then it slowly decays. As frequency of pre-synaptic stimulus increased, PSC enhances to 0.15 mA. Under 1.0 Hz pre-synaptic stimulus, PSC facilitated markedly to 0.20 mA. The decay curves and fitting lines of PSC of P-type synaptic transistors are presented in Figure 6-6a. The lifetime of PSC under 0.25 Hz, 0.5 Hz and 1.0 Hz were calculated as 8.19 sec, 46.7 sec and 73.1 sec, providing unambiguous evidence for the successful STM to LTM transition.

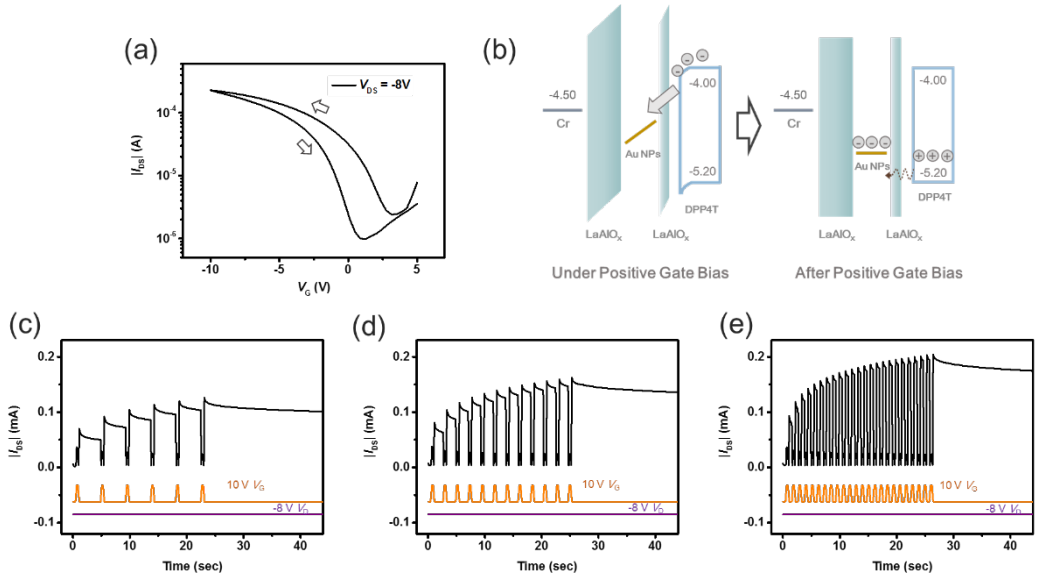

Figure 6-4. (a) Transfer hysteresis curves of low-voltage P-type synaptic transistors. (b) Schematic energy-band diagrams for illustration the work mechanism of low-voltage P-type synaptic transistors. Time dependence measurement of devices carried out by positive V_G spiked with the frequency of (c) 0.25 Hz, (d) 0.5 Hz and (e) 1.0 Hz, respectively. Pulse width of V_G spikes are set at 0.4 sec. Black, orange and purple lines represent the real-time PSC, V_G and V_D, respectively.

On the other hand, the transfer curves of low voltage N-type synaptic transistors are also displayed in Figure 6-5a; they exhibit an anticlockwise hysteresis. Similarly, two distinct states are observed at two different V_G sweeping directions, yielding a ΔV_{Th} of 5V when 8 V V_D is applied. On the contrary to the P-type synaptic transistors, I_{DS} is programed by amplified voltage and erased by depletion voltage in N-type synaptic transistors. Such different phenomenon can be contributed to different memory storage mechanism. In floating gate transistors, memory depend on the opposite charge injected into floating gate. Conversely, in N-type electrolyte synaptic transistors, memory relied on the generation of an electron double layer (EDL). As displayed in Figure 6-5b, the moving ions including proton and nitrate group in the electrolyte layer can migrate towards the interface accumulated as EDL when a positive V_G applied.[29] After removal of the V_G, this EDL is maintained for a short time and still provides the amplified effect to the channel IGZO layer.

To enable comparison with P-type synaptic transistors, time-dependence measurement on low voltage N-type synaptic transistors were also carried out. Positive V_G of 10 V and V_D of 8 V were applied as the pre- and post-synaptic terminals, respectively (Figure 6-5c to 6-5e). Thanks to the amplified voltage applied as facilitated pre-synaptic stimulus, large PSC of 0.4 mA, 0.8 mA and 2.1 mA occur as 0.25 Hz, 0.5 Hz and 1.0 Hz V_G has been applied. However, as evidenced in the decay curves and fitting lines displayed in Figure 6-6b, the lifetime of PSC is shorter than that in P-type synaptic transistors, which is ascribed to the fast charge recombination of EDL. According to the decay curves of PSC after 0.25 Hz and 0.5 Hz V_G spikes, the lifetimes of PSC are negligible. Upon acerating the V_G spiked to 1.0 Hz, observable memory lifetime of 0.16 sec could be achieved, which also suggest the successful conversion of STM to LTM.

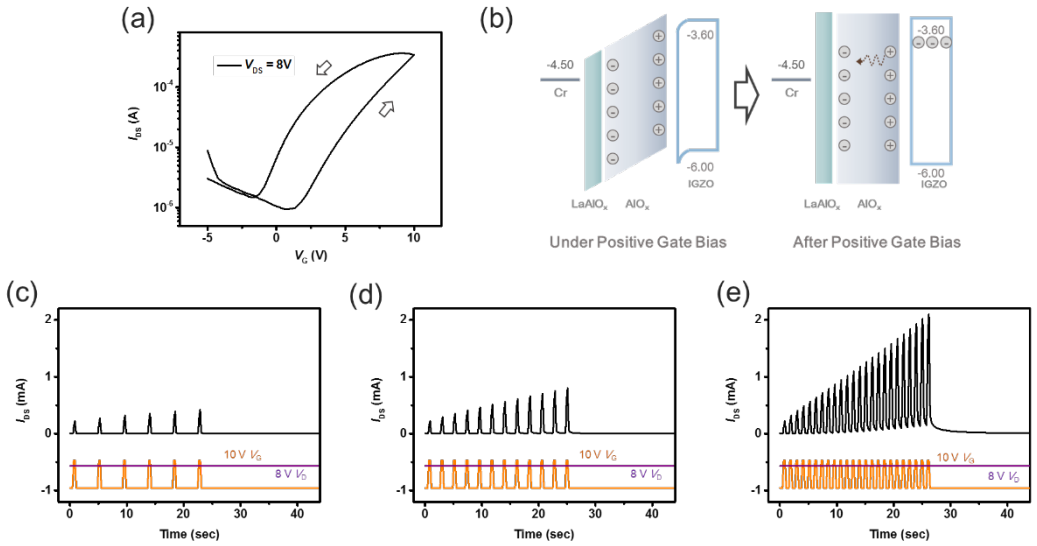

Figure 6-5. (a) Transfer hysteresis curves of low-voltage N-type synaptic transistors. (b) Schematic energy-band diagrams for illustration the work mechanism of low-voltage N-type synaptic transistors. Time dependence measurement of devices carried out by positive V_G spiked with the frequency of (c) 0.25 Hz, (d) 0.5 Hz and (e) 1.0 Hz, respectively. Pulse width of V_G spikes are set as 0.4 sec. Black, orange and purple lines represent the real-time PSC, V_G and V_D, respectively.

The lifetime (τ_l) of PSC in the devices can be determined from the decay curves according to the exponential equation $I(t) = I_0 \times \exp(-t/\tau_l) + I_\infty$, where I_0 is the initial current and I_∞ is the steady-state current.

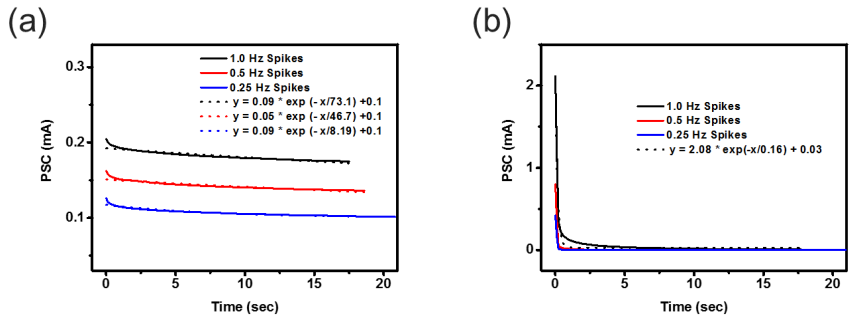

Figure 6-6. Decay curve and fitting line of PSC of (a) low voltage P-type synaptic transistors and (b) low voltage N-type synaptic transistors when spikes with different

frequency are applied.

6.3. Low voltage Long Afterglow OLETs

P-type LAOLETs and N-type LAOLETs were manufactured on glass substrates based on floating gate and electrolyte gate structure, respectively. It is not surprisingly that synaptic behaviors can be achieved in both low voltage LAOLETs.

The combined electrical/optical hysteresis in the transfer curves of P-type LAOLETs are displayed in Figure 6-6a. These devices exhibit a field-effect mobility of 0.078 $cm^2\ V^{-1}\ s^{-1}$, an I_{on}/I_{off} of 10^4 and maximum brightness of 400 cd m^{-2}. More importantly, a remarkable electrical and optical ΔV_{Th} of 8V provide evidence for their potential to mimic synaptic function. The energy levels of the materials components the multilayer structure and the working mechanism including memory and display processes are illustrated in Figure 6-7b. After pre-synaptic signal stimulus, the conductance of the DPP4T channel layer increases as a result of the electron storage in floating gate compising Au NPs. Therefore, hole carrier can be injected from source electrode to the DPP4T semiconductor, and then transported into hole transport layer of PTPD and light emission layer (EML) of SpiroG. Simultaneously, electron carriers are injected from drain electrode and then migrated from the electron transport layer of PFNOX to the EML, yielding the recombination with hole carrier, ultimately leading to photon emission.

The combined electrical/optical real-time measurement of the devices are plotted in Figure 6-7c to 6-7e. Compared with synaptic transistors, a slightly larger continues V_D bias of −12 V was necessary to apply in LAOLETs for driven the light emission material. PSC of 0.04 mA, 0.05 mA and 0.07 mA with lifetime of 75.5 sec, 61.4 sec and 29.5 sec are obtained when pulse V_G spikes of 10 V with frequency of 0.25 Hz, 0.5 Hz and 1.0 Hz applied (Figure 6-9a). Importantly, the post-synaptic brightness (PSB) with spike-frequency dependent plasticity is observed. After 25 sec V_G spikes with frequency

of 0.25 Hz finished, PSB of 50 cd m^{-2} is observed and presents long afterglow emission. As frequency of pre-synaptic stimulus increased to 0.5 Hz and 1.0 Hz, PSB enhanced markedly to 90 cd m^{-2} and 120 cd m^{-2}. From the decay curves and fitting lines of PSB of P-type LAOLETs in Figure 6-9(c), the lifetime of PSB under 0.25 Hz, 0.5 Hz and 1.0 Hz were calculated as 20.0 sec, 32.4 sec and 35.5 sec, confirming the successful STM to LTM transition of long afterglow. Such results are consistent with our previous work, where devices were fabricated on Si/SiO_2 substrate.

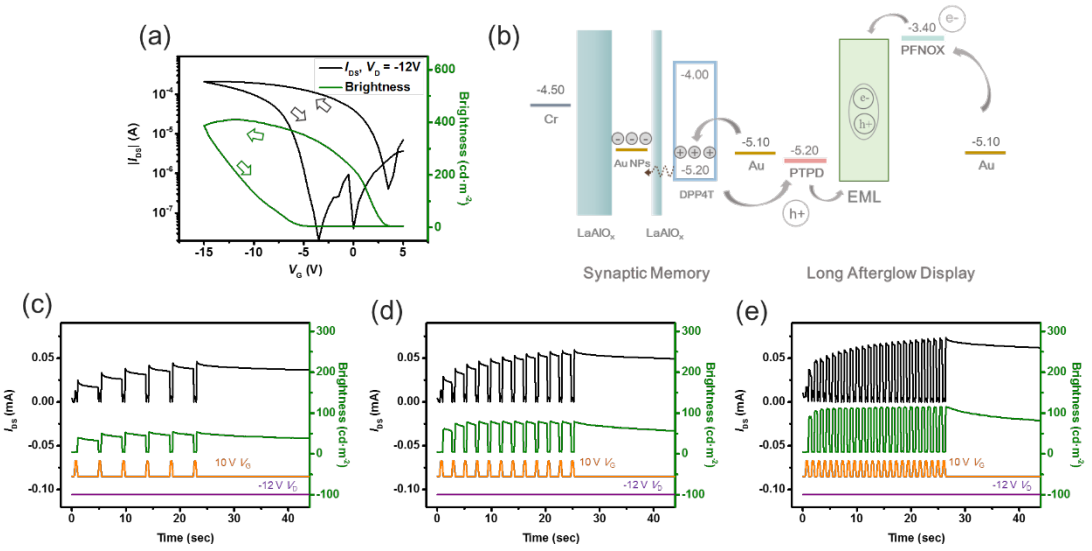

Figure 6-7. (a) Electrical and optical transfer hysteresis curves of low-voltage P-type LAOLETs. (b) Schematic energy-band diagrams for illustration the long afterglow display of devices. Time dependence measurement of devices carried out by positive V_G spiked with the frequency of (c) 0.25 Hz, (d) 0.5 Hz and (e) 1.0 Hz, respectively. Black, green, orange and purple lines represent the real-time PSC, PSB, V_G and V_D, respectively.

The combined electrical/optical hysteresis transfer curves of N-type LAOLETs have been characterized and are displayed in Figure 6-8a. These devices exhibited a superior field-effect mobility of 0.91 cm^2 V^{-1} s^{-1}, an I_{on}/I_{off} of 10^4, maximum brightness of 1300 cd m^{-2} and excellent electrical and optical ΔV_{Th} of 8V. The energy levels of the

components forming the multilayer structure and the working mechanism including memory and display processes are portrayed in Figure 6-8b. As for the case of P-type LAOLETs, EML were incorporated in between the PFNOX and PFNBT layer which functioned as electron and hole transport layer, respectively. After pre-synaptic signal input, EDL forming in the electrolyte layer increased the conductance of channel IGZO layer and thus electron carriers could be injected from source electrode into the IGZO. The recombination of electron and hole carriers in the EML yielded a uniform drain-shaped region of light emission.

The combined electrical/optical real-time properties on low voltage N-type LAOLETs have been also characterized to allow comparison with P-type LAOLETs. Positive V_G of 10 V and V_D of 12 V were applied as the pre- and post-synaptic terminals, respectively (Figure 6-7c to 6-7e). Similar to N-type synaptic transistor, amplified voltage facilitates the PSC as high as 0.3 mA, 0.4 mA and 0.6 mA when 0.25 Hz, 0.5 Hz and 1.0 Hz V_G is spiked. In analogy to P-type LAOLETs, PSB with two important synaptic functions has been achieved. Powered by PSC, a PSB of 750 cd m^{-2}, 1000 cd m^{-2} and of 1300 cd m^{-2} has been recorded, when applying 0.25 Hz, 0.5 Hz and 1.0 Hz V_G spiked respectively. However, the lifetime of PSC and PSB in N-type LAOLETs is unclear, corresponding to N-type synaptic transistor. From the decay curves of PSC and PSB after 1.0 Hz V_G stimulus one can estimate a lifetime as short as 0.36 sec and 0.22 sec (Figure 6-9b).

Interestingly, both in synaptic transistors and LAOLETs, a high PSC accompanied with a PSB is observed but characterized by a shorter lifetime in N-type devices compared with P-type devices. Such a phenomena can be ascribed to the tunnelling layer coating Au NPs which prevents the stored charged to escape, but such a protection is absent in electrolyte bulk. These low voltage LAOLETs exhibiting versatile range of synaptic behaviors can be tailored to meet the specific requirements of different applications.

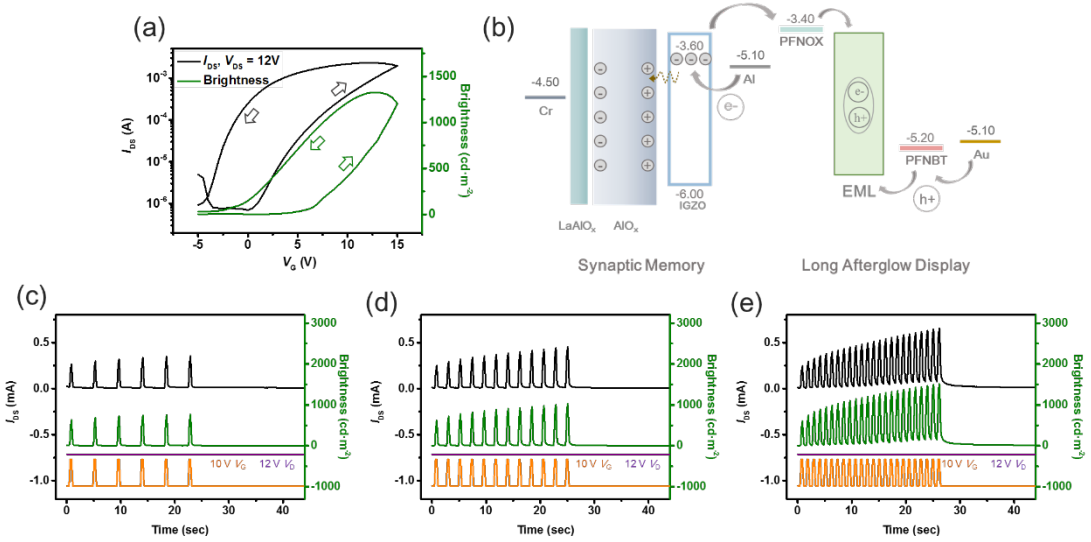

Figure 6-8. (a) Electrical and optical transfer hysteresis curves of low-voltage N-type LAOLETs. (b) Schematic energy-band diagrams for illustration the long afterglow display of devices. Time dependence measurement of devices carried out by positive V_G spiked with the frequency of (c) 0.25 Hz, (d) 0.5 Hz and (e) 1.0 Hz, respectively. Black, green, orange and purple lines represent the real-time PSC, PSB, V_G and V_D, respectively.

Electroluminescence lifetime (τ_l) of PSB in LAOLETs can be also determined from the time-resolved decay of luminescent intensity in the exponential decay equation: $L(t) = L_0 \times \exp(-t/\tau_l) + L_\infty$, where L_0 is the initial fluorescence strength at starting time (t = 0) and L_∞ is the steady-state brightness.

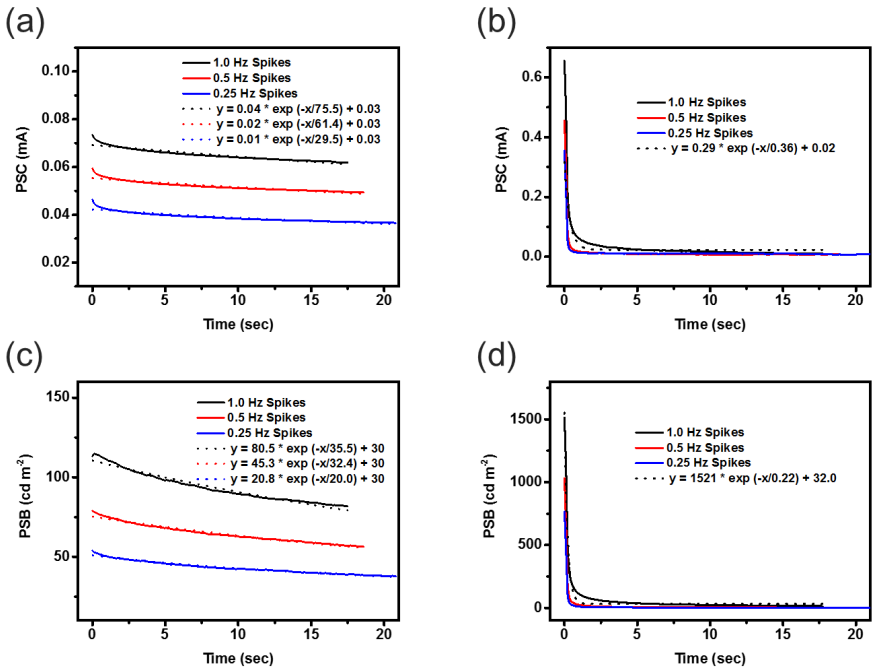

Figure 6-9. Decay curves and fitting lines of PSC of (a) low voltage P-type LAOLETs and (b) low voltage N-type LAOLETs when spikes with different frequency applied. Decay curves and fitting lines of PSB of (c) low voltage P-type LAOLETs and (d) low voltage N-type LAOLETs when spikes with different frequency applied.

Both the optical images of P-type and N-type LAOLETs under −12 V V_D/−10V V_G and 12 V V_D/10V V_G applied electric field are displayed in Figure 6-10a and 6-10b, respectively.

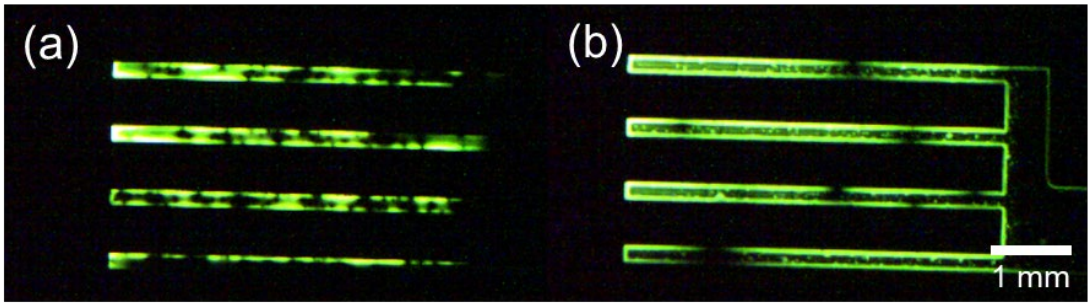

Figure 6-10. Optical images of (a) P-type low voltage LAOLETs and (b) N-type low voltage LAOLETs.

6.4. Conclusions

In summary, in this chapter, low voltage LAOLETs were fabricated based on the high *k* dielectric materials $LaAlO_x$. Such low voltage LAOLETs displayed different synaptic behaviors. In particular, depletion voltage and amplification voltage have been exploited to facilitate PSB in P-type and N-type low voltage LAOLETs, respectively. Compared with floating gate yielding PSB in P-type LAOLETs, PSB imparted by electrolyte gate in N-type LAOLETs displayed higher brightness but shorter lifetime.

6.5. Reference

1. Chaudhry, M. U.; Muhieddine, K.; Wawrzinek, R.; Sobus, J.; Tandy, K.; Lo, S. C.; Namdas, E. B., Organic Light−Emitting Transistors: Advances and Perspectives. *Advanced Functional Materials* **2019,** *30* (20), 1905282.

2. Ganesan, P.; Tsao, H. N.; Gao, P., En Route to Wide Area Emitting Organic Light-Emitting Transistors for Intrinsic Drive-Integrated Display Applications: A Comprehensive Review. *Advanced Functional Materials* **2021,** *31* (48), 2105506.

3. Liu, C. F.; Liu, X.; Lai, W. Y.; Huang, W., Organic Light-Emitting Field-Effect Transistors: Device Geometries and Fabrication Techniques. *Advanced Materials* **2018,** *30* (52), e1802466.

4. Li, J.; Zhou, K.; Liu, J.; Zhen, Y.; Liu, L.; Zhang, J.; Dong, H.; Zhang, X.; Jiang, L.; Hu, W., Aromatic Extension at 2,6-Positions of Anthracene toward an Elegant Strategy for Organic Semiconductors with Efficient Charge Transport and Strong Solid State Emission. *ournal of the American Chemical Society* **2017,** *139* (48), 17261-17264.

5. Liu, D.; De, J.; Gao, H.; Ma, S.; Ou, Q.; Li, S.; Qin, Z.; Dong, H.; Liao, Q.; Xu, B.; Peng, Q.; Shuai, Z.; Tian, W.; Fu, H.; Zhang, X.; Zhen, Y.; Hu, W., Organic Laser Molecule with High Mobility, High Photoluminescence Quantum Yield, and Deep-Blue Lasing Characteristics. *ournal of the American Chemical Society* **2020,** *142* (13),

6332-6339.

6. Yuan, D.; Awais, M. A.; Sharapov, V.; Liu, X.; Neshchadin, A.; Chen, W.; Yu, L., Synergy between Photoluminescence and Charge Transport Achieved by Finely Tuning Polymeric Backbones for Efficient Light-Emitting Transistor. *ournal of the American Chemical Society* **2021,** *143* (13), 5239-5246.

7. Muhieddine, K.; Ullah, M.; Maasoumi, F.; Burn, P. L.; Namdas, E. B., Hybrid Area-Emitting Transistors: Solution Processable and with High Aperture Ratios. *Advanced Materials* **2015,** *27* (42), 6677-6782.

8. Ullah, M.; Wawrzinek, R.; Nagiri, R. C. R.; Lo, S.-C.; Namdas, E. B., UV-Deep Blue-Visible Light-Emitting Organic Field Effect Transistors with High Charge Carrier Mobilities. *Advanced Optical Materials* **2017,** *5* (8), 1600973.

9. Ullah, M.; Lin, Y.-H.; Muhieddine, K.; Lo, S.-C.; Anthopoulos, T. D.; Namdas, E. B., Hybrid Light-Emitting Transistors Based on Low-Temperature Solution-Processed Metal Oxides and a Charge-Injecting Interlayer. *Advanced Optical Materials* **2016,** *4* (2), 231-237.

10. Sobus, J.; Bencheikh, F.; Mamada, M.; Wawrzinek, R.; Ribierre, J. C.; Adachi, C.; Lo, S. C.; Namdas, E. B., High Performance p- and n-Type Light-Emitting Field-Effect Transistors Employing Thermally Activated Delayed Fluorescence. *Advanced Functional Materials* **2018,** *28* (28), 1800340.

11. Pan, Z.; Liu, K.; Miao, Z.; Guo, A.; Wen, W.; Liu, G.; Liu, Y.; Shi, W.; Kuang, J.; Bian, Y.; Qin, M.; Zhu, M.; Zhao, Z.; Guo, Y.; Dong, H.; Liu, Y., Van der Waals Multilayer Heterojunction for Low-Voltage Organic RGB Area-Emitting Transistor Array. *Advanced Materials* **2023,** *35* (8), e2209097.

12. Chen, H.; Xing, X.; Miao, J.; Zhao, C.; Zhu, M.; Bai, J.; He, Y.; Meng, H., Highly Efficient Flexible Organic Light Emitting Transistor Based on High-k Polymer Gate Dielectric. *Advanced Optical Materials* **2020,** *8* (6), 1901651.

13. He, P.; Lan, L.; Deng, C.; Wang, J.; Peng, J.; Cao, Y., Highly Efficient and Stable Hybrid Quantum-Dot Light-Emitting Field-Effect Transistors. *Materials Horizons* **2020,** *7* (9), 2439-2449.

14. Zhao, C.; Chen, H.; Ali, M. U.; Yan, C.; Liu, Z.; He, Y.; Meng, H., Improving the Performance of Red Organic Light-Emitting Transistors by Utilizing a High-k Organic/Inorganic Bilayer Dielectric. *ACS Applied Materials & Interfaces* **2022,** *14* (32), 36902-36909.

15. Ren, Y.; Yang, J. Q.; Zhou, L.; Mao, J. Y.; Zhang, S. R.; Zhou, Y.; Han, S. T., Gate-Tunable Synaptic Plasticity through Controlled Polarity of Charge Trapping in Fullerene Composites. *Advanced Functional Materials* **2018,** *28* (50), 1805599.

16. Yang, X.; Yu, J.; Zhao, J.; Chen, Y.; Gao, G.; Wang, Y.; Sun, Q.; Wang, Z. L., Mechanoplastic Tribotronic Floating-Gate Neuromorphic Transistor. *Advanced Functional Materials* **2020,** *30* (34), 2002506.

17. Zhao, T.; Zhao, C.; Xu, W.; Liu, Y.; Gao, H.; Mitrovic, I. Z.; Lim, E. G.; Yang, L.; Zhao, C. Z., Bio-Inspired Photoelectric Artificial Synapse Based on Two-Dimensional $Ti_3C_2T_x$ MXenes Floating Gate. *Advanced Functional Materials* **2021,** *31* (45), 2106000.

18. Park, E.; Kim, M.; Kim, T. S.; Kim, I. S.; Park, J.; Kim, J.; Jeong, Y.; Lee, S.; Kim, I.; Park, J. K.; Kim, G. T.; Chang, J.; Kang, K.; Kwak, J. Y., A 2D Material-Based Floating Gate Device with Linear Synaptic Weight Update. *Nanoscale* **2020,** *12* (48), 24503-24509.

19. Chen, L.; Wang, L.; Peng, Y.; Feng, X.; Sarkar, S.; Li, S.; Li, B.; Liu, L.; Han, K.; Gong, X.; Chen, J.; Liu, Y.; Han, G.; Ang, K. W., A van der Waals Synaptic Transistor Based on Ferroelectric $Hf_{0.5}Zr_{0.5}O_2$ and 2D Tungsten Disulfide. *Advanced Electronic Materials* **2020,** *6* (6), 2000057.

20. Ko, C.; Lee, Y.; Chen, Y.; Suh, J.; Fu, D.; Suslu, A.; Lee, S.; Clarkson, J. D.; Choe,

H. S.; Tongay, S.; Ramesh, R.; Wu, J., Ferroelectrically Gated Atomically Thin Transition-Metal Dichalcogenides as Nonvolatile Memory. *Advanced Materials* **2016,** *28* (15), 2923-2930.

21. Zhou, Y.; Li, J.; Yang, Y.; Chen, Q.; Zhang, J., Artificial Synapse Emulated through Fully Aqueous Solution-Processed Low-Voltage In_2O_3 Thin-Film Transistor with Gd_2O_3 Solid Electrolyte. *ACS Applied Materials & Interfaces* **2020,** *12* (1), 980-988.

22. Yu, R.; Li, E.; Wu, X.; Yan, Y.; He, W.; He, L.; Chen, J.; Chen, H.; Guo, T., Electret-Based Organic Synaptic Transistor for Neuromorphic Computing. *ACS Applied Materials & Interfaces* **2020,** *12* (13), 15446-15455.

23. Li, Y.; Xuan, Z.; Lu, J.; Wang, Z.; Zhang, X.; Wu, Z.; Wang, Y.; Xu, H.; Dou, C.; Kang, Y.; Liu, Q.; Lv, H.; Shang, D., One Transistor One Electrolyte-Gated Transistor Based Spiking Neural Network for Power-Efficient Neuromorphic Computing System. *Advanced Functional Materials* **2021,** *31* (26), 2100042.

24. Zhu, L. Q.; Wan, C. J.; Guo, L. Q.; Shi, Y.; Wan, Q., Artificial Synapse Network on Inorganic Proton Conductor for Neuromorphic Systems. *Nature Communications* **2014,** *5*, 3158.

25. Baeg, K.-J.; Noh, Y.-Y.; Sirringhaus, H.; Kim, D.-Y., Controllable Shifts in Threshold Voltage of Top-Gate Polymer Field-Effect Transistors for Applications in Organic Nano Floating Gate Memory. *Advanced Functional Materials* **2010,** *20* (2), 224-230.

26. Liang, X.; Li, Z.; Liu, L.; Chen, S.; Wang, X.; Pei, Y., Artificial Synaptic Transistor with Solution Processed InOx Channel and AlOx Solid Electrolyte Gate. *Applied Physics Letters* **2020,** *116* (1), 012102.

27. Zhu, L. Q.; Sun, J.; Wu, G. D.; Zhang, H. L.; Wan, Q., Self-Assembled Dual In-Plane Gate Thin-Film Transistors Gated by Nanogranular SiO_2 Proton Conductors for Logic Applications. *Nanoscale* **2013,** *5* (5), 1980-1985.

28. Banger, K.; Warwick, C.; Lang, J.; Broch, K.; Halpert, J. E.; Socratous, J.; Brown, A.; Leedham, T.; Sirringhaus, H., Identification of Dipole Disorder in Low Temperature Solution Processed Oxides: Its Utility and Suppression for Transparent High Performance Solution-Processed Hybrid Electronics. *Chemical Science* **2016,** *7* (10), 6337-6346.

29. Park, J. H.; Kim, K.; Yoo, Y. B.; Park, S. Y.; Lim, K.-H.; Lee, K. H.; Baik, H. K.; Kim, Y. S., Water Adsorption Effects of Nitrate Ion Coordinated Al_2O_3 Dielectric for High Performance Metal-Oxide Thin-Film Transistor. *Journal of Materials Chemistry C* **2013,** *1* (43), 7166-7174.

Chapter 7. Application of LAOLETs

In the above experimental chapters, UV-spiked LAOLETs, electrical spiked LAOLETs and low-voltage LAOLETs were fabricated successfully. In these devices, post-synaptic brightness (PSB) powered by post-synaptic current (PSC) was accomplished with two fundamental synaptic rules, spike-timing-dependent plasticity (STDP) and short-term memory (STM) to long-term memory (LTM) transitions.

As describe in chapter 4, UV-spiked LAOLETs can exhibit long afterglow emission after UV irradiation if one exploits the unique PPC characteristics of the IGZO channel layer. This UV irradiation dependence of long afterglow emission can be used to display UV irradiative patterns, that cannot be captured by human eyes. By taking full advantage of such an exceptional characteristic, a visual UV sensor based on 100 UV-spiked LAOLETs arrays has been fabricated and reported in paragraph 7.1.

Bio-sensors can be sensitive to various bio-signals such as heat, sound, pressure, chemical ion, by providing response in the current output. As described in chapter 5, trigged by positive and negative gate signal input, electrical spiked LAOLETs display “click-on” light emission and long afterglow emission, respectively. The pressure sensor has been combined with electrical spiked LAOLETs to achieve pressure-induced light emission, which is presented in paragraph 7.2.

In the future, both UV-spiked and electrical spiked LAOLETs are expected to find applications as key components in “in-memory” computing and multifunctional devices.

7.1. Visual UV Sensor

The persistent light-emission in UV-spiked LAOLETs can also be observed even without applying a gate voltage. To demonstrate unique behavior of UV-spiked LAOLETs and explore their potential for advanced opto-electronics applications, we have fabricated an *ad hoc* light-emitting array composed of 100 two-terminal pixels

without gate electrode. As shown in the Figure 7-1a, the device was fabricated on a 2.5 × 2.5 cm^2 glass substrate with a structure of IGZO/Al/PFNOX/CBP:CzDBA/NPB/Au. Detailed image of the patterned electrode is provided (Figure 7-1d). The aperture ratio of these devices amounted to 0.39, hence being comparable to that of commercial LED-LCD and OLED displays (around 0.34).[1]

Noteworthy, our unprecedented long afterglow devices do not suffer from undesired appearance of random noise. In fact, the post-synaptic weights difference of each pixels was caused by the different UV photon flux.[2,3] Optical image of device were captured in Figure 7-1b and 7-1c. Figure 7-1e also displays the layout of five shadow masks characterized by an *ad hoc* design combining a standard pattern consisting of a number 8 with point defects. Upon exposure of the device successively to five UV irradiations by using a different shadow mask in each of them, it was possible to modulate the photons flux for each pixel thereby enabling to program coexistence of LTP and STP states in neighboring pixels. In particular, PSC of STP is not sufficient to power the light-emission of the pixels and PSB with a pattern “8” in absence of noise is observed by the camera. Thus, high luminescence efficiency and long light-emission lifetime were achieved simultaneously under prolonged or repetitive UV stimulus, with a marked difference in brightness between desired area and noise information by an accurate spatial distribution of UV-exposed pixels. As a proof-of-concept, our LAOLETs array possesses a capability of delayed luminescence as an UV-imager due to its synaptic characteristics.

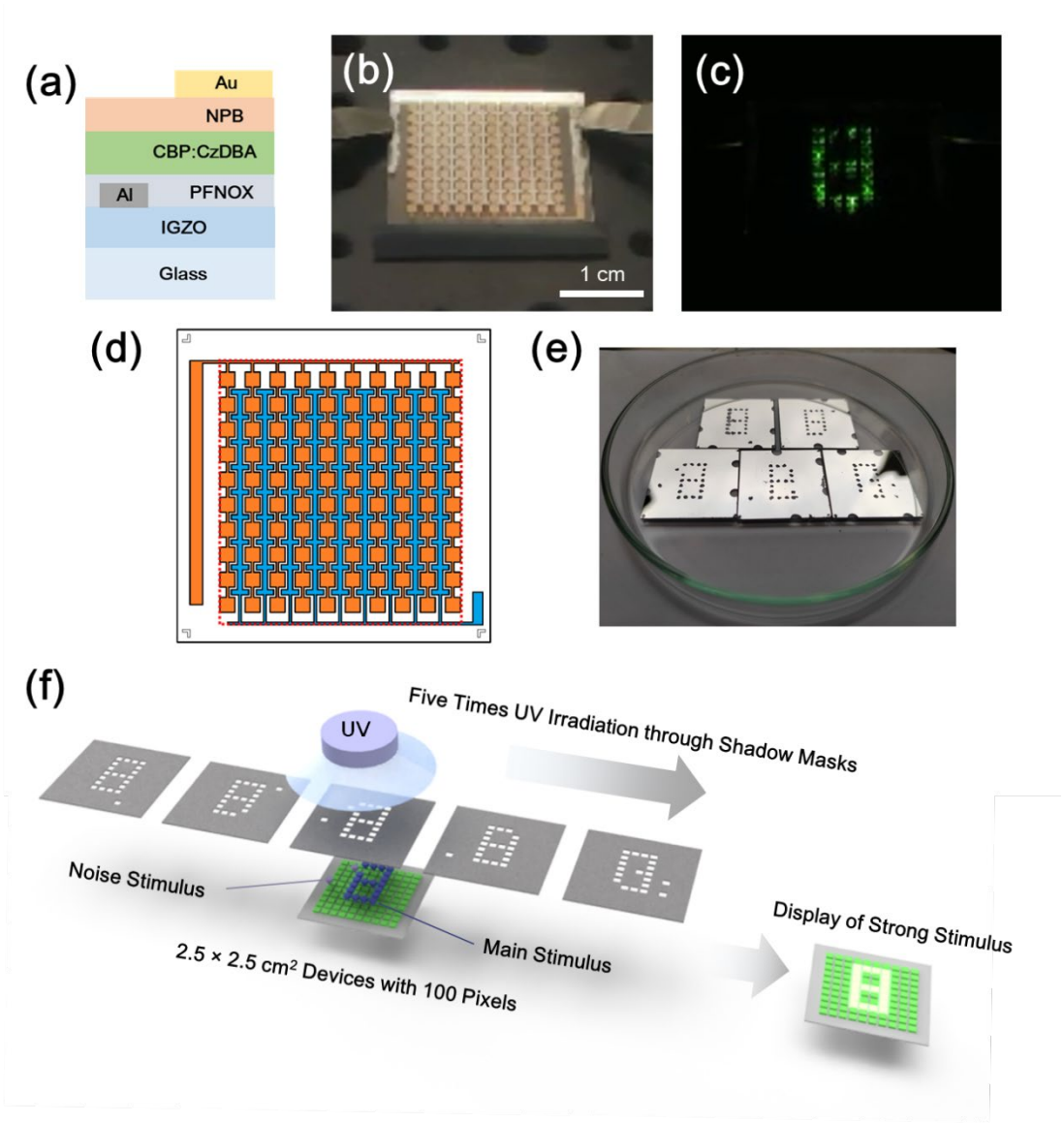

Figure 7-1. Typical optical image and schematic images of two terminal long afterglow device with 100 pixels. (a) Cross section schematic images of device structure. (b) Optical image of device. (c) Light emission image of device after five times UV irradiation. (d) Electrode pattern of two terminal long afterglow device, where blue color represent Al electrode and orange color represent Au electrode. The aperture ratio of these devices was calculated as area of Au/area of device (red dot square). (e) Photo of UV shadow masks for different UV stimulus. (f) Schematic illustration of UV irradiation through five different shadow masks which lead to five similar stimuli with different noise, and correct pattern of "8" display finally. V_D of 40 V were applied for

this device.

7.2. Long Afterglow Pressure Sensors

Pressure sensing represents a crucial input that needs to be embedded in intelligent bionic systems, especially because flexible and wearable pressure sensors can satisfy the needs of human motion detection for health and disease diagnosis. Electrically conductive polymer-nano composites have been widely reported as piezoresistive sensor. Hence, toward processing long afterglow sensors, a graphene sponge was selected because their advantages of low-cost, environmental-friendly, and simple fabrication.[4] The optical image and *I-V* characterized curves of the graphene sponge are presented in Figure 7-2a and 7-2b. When a pressure of ca. 6 kPa was exerted to the graphene sponge, the pressure sensor drastically transformed from high resistant state to low resistant state. As a proof-of-concept, aiming at demonstrating the practical application of the long afterglow device, long afterglow pressure sensors were fabricated by integrating two units (Figure 7-2c), a graphene sponge as pressure sensor component and a G-LAOLETs unit fabricated as described above. Real-time measurement of this long afterglow pressure sensor is displayed in Figure 7-2d upon applying a V_G of 120 V. The orange, black and green lines correspond to the I_{GS}, I_{DS} and brightness, respectively. Initially, the pressure sensor resistance was much greater than the setting resistance. When a pressure was exerted on the device, I_{GS} increased to 0.02 mA and the resistance of total circuit (which corresponds to the sum of the setting and the pressure sensor resistance) was calculated as 6 MΩ. Correspondingly, the voltage dropped on G-LAOLETs could be emulated as 100 V, leading to long afterglow emission after ceasing the pressure signal input. This long afterglow emission could be also enhanced by repeating the pressure signal input. Another operating mode was also achieved upon applying a V_G of −120 V. Light emission of device was observed when each pressure signal input was applied (Figure 7-2e).

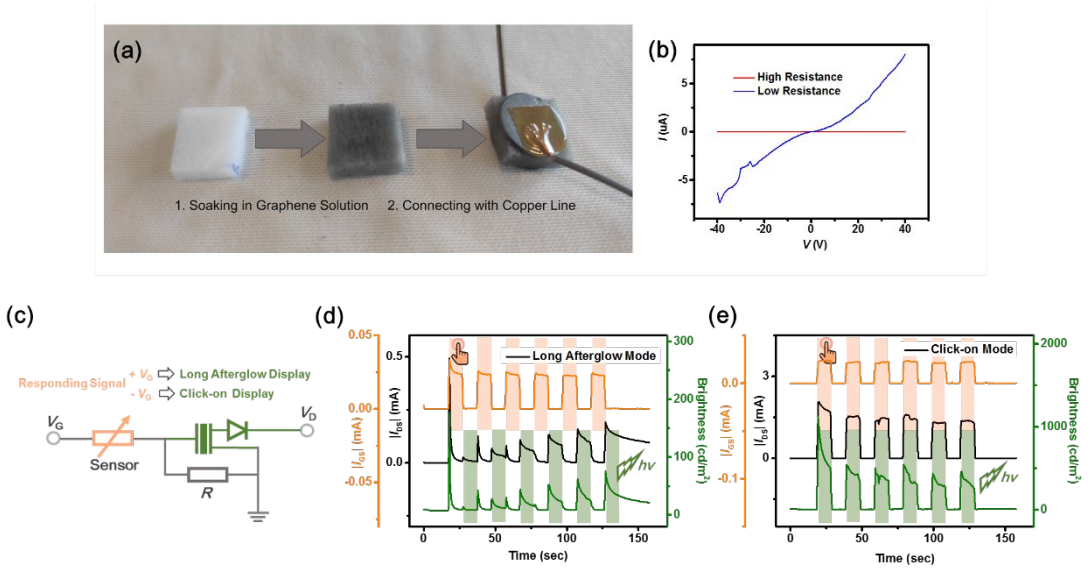

Figure 7-2. (a) Optical image of pressure sensor. (b) *I-V* curves of pressure sensor before (high resistance) and after (low resistance) having exerted a pressure of 6 kPa. (c) Equivalent electrical circuit integrating the pressure sensor function in a G-LAOLET. R is a setting resistance of 5 MΩ. Real-time measurement of long afterglow pressure sensor upon applying a V_G of (d) 120 V, and (e) −120 V.

7.3. Conclusions

In summary, in this chapter, two practical applications based on UV-spiked and electrical spiked LAOLETs were demonstrated. 100 UV-spiked LAOLETs array without gate electrode has been operated as visual UV sensors with a capacity of auto-noise-filter. In order to respond to other physical and chemical pre-synaptic signal input, electrical spiked LAOLETs can be combined with several sensors. As proof-of-concept, external pressure trigged long afterglow emission were realized by exploiting a piezo-responsive sensor.

7.4. Reference

1. Nam, W. J.; Kim, C. Y.; Lee, J. H.; Park, S. G.; Han, M. K., High-Aperture Ratio AMOLED Pixel Design Employing V_{DD} Line Elimination for Reducing OLED Current

Density. *SID Symposium Digest of Technical Papers* **2012**, *36*, 1456.

2. Wu, C.; Kim, T. W.; Choi, H. Y.; Strukov, D. B.; Yang, J. J., Flexible Three-Dimensional Artificial Synapse Networks with Correlated Learning and Trainable Memory Capability. *Nature Communications* **2017**, *8*, 752.

3. Yang, F. S.; Li, M.; Lee, M. P.; Ho, I. Y.; Chen, J. Y.; Ling, H.; Li, Y.; Chang, J. K.; Yang, S. H.; Chang, Y. M.; Lee, K. C.; Chou, Y. C.; Ho, C. H.; Li, W.; Lien, C. H.; Lin, Y. F., Oxidation-Boosted Charge Trapping in Ultra-Sensitive van der Waals Materials for Artificial Synaptic Features. *Nature Communications* **2020**, *11*, 2972.

4. Zhao, J.; Ren, W.; Cheng, H.-M., Graphene Sponge for Efficient and Repeatable Adsorption and Desorption of Water Contaminations. *Journal of Materials Chemistry* **2012**, *22*, 20197-20202.

Chapter 8. Conclusions and Perspectives

8.1. Conclusions

While the development of multifunctional and multiresponsive electronic devices such as transistors have been already demonstrated, the research on multifunctional light-emitting devices is rather an unchartered territory. On the same time, neuromorphic-like functional properties in artificial molecule-based materials and devices have recently gained a great attention as means to accomplish complex logic operations.

In this thesis we have successfully integrated the synaptic function, amplification function and light emission function into a single device based on the transistors structure. Importantly, by harnessing the PSC to drive light emission materials PSB has been attained, which can be operated as long afterglow with two essential synaptic function, STDP and STM to LTM transition.

Firstly, an IGZO layer with PPC characteristics was integrated in hybrid OLETs device architecture to power electroluminescence of solution processed TADF emissive layers. Irradiation with UV light at λ=312 nm determined to the production of oxygen vacancies in the IGZO layer which free electrons in excess yielding to an increase in the channel conductance. Due to the slow recombination kinetics of such electrons with oxygen vacancies, the conductance of IGZO channel retained its high state. As a result, in this UV-spiked LAOLETs, the UV light activated PSC has fueled a persistent bright emission with CIE x,y (0.37, 0.57) expanding from the gold electrode with long afterglow. The brightness and lifetime of devices could be enhanced by prolonged UV irradiation, resulting in long-term plasticity of post-synaptic brightness of 11 cd m^{-2} with lifetime of 272 sec. The decaying ratio could be also modulated by controlling the gate voltage. Appling V_G of −30 V, PSB of 4 cd m^{-2} with lifetime of 159 sec were recorded.

In the second experimental chapter, we have presented the fabrication of electrical spiked LAOLETs which was accomplished by assembling on a Si/SiO_2 wafer through successive spin-coating depositions a multilayered structure comprising Au NPs as nano-floating gate coated with an insulating Al_2O_3 tunneling barrier supporting four different functionalized polymer layers acting as channel, hole transport, light-emission and electron transport layer, respectively. By using SpiroG as light-emitting material, G-LAOLETs exhibiting a maximum brightness of 2500 cd m^{-2} and an I_{on}/I_{off} ratio of 10^5 were realized. After applying positive gate spike as pre-synaptic stimulus, long afterglow display of 81 cd m^{-2} with lifetime of 14.08 sec was attained. The PSB of devices can be enhanced to 142 cd m^{-2} by repeating the stimulus. On the same time, the lifetime of PSB could be prolonged to 17.17 sec by increasing stimulus width to 24 sec. Significantly, another operating mode, displaying a prompt light-emission under each negative gate spiked was also observed in the same device. In light of such unique characteristics, our LAOLETs can find application as reconfigurable displays. Furthermore, by exploiting four commercially available semiconducting polymers as light-emissive layers, full color LAOLETs ranged in whole visible light were achieved with approximately ΔV_{Th} and ΔV_{on} of ~30 V and $I_{P/E}$ of ~10^3, respectively.

In these two examples, to power the LAOLETs a high operation voltage of ca. 100 V was required, jeopardizing their technology relevance. As third example, we have overcome this major problem by replacing the low k dielectric materials SiO_2 with $LaAlO_x$. Such solution processed dielectric material exhibits a high k value of 13. Furthermore, based on $LaAlO_x$, both P-type and N-type low voltage LAOLETs could be fabricated successfully, which can work under low operation absolute voltage of V_D = 12 V and V_G = 10 V. On the same time, floating gate and electrolyte gate were embedded into P-type and N-type low voltage LAOLETs respectively, yielding two different PSB behaviors. By using the depletion voltage as pre-synaptic signal input with frequency of 1.0 Hz, long afterglow display of 120 cd m^{-2} with lifetime of 35.5 sec was attained in low voltage P-type LAOLETs. Conversely, upon exploiting

amplification voltage as pre-synaptic signal input with same frequency, long afterglow display with higher brightness of 1300 cd m^{-2} with but shorter lifetime of 0.22 sec was observed in N-type LAOLETs.

Finally, practical applications based on LAOLETs were developed as proof-of-concept. A large size of 2.5 × 2.5 cm^2 long afterglow light-emitting devices capable to record UV irradiations were realized, demonstrating the enormous potential of our LAOLETs for applications as visual UV micro-sized sensors. Upon integrating a piezo-responsive sensor with these electrical spiked LAOLETs, long afterglow emission could be trigged by exerting an external pressure, suggesting their relevance for long afterglow sensing technologies.

8.2. Short-Term Perspectives

Although OLETs have been the subject of various studies during the last two decades, their performance, such as maximum brightness, EQE and turn-on voltage, is stills inferior to that of OLEDs. Key steps forward aimed at improving the performance of LAOLETs can be achieved in the near future through the enhanced materials design and device engineering. (a) The use of light-emitting materials with high PLQY (approaching 100%) and exploitation of channel materials with high field-effect mobilities around 10 cm^2 V^{-1} s^{-1} can enable to enhance the I_{DS} and current efficiency of LAOLETs. On the same time, the lifetime of OSC should also be optimized with long term stability, which fit the requirement of LAOLETs for long afterglow emission.[1] (b) It is well-known that embedding the electron/hole injection layer and electron/hole blocking layer into the OLEDs architecture can sufficiently decrease the interface energy barrier and thus improve device perfromance.[2] The deposition of multi-interface layers into LAOLETs can be foreseen as ideal strategy to further decrease the operation voltage of LAOLETs.

Our LAOLETs is a promising functional element for the development of active-matrix integrated displays and optical memories. The possibility of triggering long

afterglow emission by applying a force was demonstrated by fabricating pressure sensors integrated LAOLETs, providing unambiguous evidence that our LAOLETs can respond to bionic stimulus for artificial sensory-related synaptic display in tomorrow's smart opto-electronics. (c) In the future, upon changing the responsive units, different kinds of long afterglow sensors capable to respond to diverse stimuli can be employed for light, thermal, sound and bio-molecular sensing in new active displays.[3] (d) Upon blending OSC with stretchable matrix, stretchable LAOLET devices can be manufactured for the realization of multifunctional e-skin in human or robot, which is also desirable in health monitoring system.[4]

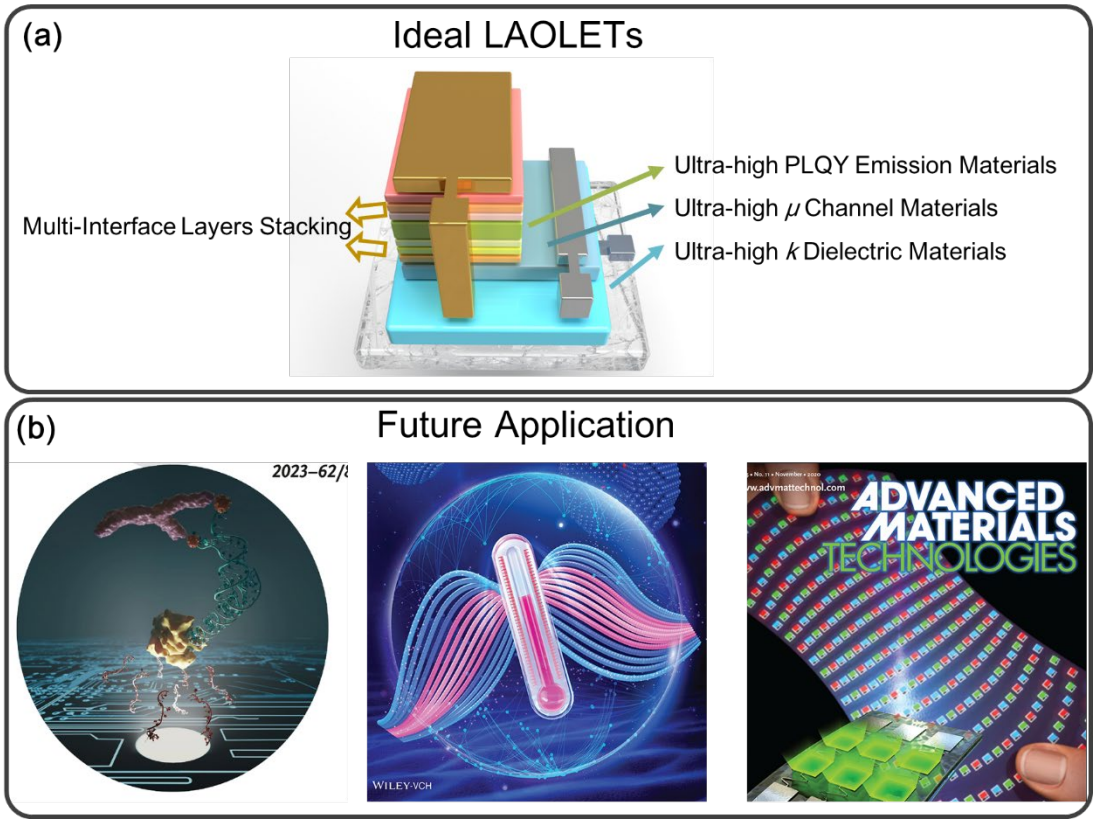

Figure 8-1. (a) Ideal device structure of LAOLETs with multi-interface layers and high property OSC. (b) Proposed practical application of LAOELTs when integrated with bio-sensor and temperature sensor, even fabricated as stretchable one.[5-7]

8.3. Long-Term Perspectives

The vision of artificial brain fabrication has inspired researchers to mimic the function of natural brain into electronic device. Neural processing unit (NPU) based on artificial neural network (ANN) have been successfully applied on pattern recognition in smartphone such as Iphone 13. However, in ANN, the two-dimension synaptic crossbar array structure is far away to "copy" human brain, because the synapse connection in nervous system is three-dimensions (3D). Toward the fabrication of natural neuronal network (NNN), 3D integration technology has been considered as a potential approach,[8] as shown in Figure 8-2a. Moreover, the brain is not only composed by synapses and neural cell that transmit information by volatile neurotransmitter (*i.e.* Ca^{2+}, Na^{+}), tissue and protein in the brain also present the essential roles, which can be considered as non-volatile existence.

Herein, we propose the development of the memory optocoupler, which is composed by LAOLET and optically switchable filed-effect transistor (OSFETs) (Figure 8-2b). In principle, LAOLET is a device kind that can process post-synaptic current and display post-synaptic brightens, while OSFET is a device capable to store photon flux into non-volatile current as multilevel. Electrical and optical processing in this optocoupler is obviously orthogonal. In presence of a post-synaptic current signal input, PSC in LAOLETs occurs. If the PSC is strong enough to power the light emission materials, PSB is observed which can be used as input in OSFET to record an information, *i.e.* as non-volatile memory with a current output. In this way, light can act as the bridge between the instantaneous memories and the permanent memories in a non-contact method, thereby reproducing the relationship of synapse and protein/tissue in the human brain.

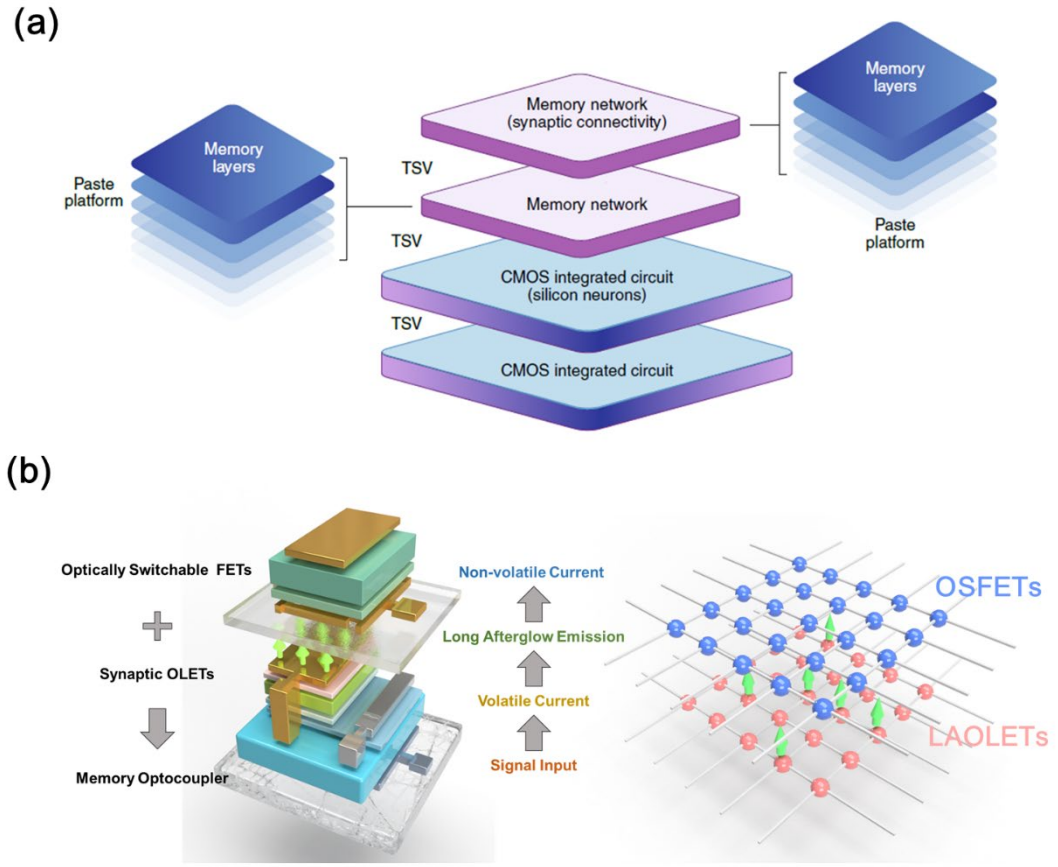

Figure 8-2. (a) A NNN can be fabricated by vertically packaged memory network and CMOS integrated circuit via 3D integration technology based on through-silicon vias (TSVs).[8] (b) Our proposal of fabrication a NNN based on memory optocoupler, which can be also 3D integrated and provide the function of volatile memory to non-volatile memory transmission.

8.4. Reference

1. Scholz, S.; Kondakov, D.; Lüssem, B.; Leo K., Degradation Mechanisms and Reactions in Organic Light-Emitting Devices. *Chemical Reviews* **2015**, *115* (16), 8449–8503

2. Byeon, S.; Lee, D.; Yook, K.; Lee, J. Recent Progress of Singlet-Exciton-Harvesting Fluorescent Organic Light-Emitting Diodes by Energy Transfer Processes.

Advanced Materials **2019**, *31*, 1803714

3. Ditte, K.; Nguyen Le, T. A.; Ditzer, O.; Sandoval Bojorquez, D. I.; Chae, S.; Bachmann, M.; Baraban, L.; Lissel, F., Rapid Detection of SARS-CoV-2 Antigens and Antibodies Using OFET Biosensors Based on a Soft and Stretchable Semiconducting Polymer. *ACS Biomaterials Science & Engineering* **2021**, DOI: 10.1021/acsbiomaterials.1c00727.

4. Lee, Y.; Park, J.; Choe, A.; Cho, S.; Kim, J.; Ko, H. Mimicking Human and Biological Skins for Multifunctional Skin Electronics. *Advanced Functional Materials* **2020**, *30*, 1904523.

5. Bracaglia, S.; Ranallo, S.; Ricci. F., Electrochemical Cell-Free Biosensors for Antibody Detection. *Angewandte Chemie International Edition* **2023**, *8*, Cover Picture.

6. Cao, S.; Zheng, J.; Zhao, J.; Yang, Z.; Shang, M.; Li, C.; Yang, W.; Fang, X., Temperature Sensors: Robust and Stable Ratiometric Temperature Sensor Based on Zn–In–S Quantum Dots with Intrinsic Dual-Dopant Ion Emissions. *Advanced Functional Materials* **2016**, *40*, Cover Picture.

7. Kim, T.; Lee, H.; Jo, W.; Kim, T.-S.; Yoo. S., Stretchable OLEDs: Realizing Stretchable OLEDs: A Hybrid Platform Based on Rigid Island Arrays on a Stress-Relieving Bilayer Structure. *Advanced Materials Technologies* **2020**, *11*, Inside Back Cover.

8. Ham, D.; Park, H.; Hwang, S.; Kim, K. Neuromorphic Electronics based on Copying and Pasting the Brain. *Nature Electronics* **2021**, 4, 635-644.

Statement of Works

All the experimental data analysis presented in this Thesis was carried out by the author (Yusheng Chen) under the supervised by Prof. Paolo Samorì except for the following:

The Résumé was revised by Dr. Nicolas Weibel.

In Chapter 4, the SEM image was recorded by Dr. Verónica Montes-García.

In Chapter 7, the graphene sponge was fabricated by Feng Luo and Dr. Zhaoyang Liu.

All the images displayed in this thesis were designed by the Yusheng Chen (author), and all the original projects reported in this thesis were designed and developed by Yusheng Chen (author) and Prof. Paolo Samorì.

Acknowledgments

At the end of this Thesis, I would like to thank the Chinese Scholarship Council for providing me the financial support. I will always be grateful to Chinese government because they provide me scholarship for my master's studies. And from then on, I don’t need to worry about bread and milk. I would like to thank my wife and my family for providing spiritual support. No matter what happens, they are my strong backing.

I would like to express my highest gratitude to my Ph.D. supervisor, Prof. Paolo Samorì, for accepting me as a Ph.D. candidate in his group. During my Ph.D. studying, he gives me not only valuable guidance on ideas and experiments but also great freedom to choose the research field. I enjoy the scientific research in such an outstanding research environment.

Very special thanks to Dr. Jiahui Tan, Dr. Junyou Pan, Prof. Zhen-gang Zhu and Prof. Xiaozhong Qu for recommendation and assistance when I was looking for Ph. D. Thesis. Strongly thanks to Dr. Hanlin Wang, Dr. Yifan Yao and Dr. Chun Ma for giving me guidance about the fabrication of synaptic transistors and light-emitting devices when I start my projects. Interacting with them broadened my knowledge and stimulated my new ideas.

I would like to thank Dr. Artur Ciesielski, Dr. Ye Wang, Dr. Shunqi Xu, Dr. Verónica Montes Garcia, Dr. Zhaoyang Liu, Dr. Can Wang, Dr. Nicholas Turetta, Feng Luo and Bin Han for many fruitful discussions and patience in answering my questions. I would like to thank all the members in the Nanochemistry Group. They give me help in both work and life.

I am deeply thankful to the wonderful life. I was born into a poor family, but now I am proud that my life is significantly changed. What does not kill me, makes me stronger.

Yusheng CHEN, 陈煜升

List of Publications

1. Yao, Y.; Chen, Y.; Wang, H.; Samorì, P., Organic Photodetectors Based on Supramolecular Nanostructures. *SmartMat* **2020,** *1* (1), e1009.

2. Chen, Y.; Wang, H.; Yao, Y.; Wang, Y.; Ma, C.; Samorì, P., Synaptic Plasticity Powering Long-Afterglow Organic Light-Emitting Transistors. *Advanced Materials* **2021**, *33* (39), 2103369.

3. Wang, H.; Wang, Y.; Ni, Z.; Turetta, N.; Gali, S. M.; Peng, H.; Yao, Y.; Chen, Y.; Janica, I.; Beljonne, D.; Hu, W.; Ciesielski, A.; Samorì, P., 2D MXene-Molecular Hybrid Additive for High-Performance Ambipolar Polymer Field-Effect Transistors and Logic Gates. *Advanced Materials* **2021,** *33* (20), 2008215.

4. Wang, Y.; Wang, H.; Gali, S. M.; Turetta, N.; Yao, Y.; Wang, C.; Chen, Y.; Beljonne, D.; Samorì, P., Molecular Doping of 2D Indium Selenide for Ultrahigh Performance and Low‐Power Consumption Broadband Photodetectors. *Advanced Functional Materials* **2021,** 31 (30), 2103353.

5. Chen, Y.; Yao, Y.; Turetta, N.; Samorì, P., Vertical Organic Transistors with Short Channels for Multifunctional Optoelectronic Devices. *Journal of Materials Chemistry C* **2022,** *10* (7), 2494-2506.

6. Romito, D.; Fresta, E.; Cavinato, L. M.; Kahlig, H.; Amenitsch, H.; Caputo, L.; Chen, Y.; Samorì, P.; Charlier, J. C.; Costa, R. D.; Bonifazi, D., Supramolecular Chalcogen-Bonded Semiconducting Nanoribbons at Work in Lighting Devices. *Angewandte Chemie International Edition* **2022,** *61* (38), 202202137.

7. Wang, H.; Chen, Y.; Ni, Z.; Samorì, P., An Electrochemical-Electret Coupled Organic Synapse with Single-Polarity Driven Reversible Facilitation-to-Depression Switching. *Advanced Materials* **2022,** *34* (50), 2205945.

8. Yao, Y.; Chen, Y.; Wang, K.; Turetta, N.; Vitale, S.; Han, B.; Wang, H.; Zhang, L.;

Samorì, P., A Robust Vertical Nanoscaffold for Recyclable, Paintable, and Flexible Light-emitting Devices. *Science Advances* **2022,** 8 (10), eabn2225

9. Chen, Y.; Wang, H.; Luo, F.; Montes-García, V.; Liu, Z.; Samorì, P., Nanofloating Gate Modulated Synaptic Organic Light-emitting Transistors for Reconfigurable Displays. *Science Advances* **2022,** 8 (37), eabq4824.

List of Presentations

Conférences nationales et internationales: Poster

Chen, Y.; Wang, H.; Luo, F.; Montes-García, V.; Liu, Z.; Samorì, P. Toward Reconfigurable Displays-Synaptic Plasticity Powering Full Color Long Afterglow Organic Light-Emitting Transistors. International Conference of Electroluminescence and Optoelectronic Devices. (ICEL 2022) London, United Kingdom, 05-07 December 2022.

Yusheng CHEN

Développement de transistors électroluminescents synaptiques : vers des dispositifs électroniques organiques multifonctionnels

Résumé

Cette thèse est consacrée à la fabrication de dispositifs émettant de la lumière multifonctionnels par l'incorporation contrôlée de plusieurs molécules fonctionnelles dans des films préparés soit par mélange, soit par dépôt couche par couche. Les matériaux émettant de la lumière dans les OLET peuvent être alimentés par un courant post-synaptique, qui répond aux impulsions UV et électriques. Une émission de lumière post-synaptique agissant comme une longue émission de lumière rémanente avec deux propriétés synaptiques spéciales, la plasticité dépendante du temps et la transmission de la mémoire à court terme à la mémoire à long terme, est obtenue. En interfaçant une telle fonctionnalité avec le corps humain, nos dispositifs émettant de la lumière peuvent être dotés de capacités de détection de force et être alimentés à des tensions compatibles avec une utilisation sur la peau. La nouveauté de cette thèse est l'intégration sans précédent de la fonction de mémoire synaptique et de la fonction d'affichage dans un seul dispositif.

Mots clés: Molécules optoélectroniques, Affichage à mémoires synaptiques, Électronique organique multifonctionnelle

Résumé en Anglais

This thesis is dedicated to the fabrication of multifunctional light-emitting devices via the controlled incorporation of multiple functional molecules into films which are prepared either by blending or layer-by-layer deposition. Light-emitting materials in OLETs can be powered by post-synaptic current, which respond to UV-spike and electrical spike. Post-synaptic light emission acting as long afterglow light emission with two special synaptic property, spiked-time-dependent-plasticity and short term memory to long term memory transmission, is achieved. By interfacing such functionality with human body, our light-emitting devices can be endowed with force sensing capabilities and be powered at voltages compatible with on-skin operations. The novelty of this thesis is the unprecedented integration of synaptic memory function and display function into one single device.

Keywords: Opto-electronic Molecules, Synaptic Memory Display, Multifunctional Organic Electronic